SCANNING TUNNELLING MICROSCOPY AND TRANSPORT SPECTROSCOPY ON CANDIDATE TOPOLOGICAL SYSTEMS

SHEKHAR DAS

A thesis submitted for the partial fulfillment of the degree of

Doctor of Philosophy

Department of Physical Sciences

Indian Institute of Science Education and Research Mohali

Knowledge city, Sector 81, SAS Nagar, Manauli PO, Mohali

140306, Punjab, India

October, 2019

Dedicated to

my family

Declaration

The work presented in this thesis has been carried out by me under the guidance of Dr. Goutam Sheet at Indian Institute of Science Education and Research (IISER) Mohali. This work has not been submitted in part or in full for a degree, a diploma, or a fellowship to any other university or institute. Whenever contributions of others are involved, every effort is made to indicate this clearly, with due acknowledgement of collaborative research and discussions. This thesis is a bonafide record of original work done by me and all sources listed within have been detailed in the bibliography.

Date:

Place :

<div align="right">Shekhar Das</div>

In my capacity as the supervisor of the candidate's thesis work, I certify that the above statements by the candidate are true to the best of my knowledge.

<div align="right">Dr. Goutam Sheet (Supervisor)</div>

Acknowledgement

First, I would like to thank Dr. Goutam Sheet for giving the opportunity to work in his lab where I got the freedom to work on my interests. His dedication to work inspired me a lot. Discussion with him on various topics helped to improve my understanding not only in the subject but also in overall goal in life. His immense supports on multiple circumstances during my Ph.D. tenure made this journey unforgettable.

I wish to thank my thesis advisory committee, Dr. Yogesh Singh and Dr. Sanjeev Kumar for their heartily support during this work.

I wish to thank Dr. Ananth Venkatasan for some valuable discussions related to this work. I am grateful to Dr. Dipanjan Chakraborty for his encouragements during this work.

I want to thank Prof. Prasenjit Guptasarma from University of Wisconsin, USA, Dr. Kansiska Biswas and Subhajit from JNCASR, India, Dr. Yogesh Singh and Amit from IISER Mohali, India for providing good quality samples. I wish to thank Dr. Tanmoy Das and Gaurav from IISC Bangalore, India for the theoretical studies of our experimental results.

I wish to thank order and purchase team at IISER Mohali for their constant support and cooperative behavior.

I wish to thank Subas Pai and other excel instrument staffs for their cooperation in building instruments. Mukesh Ji, thank you for helping me out of some critical situations during building instruments and for giving access to use your machine shop whenever I need it. The IISER Mohali

da, Soumen da, thank you all for your constant support whenever I need it.

I would like to thank Monojit, Tanmoy, Bikram, Happy, Aritra, and all the school & college friends for their emotional support which helped me to reach in this stage. I am grateful to all the school, college and tuition teachers for their guidance.

List of Publications:

1. *Conventional Superconductivity in Type II Dirac Semimetal $PdTe_2$, **Shekhar Das,** Amit, Anshu Sirohi, Lalit Yadav, Sirshendu Gayen, Yogesh Singh, Goutam Sheet, Physical Review B **97,** 014523 (2018)

2. *Discovery of highly spin-polarized conducting surface states in the strong spin-orbit coupling semiconductor Sb2Se3, **Shekhar Das,** Anshu Sirohi, Gaurav Kumar Gupta, Suman Kamboj, Aastha Vasdev, Sirshendu Gayen, Prasenjit Guptasarma, Tanmoy Das, and Goutam Sheet, Phys. Rev. B **97,** 235306 (2018)

3. *Unexpected superconductivity at nanoscale junctions made on the topological crystalline insulator $Pb_{0.6}Sn_{0.4}Te$, **Shekhar Das**, Leena Aggarwal, Subhajit Roychowdhury, Mohammad Aslam, Sirshendu Gayen, Kanishka Biswas and Goutam Sheet, Appl. Phys. Lett. **109,** 132601 (2016).

4. *A point contact spectroscopy probe for milli-Kelvin applications in high vacuum, **Shekhar Das** and Goutam Sheet, Rev. of Sc. Inst. **90**, 103903 (2019).

5. "Multiband superconductivity in Mo_8Ga_{41} driven by a site-selective mechanism" Anshu Sirohi, Surabhi Saha, Prakriti Neha, **Shekhar Das**, Satyabrata Patnaik, Tanmoy Das, and Goutam Sheet, Physical Review B **99 (5)**, 054503 (2019)

6. Suppression of transport spin-polarization of surface states with emergence of ferromagnetism in Mn-doped Bi_2Se_3", Suman Kamboj, **Shekhar Das**, Anshu Sirohi, Rajeswari Roy Chowdhury, Sirshendu Gayen, Vishal Maurya, S Patnaik and Goutam Sheet, Journal of Physics: Condensed Matter **30,** 35 (2018)

7. Low-energy excitations and non-BCS superconductivity in Nb_x-Bi_2Se_3", Anshu Sirohi, **Shekhar Das**, Prakriti Neha, Karn S. Jat, Satyabrata Patnaik, Goutam Sheet, Phys. Rev. B **98**, 094523 (2018)

8. Mixed type I and type II superconductivity due to intrinsic electronic inhomogeneities in the type II Dirac semimetal PdTe2", Anshu Sirohi, **Shekhar Das**, Rajeswari Roy Chowdhuri, Amit, Yogesh Singh, Sirshendu Gayen, Goutam Sheet, accepted in Journal of Physics Condensed Matter (Nov. 2018)

9. Large enhancement of superconductivity in Zr point contacts", Mohammad Aslam, Chandan K. Singh, **Shekhar Das**, Ritesh Kumar, Soumya Datta, Soumyadip Haldar, Sirshendu gayen, Mukul Kabir and Goutam Sheet, Journal of Physics Condensed Matter **30**, 255002 (2018)

10. Evidence of pseudogap in the ferromagnetic superconductor $Sr_{0.5}Ce_{0.5}FBiS_2$ driven by competing orders of multi-band origin", Mohammad Aslam, Arpita paul, Gohil S Thakur, Ritesh Kumar, Avtar Singh, **Shekhar Das**, Ashok K Ganguli, Umesh V Waghmare and Goutam Sheet, Journal of Physics: Condensed Matter **28**, 195701 (2016).

11. Mesoscopic superconductivity and high spin polarization coexisting at

metallic point contacts on the Weyl semimetal TaAs", Leena Aggarwal, Sirshendu Gayen, **Shekhar Das**, Ritesh Kumar, Vicky Süß, Chandra Shekhar, Claudia Felser and Goutam Sheet, Nature Communications **8**, 13974 (2016)

12. Enhanced zero-bias conductance peak and splitting at mesoscopic interfaces between an s-wave superconductor and 3D Dirac semimetal", Leena Aggarwal, Sirshendu Gayen, **Shekhar Das,** Gohil S Thakur, Ashok K Ganguli and Goutam Sheet, Appl. Phys. Lett. **109**, 252602 (2016)

*Works included in the thesis

Abstract

Topologically non-trivial systems have emerged as a new area of research in condensed matter physics. The study of topologically nontrivial electronic systems is important because they provide a platform to experimentally investigate new low-energy excitations. In this thesis, I will discuss three such systems:

Conventional Superconductivity in PdTe$_2$: PdTe$_2$ is a unique topological system where type II Dirac semimetallic phase coexists with a superconducting phase. This combined nature offers an interesting material candidate for investigation of possible topological superconductivity. We have performed high-resolution scanning tunnelling spectroscopic (STS) measurements to study the nature of superconductivity in this system. Theoretically, it has been speculated that superconductivity in such systems will be unconventional in nature. However, our experiments provide direct evidence of conventional superconductivity in PdTe$_2$.

High spin-polarization in Sb$_2$Se$_3$: Most of the A$_2$B$_3$ type chalcogenides (e.g. Bi$_2$Se$_3$, Bi$_2$Te$_3$ and Sb$_2$Te$_3$ etc.) are well known topological insulators. Though Sb$_2$Se$_3$ is a member of the same group, it is a band insulator under ambient conditions. A prominent quasiparticle interference (QPI) pattern observed in STM conductance mapping indicates the presence of backscattering, which is forbidden for a topological insulator. Interestingly, like most of the topological insulators, Sb$_2$Se$_3$ shows a high spin polarization (69 %) in transport current. To understand the origin of such high spin

polarization, we performed band structure calculations which revealed presence of two trivial surface states with one undergoing large splitting due to Rashba type SOC and leading to high spin polarization.

Tip-induced superconductivity in $Pb_{0.6}Sn_{0.4}Te$: The emergence of tip-induced superconductivity (TISC) has offered a possible way to detect topological superconductivity induced by a point contacts. We performed similar experiment on a topological crystalline insulator (TCI) $Pb_{0.6}Sn_{0.4}Te$ with non-superconducting tips. Our experiments revealed that $Ag/Pb_{0.6}Sn_{0.4}Te$ and $Pd/Pb_{0.6}Sn_{0.4}Te$ point-contacts behave as a superconductor. As expected for a superconductor, we observed a sharp resistive transition at 6 K which evolved systematically with an applied magnetic field. This is also confirmed through temperature and magnetic field dependent studies of the point contact spectra. Moreover, on the basis of Hc Vs Tc phase diagram we predict that the induced superconductivity is conventional in nature.

Furthermore, I will discuss low temperature and high vacuum point-contact probe designing and fabrication.

Contents

1

CHAPTER 1

Introduction

The discoveries of novel materials drive the condensed matter physics research ahead; perhaps it started in the nineteenth century [1] when scientists were beginning to investigate the secret of atoms, through the discovery of superconductivity in the twentieth century [2]. Up until the early twentieth century, this field was known as solid state physics, the study of liquid state adds on it, and later it named as condensed matter physics. Within a short period, this field became more popular and now it is one of the largest community in the world. Condensed matter physics diverges to many research areas in physics such as low energy physics to high energy physics. Condensed matter physics research has played a vital role not only in theoretical advancement but also in technological point of view. Extraordinary instrumentation provides new experimental tools such as a scanning tunnelling microscope (STM) gives us access to play with single atoms; the synchrotron and neutron facilities work in a high energy scale.

In the later twentieth century the discovery of quantum Hall effect [3],

the Nobel prize in 1985 to von Klitzing, opened a new paradigm in condensed matter and material physics. This sensation discovered another new class of quantum matter known as topological materials such as topological insulators (TIs), topological crystalline insulators (TCIs), topological superconductors (TSs), Dirac semimetals (DSMs), Weyl semimetals (WSMs) [4–9] etc. The motivation to work on these materials is due to their extraordinary behaviour which may lead to a new aspect of quantum physics as well as in the technological world – spintronic devices, the key element for quantum computing which may drive us into a completely new generation world.

In the following sections, I will discuss some of the properties of these materials – why they are so exciting? the experimental verifications and analysis tools to measure the quantum properties.

1.1 Overview on topological class of materials:

In order to appreciate the discovery of the new class of materials, it is essential to know the historical background. In 1980, Klaus von Klitzing, G. Dorda, and M.Pepper discovered the integer quantum Hall effect (IQHE) in a Silicon-based MOSFET (metal-oxide-semiconductor field-effect transistor) in high magnetic fields and liquid helium temperatures [3]. They were able to quantize the Hall resistance. It should also be mentioned that the quantization phenomenon was already predicted theoretically in 1974 [10]. Soon after the experimental discovery of QHE, TKNN (Thouless, Kohmoto,

Nightingale, and den Nijs) showed that the quantization property is characterized by topological invariants [11]. In 1982, there was another discovery called the fractional quantum Hall effect (FQHE) [12]. However, it has no direct relevance to topological insulators [13]. At that time quantum Hall systems were considered as topological insulators. But the discovery of spin Hall effect (SHE) in 2004 by Kato *et. al.* again stirred the community [14]. However, there were lots of controversial theoretical models which established the notion of spin currents [15–19]. In 2006, Bernevig, Hughes, and Zhang published a concrete theoretical model for QSHE and also predicted a possible experimental setup to obtain quantum spin Hall effect (QSHE). They proposed a quantum well of HgTe [20] which could be a possible QSH system. Soon after this profound proposal, in 2007, Konig *et. al.* realized QSHE in HgTe/Hg$_{0.3}$Cd$_{0.7}$Te quantum well [21]. This was the first proven 2D topological insulator. Later on QSHE also observed in BiSb [22] and in Bi$_2$Se$_3$ and Bi$_2$Te$_3$ bulk crystals [23–25]. Therefore, in order to understand topological insulator, we have to go through QHE and QSHE first.

1.1.1 Quantum Hall to $\mathbb{Z}_2$ TI:

There are many similarities between IQHE and QSHE. But one significant difference between them is that the QH syestems require an external magnetic field to quantize the Landau levels. The magnetic field in the system breaks the time-reversal symmetry (TRS). Whereas the QSH systems are TRS invariant, do not need an external magnetic field. The spin-orbit coupling generates an effective magnetic field into the system. The theoretical

model for the QSH systems is called a graphene model with SOC [26].
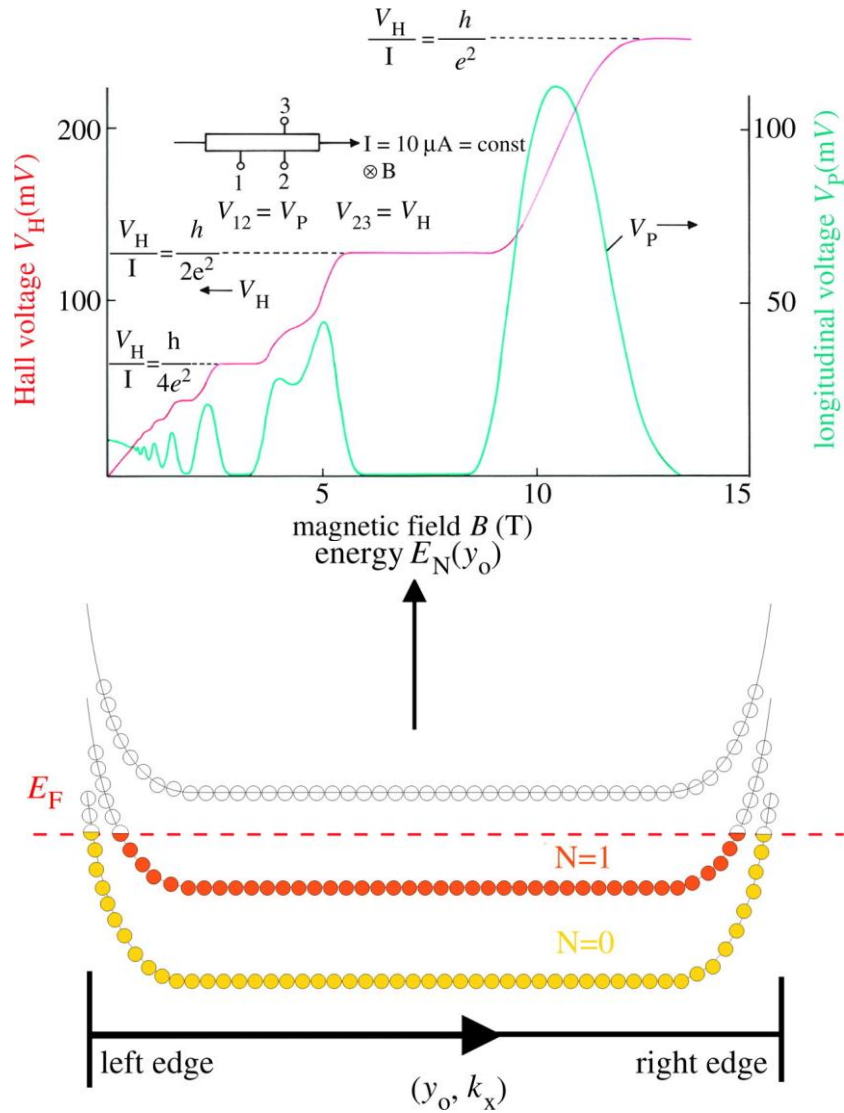
Figure 1.1: (top) Integer quantum Hall effect. Both the transverse and longitudinal resistances are shown, (bottom) Fully occupied Landau levels are crossing Fermi level at the edges. Image ref: [27]

According to the band theory of solids, metals and insulators are differentiated by a band gap which is either zero for metals or nonzero for insulators [28]. But, the discovery of IQHE changed the idea of conventional

behaviour of materials. In case of IQHE, a 2D electron gas is placed in a strong magnetic field forms cyclotron orbits and all the energy bands split into sub-bands, known as Landau levels. The frequency of the cyclotron orbit is ω_c and the energy corresponding to the quantized Landau level is, $E_n = \left(n + \frac{1}{2}\right)\hbar\omega_c$ where, $\omega_c = \frac{eB}{m_c}$, m_c is effective mass of the electron and e is the electronic charge. The single particle Hamiltonian can be written as,

$$H = \frac{(\mathbf{p} - e\mathbf{A})^2}{2m} \tag{1.1}$$

Where A is the magnetic vector potential, $\mathbf{B} = \nabla \times \mathbf{A}$ and $\mathbf{p}$ is momentum. When N Landau levels are filled, and the Fermi level lies in between the Nth and $(N+1)^{th}$ Landau levels, then the occupied and empty states just act as an insulator. Now, change in magnetic field makes ω_c different and as a result, the Landau levels start crossing the Fermi level and gives rise to a quantized Hall resistance [27],

$$R_H = \frac{h}{Ne^2} \tag{1.2}$$

In principle, each Landau level can be represented by a delta function. But due to the presence of the disorders in the sample, the Landau levels become broadened. For a device with area A, the degeneracy of each Ladau level is given by eBA/h which is quite high [27]. With increasing magnetic field the degeneracy increases. Here, in Figure 1.1 (top) the filling factor N decreases with increasing magnetic field, and at 10 T it reaches a value h/e^2 known as Klitzing constant. There could be two possible situations

in IQHE: (i) when the Fermi level lies in between the Landau levels, the plateaus form. Hence the bulk is insulating. However for a sample with finite dimensions, a dissipation less current propagates along the edges of the sample (For a finite sample, the energy levels bend at the edges and cross the Fermi level because of the high potential at the edges). It should be noted that the longitudinal resistance is zero in this situation. The bulk localized electrons which do not contribute to electronic transport and the dissipation less edge transport make it possible. (ii) when the Fermi level crosses the Landau level the scattering occurs in the bulk as well as at the edges of the sample. This leads to the increase in resistance and to reach the next quantized value. Therefore, from here we can see the bulk-boundary correspondence creates the edge states conducting whereas the bulk remains insulating. The Landau levels cross the Fermi level with increasing magnetic field which causes oscillation in the density of states. This can be mapped directly in the Landau level spectroscopy (LLS) measurement using STM/S. The transport measurements also gives an evidence to the quantum oscillations in these system. The longitudinal resistance measurement known as Shubnikov de-Haas effect and in magnetization measurement known as de-Haas van Alphen effect.

The discovery of QSHE is more intriguing because it is related to the topological insulator directly. The QSHE can be considered as a superposition of two identical subsystems with opposite spin directions (Figure 1.2 (top)). If the spin-up corresponds to one subsystem with the conductance $\sigma = e^2/h$ then the other subsystem will be spin-down with the conductance $\sigma = -e^2/h$. The spin direction can be considered as a magnetic field direction. Aperantly,
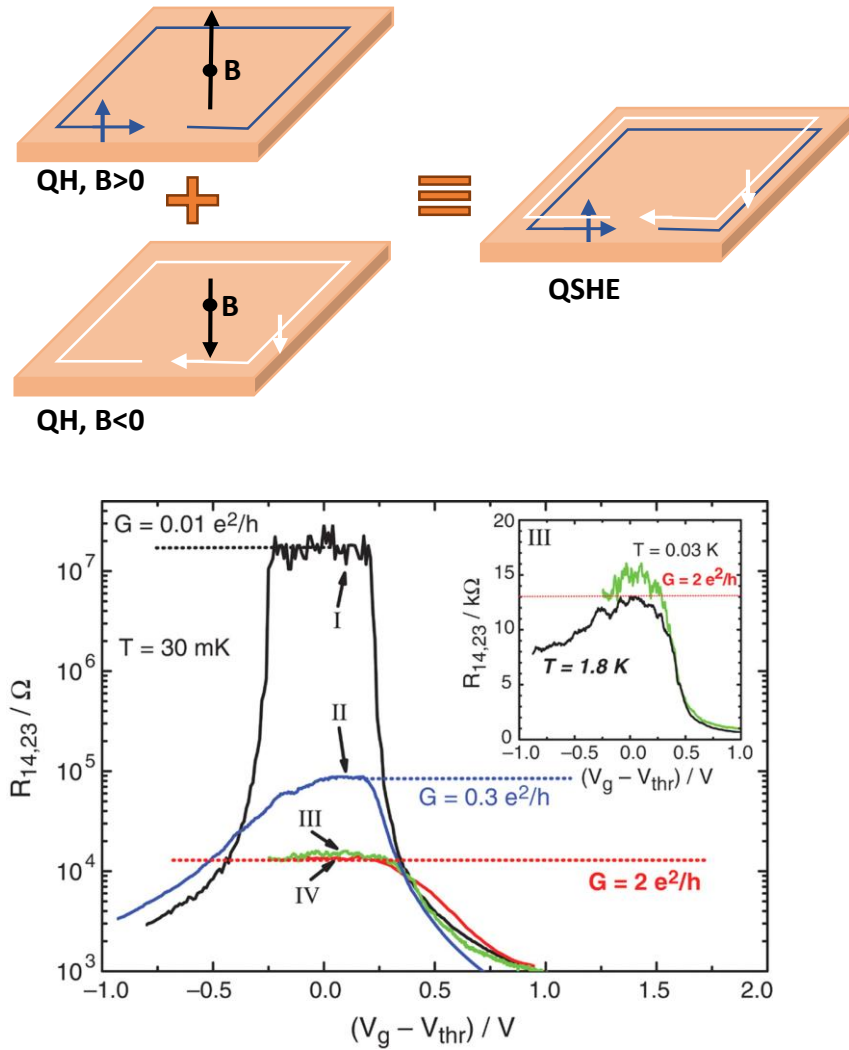
Figure 1.2: (top) Schematic diagram to understand quantum spin Hall effect. (bottom) quantum spin Hall effect realized on CdTe/HgTe/CdTe quantum-well structures at different gate voltages measured in zero magnetic field at 30 mK. [Image ref: [21]]

the subsystems look like two IQH systems in opposit direction of magnetic field. As a composite, the whole system can be considered as two spins propagating in opposite directions within the TRS protected edge states. The spin-orbit coupling acts as an effective magnetic field for the system [29]. The

electrons with spin-up and spin-down move in separate conducting channels. However, there is no net flow of charge, but net spin current in QSH systems.

1.1.2 Why the conduction channels are robust in QH systems:

The scattering causes resistance in any material. In QH systems the conduction channels can be related to a one-way traffic control system [30]. In the case of IQH systems, we do not bother about the electron spins. The electrons are spatially separated into different conduction channels at the edges of the sample. The idea of spatial separation makes it unique. As electrons have separate conduction channels, they do not see any impurity in the sample as there is no way to turn back, makes it topologically robust (Figure 1.3). In the case of QSH systems, each spin has different conduction channels. One can think of it as a four-lane traffic system. Similarly, the conduction channels in QSH systems are robust.

1.1.3 Topological invariant:

Topology is a branch of mathematics that deals with the properties of objects that are invariant under adiabatic deformations [31]. As example, (i) a plate and an apple are topologically equivalent or (ii) a coffee cup, and a doughnut is topologically equivalent. Both (i) and (ii) represent different topological classes because it is not possible to construct a doughnut from a plate without making any hole on it. All of these can be explained using Gauss-Bonnet theorem [32]. In an insulator, an energy gap separates the occupied valance
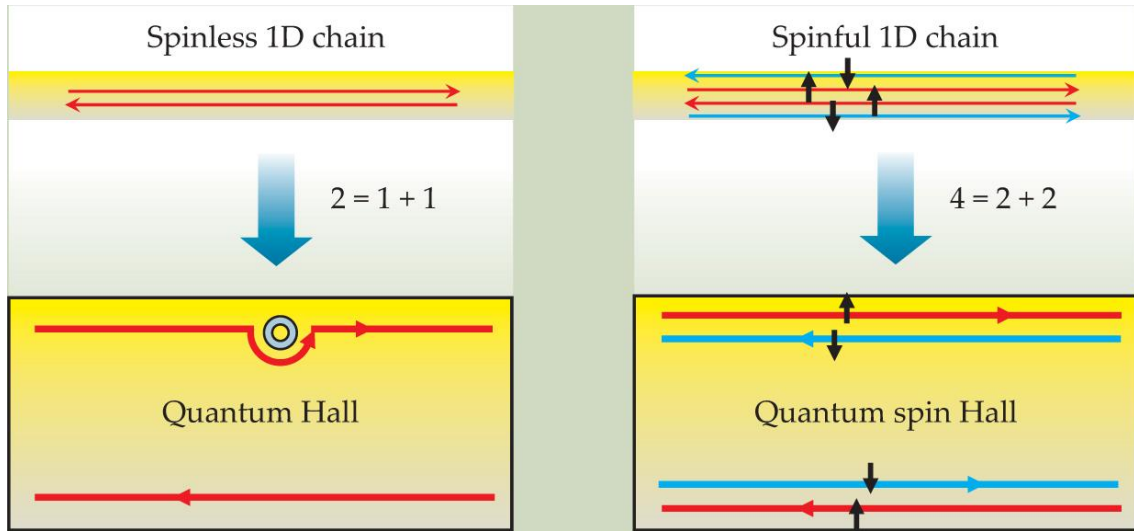
Figure 1.3: Spatial separation of charge/spin transport in the integer quantum Hall (IQH) and the quantum spin Hall (QSH) effects. (a) A spinless one-dimensional system with forward and backward transport. Two basic degrees of freedom are spatially separated: symbolic equation $2 = 1 + 1$. (b) A spinful 1D system has spatially separated four channels in a QSH bar: symbolic equation $4 = 2 + 2$. Image ref: [30]

band and the empty conduction band. Though the energy gap in an insulator is larger than a semiconductor, they are in a same topological class. One can transform the Hamiltonian of one into another via smooth deformation without closing the energy gap. According to this theory, all the insulators are topologically equivalent and are also equivalent to the *vacuum* described in the Dirac's relativistic quantum theory [33]. As it is shown in the previous section, there is a bulk-boundary correspondence which makes the problem topological. The different classes of topological systems are distinguished by topological invariants $n \in \mathbb{Z}$, where $\mathbb{Z}$ denotes integer numbers, known as Chern number. The Gaussian curvature in Gauss-Bonnet theorem is analogous to Berry curvature of electronic systems [32]. A periodic potential in a

solid state system can be expressed in terms of Bloch states $|u_m(\mathbf{k})\rangle$ which is the eigenstate of Bloch Hamiltonian $H(\mathbf{k})$. The electromagnetic vector potential is invariant under gauge transformation and it is analogous to the Berry connection can be written as, $\mathbf{A}_m = i \langle u_m | \nabla_\mathbf{k} | u_m \rangle$ [35]. The magnetic field is analogous to Berry curvature, $F_m = \nabla \times \mathbf{A}_m$. The line integral of the Berry curvature is Berry phase. The topological classes are characterized by the Chern numbers are the total Berry flux in the Brillouin zone,

$$n_m = \frac{1}{2\pi} \int d^2(\mathbf{k}) F_m \qquad (1.3)$$
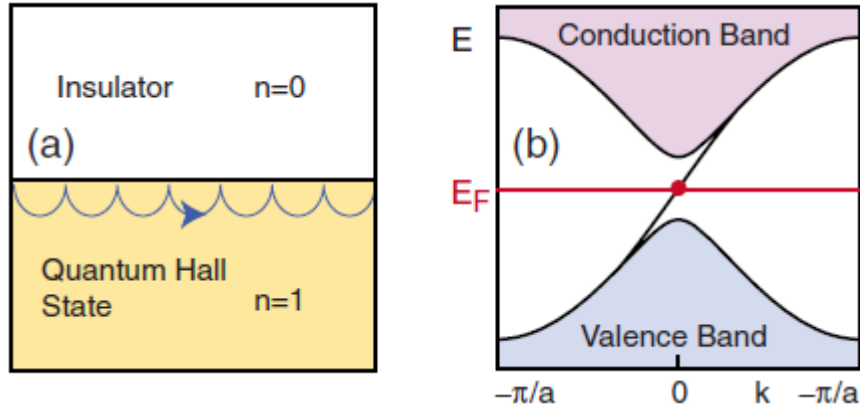
Figure 1.4: (a) Quantum Hall system has n=1 and a band isulator has n=0. At the interface skipping cyclotron orbits are seen. (b) In a band structure a single edge state connects the valance band and the conduction band. [32]

n_m is called Chern invariant, The total Chern number is summed over all occupied bands, $n = \sum_{m=1}^{N} n_m$, where the gap separation between valance band and conduction band remains finite. TKNN showed that the filling factor N in IQHE is equivalent to Chern number n [11]. In order to go from IQH state ($n = 1$) to the vacuum state ($n = 0$) through the smooth

deformation of the Hamiltonian, one has to close the gap at the boundary and as a result, the edge states formed in case of IQHE (Figure 1.4).

1.1.4 $\mathbb{Z}_2$ topological insulator:

In IQH systems, external high magnetic field breaks the TRS whereas no external magnetic field is needed for a QSH system. The edge states are remain TRS protected in QSH systems. Moreover, QSH systems are insulating in the bulk and have gapless edge states that are topologically protected by TRS and immune to non-magnetic impurities or geometric perturbations. The TR operator (Θ) in quantum mechanics is expressed as an anti-unitary operator, $\Theta = is_y K$ where s_y is y-component of Pauli spin matrices, and K is a complex conjugate operator. This relation gives a very important relation of TR operator, *i.e.* $\Theta^2 = -1$. If we consider a TRS preserved Bloch Hamiltonian of a system with energy eigenvalue E,

$$\hat{H} |\psi\rangle = E |\psi\rangle$$
$$\text{and, } H(-\mathbf{k}) = \Theta H(\mathbf{k})\Theta^{-1}$$

If $|\psi\rangle$ is a eigenstate of the Hamiltonian then $|\Theta\psi\rangle$ is also a eigenstate of the Hamiltonian because Θ is an anti-unitary operator. $|\psi\rangle$ and $|\Theta\psi\rangle$ cannot be linearly dependent for spin-$\frac{1}{2}$ particles because it gives the value of $\Theta^2 = 1$ [34]. The property $\Theta^2 = -1$ indicates that in a TR symmetric system, the energy bands comes in pairs (*i.e.* -$\mathbf{k}$ state and $\mathbf{k}$ state at same energy) which gives two fold degeneracy of the system, known as Kramer's degeneracy [35, 36]
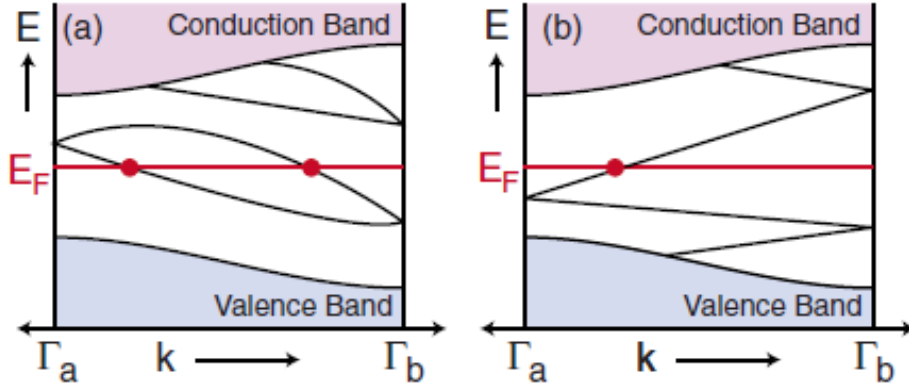
Figure 1.5: (a) The surface state crosses the Fermi level even number of times indiicates topologically trivial system. (b) The surface state crosses the Fermi level odd number of times indiicates topologically non-trivial system. Image ref: [32]

The TKNN invariant is valid for spinless systems only. For spinful systems, Kane and Mele introduced another topological invariant ν characterized by a novel topology specified by a $\mathbb{Z}_2$ index [37] which is related to the bulk-boundary correspondence. To elaborate it lets introduce two picture as shown in Figure 1.4. In Figure 1.5 band structure is shown from the range 0 to π/a because the $-\pi/a$ will be identical. The edge states are doubly degenerate and split due to spin-orbit coupling away from the high symmetry points. The edge states from one high symmetry point (0) to another high symmetry point (π/a) can be connected in two ways. Firstly, it may intercect the Fermi level in pairwise (Figure 1.5 (a)) or secondly, it may cross the Fermi level an odd number of times (Figure 1.5 (b)). In the first case, one can tune the position of the Fermi level (by deforming the Hamiltonian smoothly without changing the topological class) such a way so that the Fermi level lies in the gap or the edge states intersect the Fermi level even or zero number of times. This gives rise to the trivial nature of the edge states

(surface states in 3D). In the other picture, it is not possible to eliminate the edge states where it crosses the Fermi level an odd number of times. This corresponds to the nontrivial nature of the edge states (surface states in 3D) [32]. In mathematics, $\mathbb{Z}$ stands for a group of integer numbers. The index 2 in $\mathbb{Z}_2$ stands for two integer values; hence, a $\mathbb{Z}_2$ index generally gives a topological classification based on parity [35]. However, $\mathbb{Z}$ invariant can still be exist even if there there is no parity symmetry present in the system. Parity symmetry makes this invariant easier to calculate.

1.2 3D topological insulator:

Soon after the experimental discovery of QSHE, theorists predicted that this topological $\mathbb{Z}_2$ classification of insulators can be obtained in 3D systems as well [38–40]. As in QSH systems, the edges states are conducting residing in the bulk band gap, 3D TI has gapless TRS protected conducting surface states with a bulk band gap. There are four $\mathbb{Z}_2$ invariants $(\nu_0; \nu_1\nu_2\nu_3)$ needed to fully understand the topology [32] instead of one (ν_0) in 2D case. ν_0 is known as strong topological index whereas the others are known as weak topological indices. As mentioned above in Figure 1.5, if the surface state contains single (odd) number of Dirac cone then the system will be strong TI. Because, there is no backscattering channel open in this scenario makes it topologically robust. However, if the surface states contain odd (three, five,..., except one) number of Dirac cones then the system behave as a weak TI. Because, there are backscattering channels open in this scenario makes it topologically less robust.
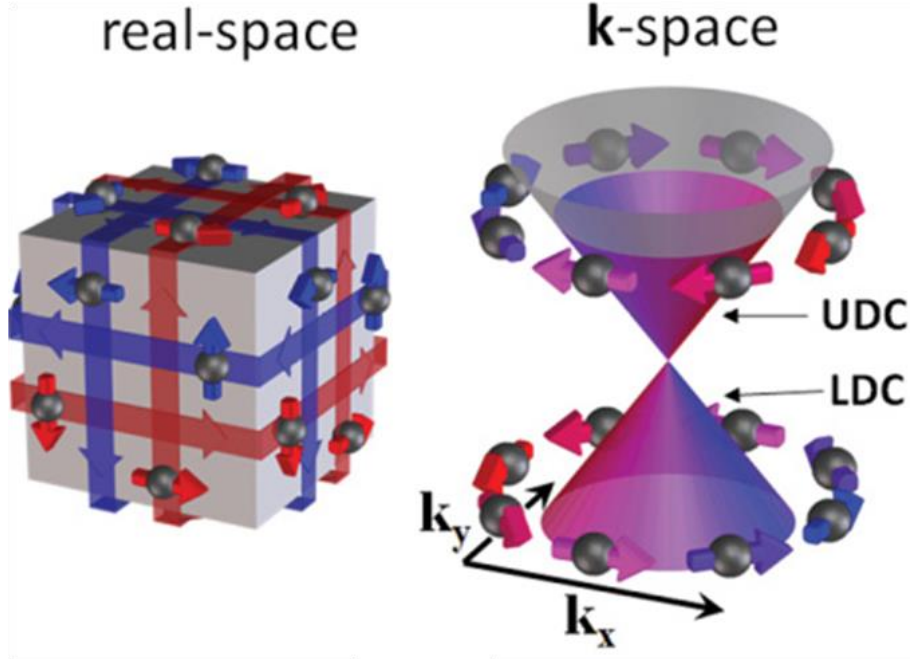
Figure 1.6: Spin-momentum locked topological surface states (left) in real space, (right)chiral spin texture in momentum space. UDC: upper Dirac cone, LDC: lower Dirac cone. Image ref: [35]

It can be shown that the charge carrier dynamics on the surface of a 3D TI is governed by the Dirac-type effective Hamiltonian can be written as,

$$H_s(k_x, k_y) = -\hbar v_F \hat{z} \times \overrightarrow{\sigma} \cdot \overrightarrow{k} \tag{1.4}$$

In conventional electronic systems, the dispersion relation is quadratic in nature whereas in 3D TI it follows a linear dispersion relation as shown in Figure 1.6 (right). One another important property of a 3D TI is that the spin of a charge carrier is in plane locked perpendicular to the momentum which is called spin-momentum locking. As an example, If spin-up charge carriers

are moving in the positive x-direction, then the spin-down charge carriers are bound to move in the negative x-direction, any mixture of these is prohibited (Figure 1.6 (left)). As a consequence, if any non-magnetic impurity falls on the way of the charge carriers, the spin has to flip in order to backscatter from the impurity state. The spin flipping is not allowed because it will cost enormous amount of energy to reach at the another edge of the sample. Therefore, this property makes the motion of the charge carriers topologically robust.

1.3   Experimental verifications:

The first discovered 3D topological insulator is $Bi_{1-x}Sb_x$. It was first predicted by Fu and Kane [22] and experimentally verified by M.Z. Hasan using ARPES measurements [4]. The nontrivial band topology can be mapped using angle-resolved photo-emission spectroscopy (ARPES). Later on, many TI materials are discovered, and Bi_2Te_3, Bi_2Te_3 are known as third-generation 3D-TI [41–44]. Using ARPES, we can map the band structure directly in the momentum space. Another powerful technique to detect the TI surface states is scanning tunnelling microscope (STM). Using STM, we can perform the local density of states (LDOS) mapping with varying energies in real space.

The topological surface states can be detected by analyzing the quasiparticle interference data(QPI) [45]. The charge carriers or quasiparticles scatter elastically from the impurities on the crystal which mixes the eigenstates of different momentum ($\mathbf{k}$) but in a same energy ($E(\mathbf{k})$) within the contour of constant energy (CCE) in momentum space. The incoming wave with wave

vector ($\mathbf{k}_1$) and the outgoing wave with wave vector ($\mathbf{k}_2$) interfere within the CCE and forms an interference pattern in the density of states [46]. This interference pattern can be observed by mapping the local density of state (LDOS) (or dI/dV mapping) using STM/S. The scattered quasiparticles form interference patterns around the defects and boundaries on the surface of a TI.

The scattering wave vectors can be obtained by taking Fourier-transform (FT) of the dI/dV map [45]. As in TSS, backscattering is prohibited, and this can be obtained from the suppression of the corresponding wave vector in the FT image [47,48]. One of the experimental evidence was obtained on MBE grown Bi_2Te_3 thin films. Some amount of Ag atoms were also deposited to act as an impurity state [47]. Figure 1.7 (a) and (b) show the standing waves induced by Ag atoms and the corresponding FT of the interference pattern respectively. From the FT image, it is clear that the intensity along the $\Gamma - M$ direction is much higher than the $\Gamma - K$ direction which implies that there is a suppression of particular wave vectors and theoretically it is shown that the suppression is due to the chiral spin texture (Figure 1.7 (c)). Another similar result was also observed on $Bi_{1-x}Sb_x$ alloy shown in Figure 1.7 (d) [45]. From these experiments, it is clear that the backscattering is forbidden on TSS. One interesting result on $Bi_{1.5}Sb_{0.5}Te_{1.7}Se_{1.3}$ shows that not only 180° but also wide-angle scattering ranging from 100° to 180° is also prohibited.

Another method to detect the TSS is Landau level spectroscopy [49,50]. Using this technique, one can directly map the oscillations in density of states with respect to energy.
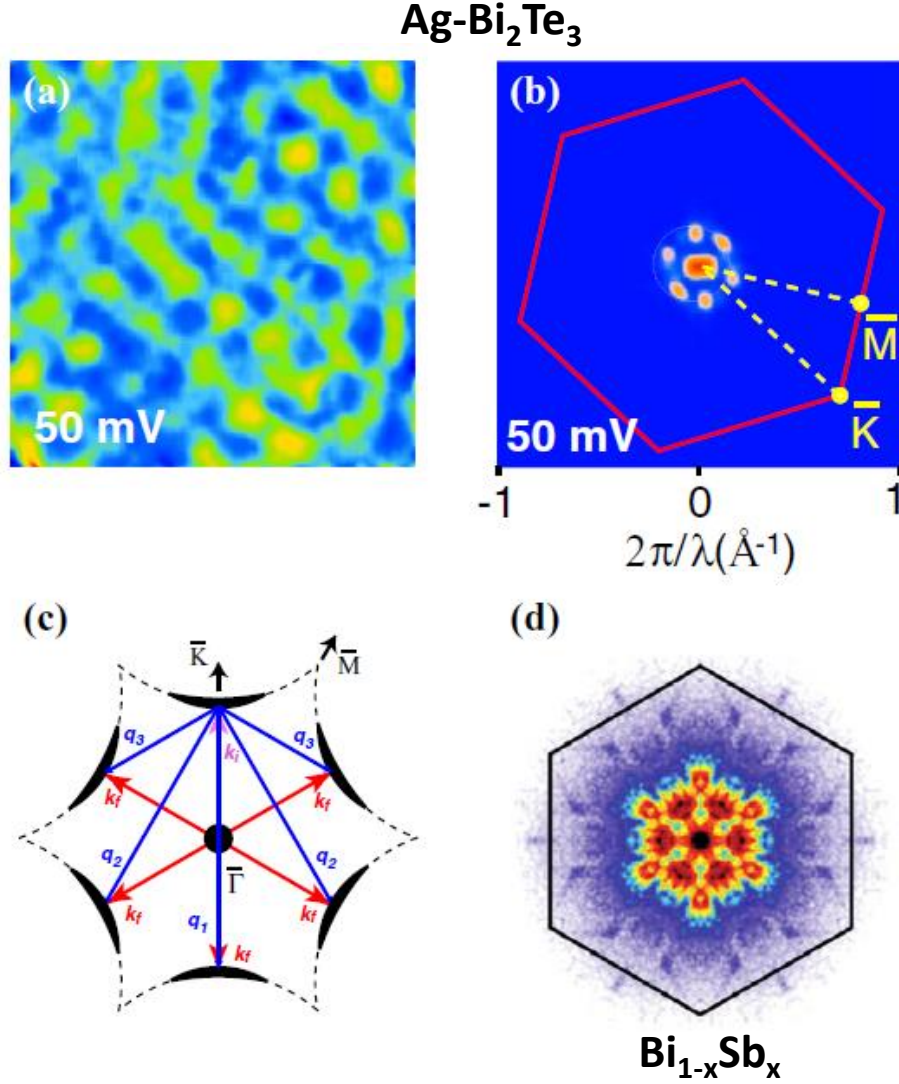
Ag-Bi$_2$Te$_3$

Figure 1.7: (a) Quasiparticle interference image on Ag-Bi$_2$Te$_3$ thin film. (b) Fourier transformed image of the QPI at 50 mV. (c) theoritical modeling of the above image. (d) Fourier transformed image of QPI in BI$_{1-x}$Sb$_x$. Image ref: [48]

As shown in Figure 1.8 in the presence of high magnetic field the oscillations in DOS ($\equiv dI/dV$) is clearly visible [49, 50]. TSS of a 3D TI can be considered as a 2D system and in the presence of magnetic field, the energy levels quantized into Landau levels. Landau level spectroscopy can be per-
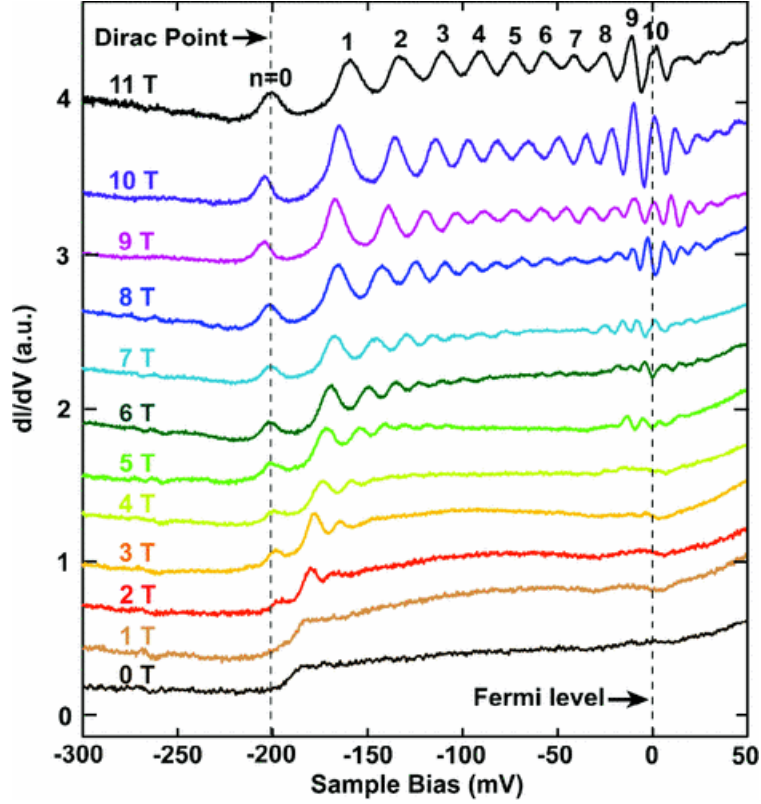
Figure 1.8: Landau level spectroscopy on Bi_2Se_3 thin film. Landau levels are formed at high magnetic fields. Image ref: [50]

formed using STM. The above result is shown on MBE grown Bi_2Se_3 thin film of 50 QL. With increasing magnetic field the oscillation increases and the quantization numbers are easily countable. These oscillations can also be seen in conductivity and magnetic susceptibility measurements. The oscillations arise in conductivity is called Shubnikov–de Haas (SdH) oscillations [51], while the oscillations arise in magnetic susceptibility is called de Haas–van Alphen (dHvA) oscillations [52, 53]. In SdH/dHvA oscillations, conductivity/susceptibility oscillates periodically with magnetic field and poltted as a function of 1/B .Utilizing this phenomenon one can also calculate the Berry

phase and the value which is associated with the topological nature of the surface state. The Berry phase which is zero for an electronic system with parabolic energy dispersion and π for linear energy dispersion associated with Dirac fermions [35].

1.4 Symmetry operations: different topological classes:

The gapless surface states of a 3D TI are protected by TRS. After discovering 3D TI, people became more interested in looking for new quantum matters with nontrivial surface states protected by other symmetries by controlling the interplay between the symmetry and topology of the electronic band structure [54–65].

In 1929, Dirac wrote down his equation for the electron involving complex 4×4 matrices [66], Weyl comes out with another simplified relativistic equation using the 2×2 complex Pauli matrices σ_n in the Dirac equation considering fermions to be massless. Weyl fermions are associated with a chirality [67]. A Dirac fermion can be expressed as a pair of opposite chirality Weyl fermions [68].

After the discovery of 3D TI, it was predicted that the Dirac semimetallic phase could be obtained at a quantum critical point in the phase transition between a trivial insulator and a TI [54, 59, 61]. This can be realized experimentally by an optimal amount of doping, applying pressure, etc. on the parent material. According to the symmetry operation, one can achieve a

Dirac semimetallic phase if both the TRS and IS is preserved in the system. At this quantum critical point, the top of the valance bands and bottom of the conduction bands touch in the momentum space and form a Dirac cone (Figure 1.9 (a), (b)). Doping a known topological insulator with lighter elements by tuning spin-orbit coupling or lattice constant may close and invert the band gap at a quantum critical point which has been investigated in many materials [58, 59, 69, 70]. The 3D Dirac point has four-fold degeneracy, and it does not carry a Chern number [54]. It is observed that the degeneracy can be lifted by applying small external perturbations. However, a stable 3D Dirac semimetallic phase can be achieved if the system preserves crystalline symmetries such as rotation symmetry, reflection symmetry in addition to TRS and IS (Figure 1.9 (b)). Na_3Bi, Cd_3As_2 are the stable 3D Dirac semimetals have Dirac linear dispersion in three momentum directions [62, 63] .
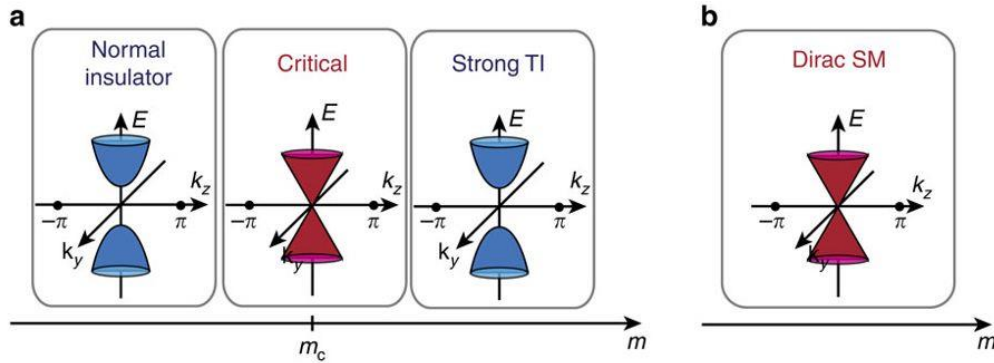
Figure 1.9: (a) Dirac semimetal phase is arising in a quantum critical point. (b) A stable Dirac semimetal. Image ref: [54]

The Dirac semimetals are also characterized by the property of the Dirac cone. In type I 3D Dirac semimetals the Dirac cone meets at the Fermi surface whereas in type II Dirac semimetals the Dirac cone is tilted which

crosses the Fermi surface and creates electron/hole pockets (Figure 1.10). Due to this nature the type I systems are semimetals (eg. Na_3Bi, Cd_3As_2) whereas type II are metals (eg. $PdTe_2$, $PtSe_2$, WTe_2 and $MoTe_2$) [71–76].
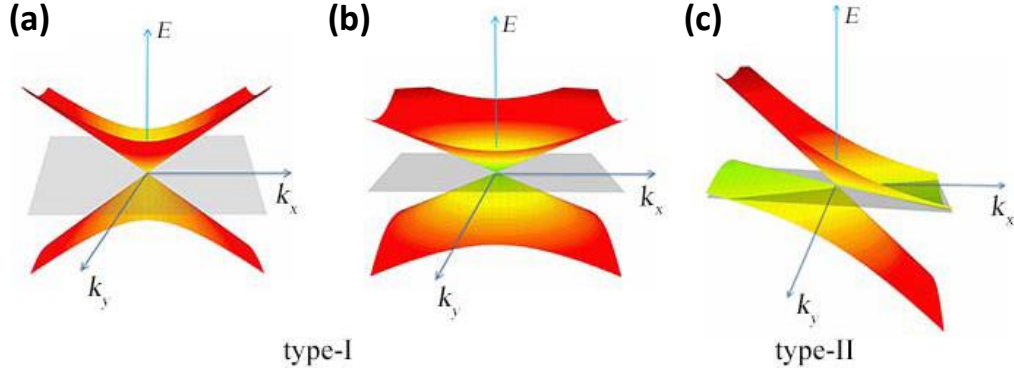
Figure 1.10: (a) Type I Dirac semimetal. (b) Type Dirac semimetal crosses the fermi level and creates a electron/hole pocket. Image ref: [74]

It was also predicted that by breaking one of the symmetries between TRS and IS one can realize another quantum phase of matter known as Weyl semimetal (WSM) [77]. Due to the broken symmetry, the four-component Dirac cone splits into two pair of Weyl cones associated with Weyl fermions and forms a new kind of surface state known as Fermi arc. In a band structure calculation with SOC the Weyl nodes can be obtained at a generic momentum position rather than any high symmetry points. In a WSM the pair of Weyl nodes are connected through an open Fermi arc in one surface and then continue to the opposite surface [78]. The Fermi arcs are tangent to the bulk Fermi surface states onto the surface Brillouin zone [79]. This Fermi arc can be realized in ARPES [80], STM [81] experiments.

Other than topological semimetals, there is another class of material known as topological crystalline insulator (TCI). The topological phase of

this quantum matter is protected by crystal symmetry such as rotation, reflection symmetry, etc. The surface which preserves the rotational/reflection symmetry supports gapless surface states [82, 83]. TCIs are the counterpart of TIs without SOC. The topology of a TCIs is characterized by mirror Chern number. The first discovered TCI was SnTe (IV-VI semiconductor) [5]. It was shown that an even number of Dirac points cut the Brillouin zone. Apparently, according to the $\mathbb{Z}_2$ topology it should be topologically trivial, but the protection of mirror symmetry makes it topologically nontrivial characterized by mirror Chern number. Later on it is shown that $Pb_{1-x}Sn_xSe$, $Pb_{0.6}, Sn_{0.4}Te$ are also TCI but $Pb_{0.8}Sn_{0.2}Te$ is not. The QPI study using STM on $Pb_{1-x}Sn_xSe$ showed four surface pockets which were consistence with the ARPES measurements [84, 85]. Quantum oscillations were obtained from the Landau level spectroscopy on the same material [86]. Therefore, the TCI materials are also a great interest to study.

1.5 Role of SOC in topological insulators:

Spin-orbit coupling plays a key role to explain and discover new topological states of matter. Mostly, the compounds with the composition of heavy elements exhibit topological phase transition [87]. Those heavy elements manifest strong bulk spin-orbit interaction. In the topological insulator edge/surface states are characterized by helical spin textures. A concrete theoretical study on the role of SOC for topological insulator has been explained by H. Zhang *et. al.* [23]. In this paper, they have shown that without SOC the band structure of the system remained a band insulator, but by turning on

the SOC, a band inversion occurred around the Γ point which indicates that the system is a TI. The studied systems were Bi_2Se_3, Bi_2Te_3, Sb_2Te_3, Sb_2Se_3. Among them, the first three systems show topological phase transition which is also proved experimentally [24, 25, 43, 88–91]. Due to the weak spin-orbit interaction Sb_2Se_3 do not undergoes band inversion. (Figure 1.11). The momentum dependent splitting of the spin bands in two-dimensional condensed matter systems is known as Rashba SOC. This type of SOC arises from the structural symmetry breaking. In a single crystal, along the crystal growth direction on the clevage surface the inversion symetry (IS) is always broken. The lack of IS generates asymetric crystal potentical which gives rise to the Rashba type of SOC. The Rashba Hamiltonian can be written as [92],

$$\hat{H}_R = \frac{\alpha_R}{\hbar} \left(\overrightarrow{\sigma} \times \overrightarrow{p} \right) \cdot \overrightarrow{z} \tag{1.5}$$

where, **p** is momentum, σ is Pauli spin matrices, **z** is direction of intrinsic electric field, α_R is Rashba parameter can be expressed as, $\hbar\mu_B E_0/mc^2$. μ_B is Bohr magnetron.

The 3D TIs can be considered as a 2D surface states, and those are characterized by Rashba SOC. Due to the chiral spin texture of the topological surface states, a current through the surface states will be 100 % spin-polarized. One interesting transport experiment performed on a thin film of Bi_2Se_3 to show the tunability of the Rashba SOC by changing the gate voltage [94]. The surface spin polarization can be measured using spin-resolved point-contact Andreev reflection spectroscopy [95] (discussed in the Section 1.7).
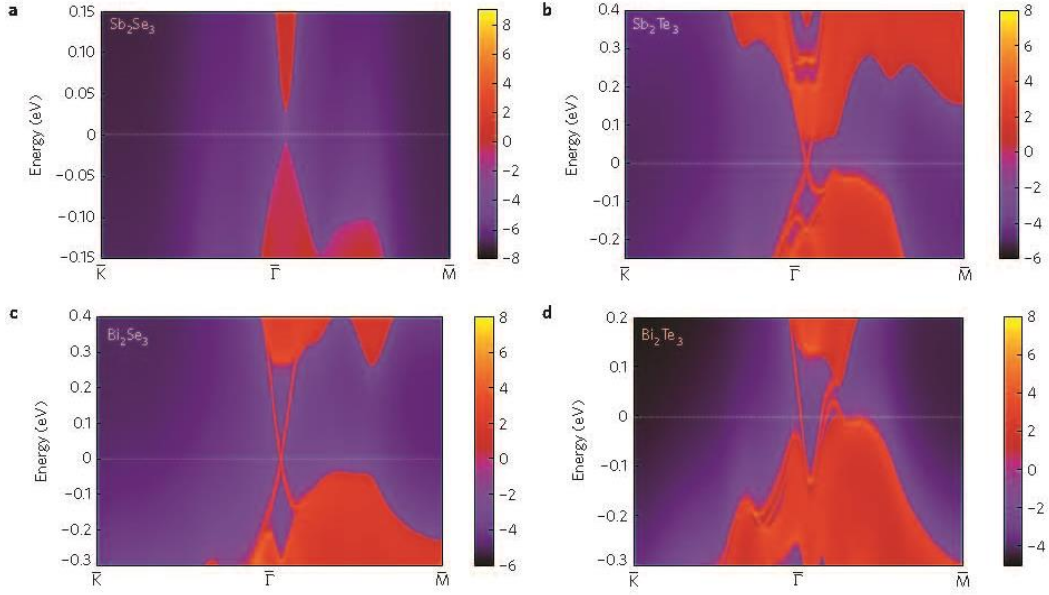
Figure 1.11: Band structure calculation with spin-orbit coupling in (a) Sb_2Se_3, (b) Sb_2Te_3, (c) Bi_2Se_3, (d) Bi_2Te_3. Image ref: [23]

1.6 Topological superconductors:

Topological superconductivity (TS) can be interpreted as topological insulator along with superconductivity [93]. This can be intrinsic property of the system or induced by proximity effect. The key indication of realizing TS is the formation of Majorana bound state (MBS) [96]. It is predicted that Majorana fermion which is its own antiparticle might act as an elementary exitation for TS. The experimental signature to obtain this state is zero bias conductance peak in a tunnelling spectrum at certain magnetic fields [97]. The most MBS theories predict that for the tunnelling manifestations of MBS involve strong spin-orbit coupling [98, 99]. As I described earlier that SOC has very important role to design a topological states of

matter. Therefore, there is a possibility to realize topological superconductivity in these systems. It is also predicted that conventional (spin-singlet, s-wave) superconductors in a combination with a topological insulator could be a TS [100]. There are many experiments realized zero bias conductance peaks which could be the signature of MBS [101–105]. However, their are other possibilities for the zero bias peaks such as, Kondo effect [106], weak antilocalization [107]. However, this can be ruled out through careful device design and parameter dependent observation [105] such as the splitting of the zero bias conductance peak with magnetic field [101], no zero bias anomaly along the spin-orbit field [97]. However, the concrete proof of realizing MBS is still elusive as all the conditions do not fulfil in a single system. Therefore, realizing topological superconductivity is an active area of research.

1.7 Spin-polarization measurement of a TI:

As I mentioned earlier that the surface state of TI is spin polarized and the current through the surface state will also be spin-polarized. People have measured this spin polarization using many techniques [108–111]. Here, I will introduce a more simpler technique which can measure the spin polarization of a TI. Using spin-polarized point contact Andreev reflection (SP-PCAR) spectroscopy, one can measure the spin-polarization of a topological surface states (TSS). Before going into the details, let us introduce the PCAR spectroscopy first.

1.7.1 PCAR spectroscopy:

Andreev reflection occurs at the interface between a superconductor and a normal metal [112]. PCAR spectroscopy [113–116], the study of energy dependent differential conductance of a mesoscopic confined region, is a popular technique practiced over decades to probe the electron-phonon interaction in metals. This technique is utilized to characterize superconductors, in particular, to find the superconducting gap amplitude, symmetry of the order parameter *etc.* A tiny confined region referred as a point-contact (PC) can simply be realized by touching two pieces of same/different materials physically known as needle-anvil method [113]. However, the PC can be achieved through other methods such as share method, break junction method, lithographic device [113]. Typically the size of such constriction (= diameter when the cross-section is assumed circular) is ~ 1 Å to few hundreds of

nanometer (nm). The PC diameter is comparable with the characteristic length-scales [117] like mean free path or de Broglie wavelength or coherence length of electrons or quasi-particles for the materials forming the junction. A simple $I - V$ measurement gives lots of information about the materials. The $I - V$ characteristic curve changes their behavior and corresponding differential conductance spectrum $dI/dV - V$, known as PC spectra, is expected to exhibit characteristic signatures depending upon the chosen materials and size of the contacts. The size of the PC relative to the elastic and inelastic mean free paths defines the regime of mesoscopic transport, and the PC resistance can be deduced from Wexler's formula [118]:

$$R_{PC} = \frac{2h/e^2}{(ak_F)^2} + \Gamma(l/a)\frac{\rho(T)}{2a} \qquad (1.6)$$

Where h is the Planck's constant, a is the point-contact diameter, e is the charge of an electron, k_F is the Fermi wave vector, l is electronic mean free path, $\Gamma(l/a)$ is a slowly varying function varies from 0.7 to 1 depending upon electronic mean free path and contact diameter, ρ is the bulk resistivity of the material, and T is the temperature at the point-contact. Here, The first term is known as Sharvin's resistance (R_S), and it is independent of the temperature and the bulk resistivity of the materials. The corresponding PC is called ballistic PC [119]. Furthermore, the second term is known as Maxwell's resistance (R_M) which depends directly on the resistivity of the materials. The corresponding PC is called thermal PC [119]. The above equation clearly reveals when the contact diameter is small compared to the electronic mean free path R_S dominates and when the contact diameter is

large R_M dominates. Therefore, by varying the contact diameter, one can go from the ballistic PC to thermal PC. In between the ballistic regime and the thermal regime, It is also possible to get an intermediate regime called a diffusive regime where energy resolved spectroscopy is possible through Andreev reflection spectroscopy. However, all of the above, another PC regime is possible, known as quantum regime. When the point-contact diameter is in the order of the de-Broglie wavelength, then conductance gets quantized, which is given by $G_0 = N \times \frac{2e^2}{h}$, where N is the number of the conducting channels [120]. Remember, this quantization equation is similar to the quantization in QHE.
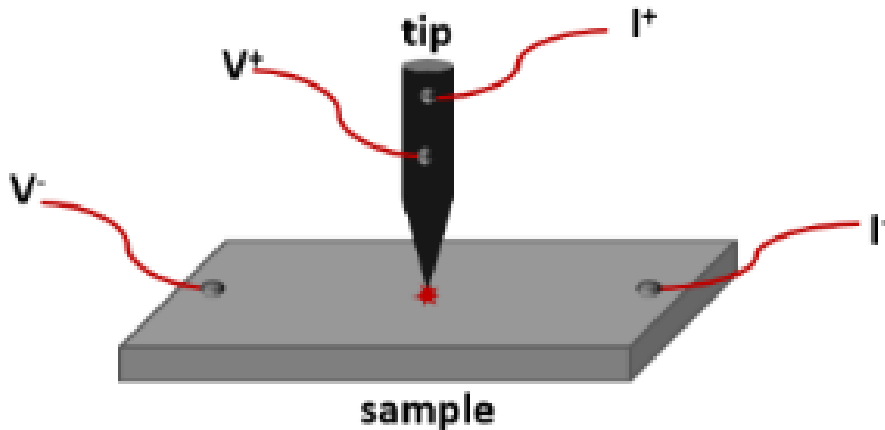
Figure 1.12: Schematic of a point-contact measurement: A pseudo four probe method.

The schematic diagram of the measurement shown in Figure 1.12. Few representative PC spectra for different regimes of PC shown in Figure 1.13. Here, it can be shown that dI/dV is directly proportional to the density of states of the material.
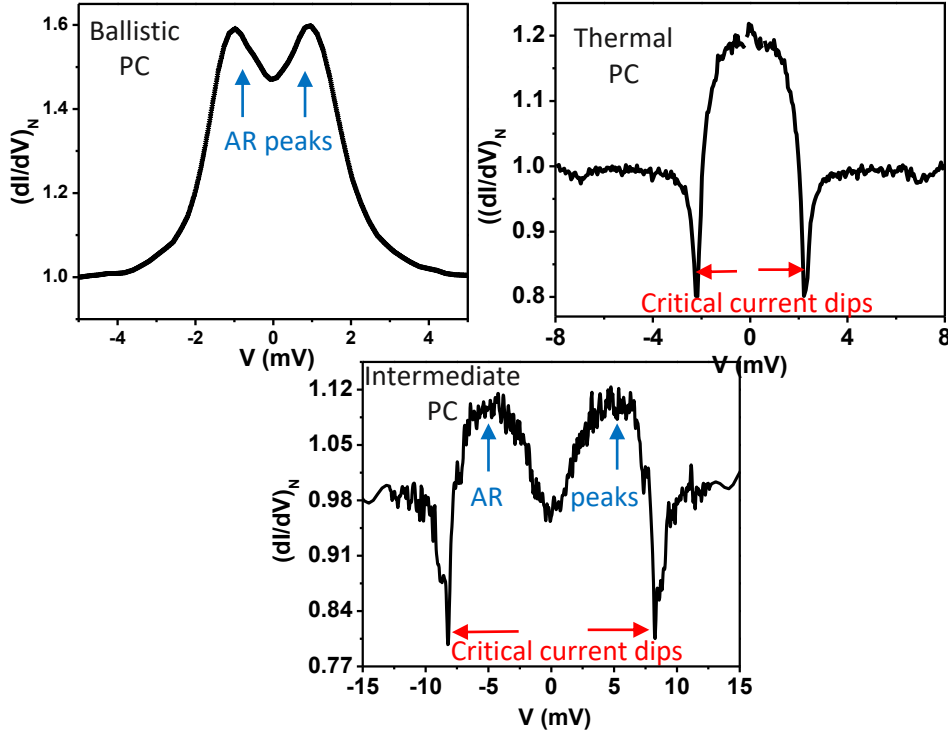
Figure 1.13: Different regimes of point-contacts.

A schematic diagram of the Andreev reflection process in the PC geometry is shown in Figure 1.14. When the energy of an electron (hole) in the normal metal side is less than the superconducting energy gap the incident electron (hole) forms a Cooper pair in the superconductor and due to momentum conservation, a hole (electron) with the opposite spin reflects back. One can measure the superconducting order parameter (Δ) by fitting a ballistic limit experimental $dI/dV - V$ spectrum with a theoretical model is known as BTK (Blonder, Tinkham, and Klapwijk) theory [121]. However, in BTK theory only the elastic scattering was accounted at the interface, but practically the electrons also experience inelastic scattering. In order to compensate the discrepancy, one another parameter associated with quasiparticle lifetime

was added in the modified BTK model [122]. The formalism of the modified theory is depicted below.
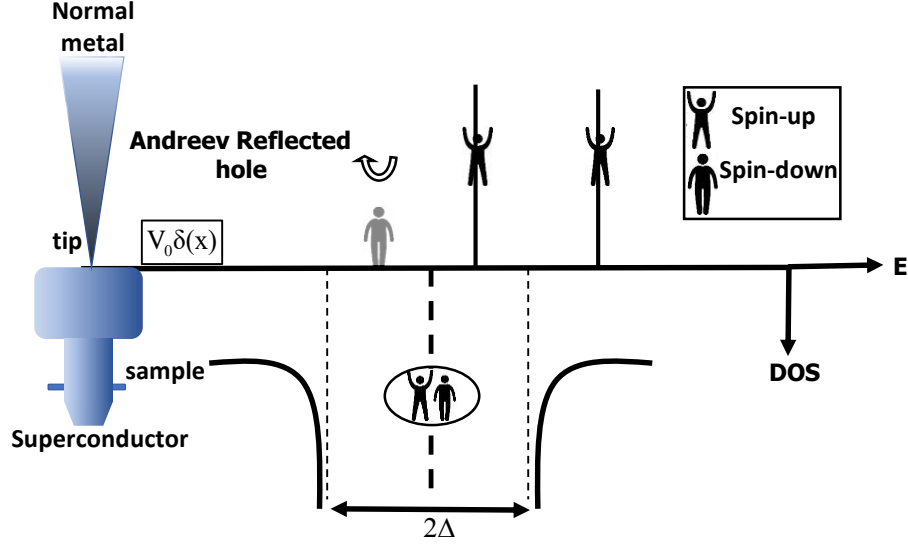
Figure 1.14: Andreev reflection in a point-contact between a normal metal and a superconductor

1.7.2 Modified BTK formalism:

The one dimentional model employed to analyze the PCAR spectrum is proposed by Blonder, Thinkham and Klapwijk (BTK) [121]. They considered a normal-superconducting (NS) microconstriction contacts spanned from metallic to tunnel junction behavior. In this model, the N/S interface is considered as a delta function, $H = V_0\delta(x)$ and the barrier height is expressed as a dimensionless parameter $Z = \dfrac{V_0}{\hbar v_F}$, where, v_F is Fermi velocity. For the systems where the difference between the Fermi velocities is large, the effective Z can be written as $Z_{eff} = Z + \frac{(1-r)^2}{4r}$, here $r = v_{F_N}/v_{F_S}$. The Bogoliubov-de Gennes [123] equations can be written as follow:

$$\iota\hbar\frac{\partial f(x,t)}{\partial t} = \left[\frac{\hbar^2\nabla^2}{2m} + \mu(x) + \iota\Gamma - V(x)\right]f(x,t) + \Delta(x)g(x,t) \qquad (1.7)$$

$$\iota\hbar\frac{\partial g(x,t)}{\partial t} = \left[\frac{\hbar^2\nabla^2}{2m} + \mu(x) + \iota\Gamma - V(x)\right]g(x,t) + \Delta(x)f(x,t) \qquad (1.8)$$

where, $\Delta(x)$ is the energy gap, $\mu(x)$ is the chemical potential, $\Gamma = \hbar/\tau$ is the quasiparticle lifetime. Here, we consider a wave function for electron and hole as,

$$\psi = \begin{pmatrix} f(x,t) \\ g(x,t) \end{pmatrix} \qquad (1.9)$$

$f(x,t)$ and $g(x,t)$ are electron and hole wave function respectively.

The boundary conditions for particles moving at $x = 0$ from normal metal to superconductor are as follow:

(i) $\Psi_S(0) = \Psi_N(0)$

(ii) $(\hbar^2/2m)(\Psi'_S - \Psi'_N) = H\Psi_N(0)$

Then incident, reflected and transmitted wave functions are:

$$\Psi_{in} = \begin{pmatrix} 1 \\ 0 \end{pmatrix} e^{\iota kx} e^{-\iota Et/\hbar} \qquad (1.10)$$

$$\Psi_{re} = \left[a\begin{pmatrix} 0 \\ 1 \end{pmatrix} e^{\iota kx} + b\begin{pmatrix} 1 \\ 0 \end{pmatrix} e^{-\iota kx}\right] e^{-\iota Et/\hbar} \qquad (1.11)$$

$$\Psi_{tr} = \left[c \begin{pmatrix} u_k \\ v_k \end{pmatrix} e^{\iota kx} + d \begin{pmatrix} v_k \\ u_k \end{pmatrix} e^{-\iota kx} \right] e^{-\iota(E+\iota\Gamma)t/\hbar} \tag{1.12}$$

u_k^2 and v_k^2 are the probabilities of an electronic state being occupied and unoccupied respectively:

$$1 - v_k^2 = u_k^2 = \frac{1}{2} \left[1 + \frac{\sqrt{(E + \iota\Gamma) - \Delta^2}}{E + \iota\Gamma} \right] \tag{1.13}$$

Where coefficients a and b are given by,

$$a = \frac{u_k v_k}{\gamma} \tag{1.14}$$

$$b = \frac{-(u_k^2 - v_k^2)(Z^2 + \iota Z)}{\gamma} \tag{1.15}$$

where,

$$\gamma^2 = \gamma\gamma^*; \quad \gamma = u_k^2 + (u_k^2 - v_k^2)Z^2 \tag{1.16}$$

If electrons tunnel through an NS junction then the number of occupied states is $N_N(E)f(E)$ and number of unoccupied states is $N_S(E - eV)[1 - f(E - eV)]$. Here, $N_N(E)$ is density of states of the normal metal, $N_S(E)$ is density of states of the superconductor and $f(E)$ is the Fermi function. For the forward current joint probability for this process is $N_N(E)f(E)N_S(E - eV)[1 - f(E - eV)]$. For the reverse current joint probability for this process is $N_N(E)f(E - eV)N_S(E - eV)[1 - f(E)]$. The net current through an NS

junction is (forword-reverse) [115, 121]

$$I_{NS} = \alpha \mid T \mid^2 \int_{-\infty}^{+\infty} N_N(E) N_S(E - eV)[f(E) - f(E - eV)]dE \qquad (1.17)$$

where α is the constant that depends upon the junction and Fermi velocity and $\mid T \mid^2$ is a tunnelling matrix element that depends on the type of insulator between the NS junction. If we assume that the density of states of the normal metal nearly flat near the Fermi level then $N_N(E) = N_N(0)$ and the differential conductance at T= 0 is given as follows:

$$G_{NS} \equiv \frac{dI_{NS}}{dV} \mid_{T=0} \propto N_S(e \mid V \mid) \qquad (1.18)$$

where, the differentiation of the Fermi functions acts as a Dirac delta function.

Now, we use the BTK formulation with Andreev reflection (AR). The current that propagate across the NS junction is:

$$I_{ballistic} \propto \int_{-\infty}^{+\infty} [f(E) - f(E - eV)][1 + A_u(E) - B_u(E)]dE \qquad (1.19)$$

where, $A_u(E)$ is the AR probability and $B_u(E)$ is the normal reflection probability and $A_u(E) = aa^*$ and $B_u(E) = bb^*$.

The expression for the dI/dV of an NS junction corresponding to the AR process at $T = 0$ is given as below:

$$G_{ballistic} = \frac{dI_{NS}}{dV} \mid_{T=0} \propto (1 + A_u(eV) - B_u(eV)) \qquad (1.20)$$

E	$A_{\mathrm{u}}(E)$	$B_{\mathrm{u}}(E)$
$E < \Delta$	$\dfrac{\Delta^2}{(E + \iota\Gamma)^2 + (1 + 2Z^2)^2[\Delta^2 - (E + \iota\Gamma)^2]}$	$1 - A(E)$
$E > \Delta$	$u_k^2 v_k^2/\gamma^2$	$(u_k^2 - v_k^2)^2 Z^2(1 + Z^2)/\gamma^2$

Table 1.1: Values of $A_u(E)$ and $B_u(E)$.

Here, $1 + A_u(E) - B_u(E)$ [121] depicts the transmission coefficient for the net current. This term can be described in the following way: Let's say, the incident charge carrier is an electron and the current is considered as unity. Now, the Andreev reflected hole has a positive charge which moves in the opposite direction of the incident electron is represented by $A_u(E)$. The current generated due to electron and the hole will add up which is $1 + A_u(E)$. Now, if the incident electron reflects from the barrier which is represented by $B_u(E)$ that will reduce the forward current *i.e.* $1 + A_u(E) - B_u(E)$.

Now, for $Z = 0$, there will be only Andreev reflection. However, for strong surface barrier $(Z^2(u^2 - v^2) >> 1)$, The AR will suppress and go to quantum tunnelling regime. One can formulate the tunnelling spectra directly from equation 1.17,

$$I_T = \beta \mid T \mid^2 \int_{-\infty}^{+\infty} N_S(E - eV)[f(E) - f(E - eV)]dE \qquad (1.21)$$

Here, the density of states of the normal metal can be considered as a constant within the energy range of the superconducting energy gap. This equation is also known as Dynes equation which was known before BTK gave his theory [124]. The superconducting density of states can be written as,$N_S(E) = Re\left(\frac{E - \iota\Gamma}{\sqrt{(E - \iota\Gamma)^2 - \Delta^2}}\right)$. The representative simulated tunnelling

spectra are shown in Figure 1.15. At $T = 0$, two sharp coherence peaks are clearly visible whereas at nonzero finite temperature the overall spectrum broadened and this broadening is taken care of using the parameter Γ. In a point contact geometry where the tip and sample touch physically, is nearly impossible to get a tunnelling limit spectrum. However, in STM, where the tip and sample do not touch physically rather than stays in the quantum tunnelling limit and the tip to sample distance can be maintained using a feedback mechanism. The expected tunnelling regime spectra are shown in Figure 1.15.
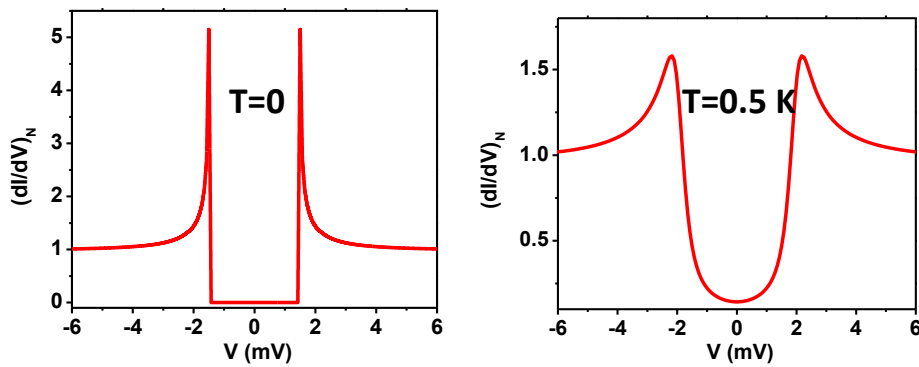
Figure 1.15: Tunnelling spectra for normal metal and superconductor in STM

Replacing normal metal with a ferromagnetic metal: The Andreev reflection process is highly spin dependent. As mentioned earlier, in the N/S point-contact the incident spin up electron gives rise to spin down hole or vice versa. Now, we replace the normal metal with a ferromagnetic metal. Due to the spin dependent band in the ferromagnetic metal, there are less probability to find the opposite spin band. Hence, the Andreev reflection will suppress. The process is illustrated in Figure 1.16. By measuring the sup-

pression of the Andreev reflection one can measure the spin-polarization of
the ferromagnet [125–128]. The spin-polarization of a ferromagnet is defined
as,

$$P = \frac{N_\uparrow(E_F) - N_\downarrow(E_F)}{N_\uparrow(E_F) + N_\downarrow(E_F)} \tag{1.22}$$

where, $N_\downarrow(E_F$ is the density of state of the down spin electron at the Fermi
level. However, in the transport experiment the spin-polarization involves
current densities which can be written as,

$$P_t = \frac{J_\uparrow - J_\downarrow}{J_\uparrow + J_\downarrow} \tag{1.23}$$

where, $J_\downarrow$ is the current density of the down spin electron at the Fermi level
which is $\langle N_\downarrow(E_F) \cdot v_F \rangle$ for ballistic point-contacts and $\langle N_\downarrow(E_F) \cdot v_F^2 \rangle$ for dif-
fusive point-contacts [129].
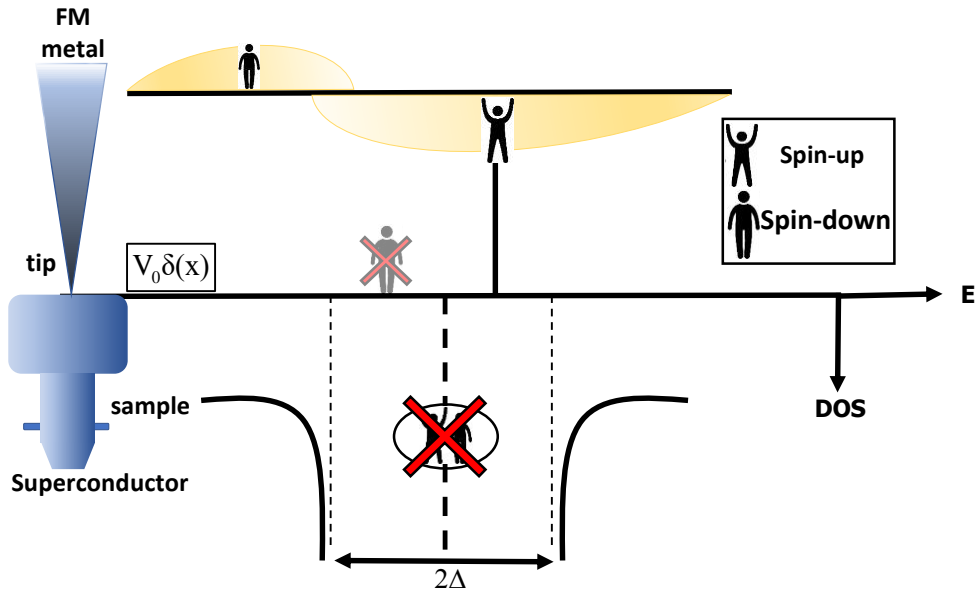
Figure 1.16: Suppression of Andreev reflection in a point-contact between
ferromagnetic metal and a superconductor

As the Andreev reflection is suppressed in F/S point-contact the BTK model will be modified accordingly. In the BTK model the modified electronic wave functions will be,

$$\Psi_{in} = \begin{pmatrix} 1 \\ 0 \end{pmatrix} e^{\iota kx} e^{-\iota Et/\hbar} \tag{1.24}$$

$$\Psi_{re} = \left[a \begin{pmatrix} 0 \\ 1 \end{pmatrix} e^{\kappa x} + b \begin{pmatrix} 1 \\ 0 \end{pmatrix} e^{-\iota kx} \right] e^{-\iota Et/\hbar} \tag{1.25}$$

$$\Psi_{tr} = \left[c \begin{pmatrix} u_k \\ v_k \end{pmatrix} e^{\iota kx} + d \begin{pmatrix} v_k \\ u_k \end{pmatrix} e^{-\iota kx} \right] e^{-\iota (E+\iota\Gamma)t/\hbar} \tag{1.26}$$

Using these wave functions one can calculate the $A_p(E)$ and $B_p(E)$.

E	$A_{\mathrm{p}}(E)$	$B_{\mathrm{p}}(E)$
$E < \Delta$	0	1
$E > \Delta$	0	$B_{\mathrm{p}}(E) = \dfrac{\left(\sqrt{(E^2-\Delta^2)/E^2}-1\right)^2 + 4Z^2\left(E^2-\Delta^2\right)/E^2}{\left(\sqrt{(E^2-\Delta^2)/E^2}+1\right)^2 + 4Z^2\left(E^2-\Delta^2\right)/E^2}$

Table 1.2: Values of A_p(E) and B_p(E)

The modified current will be,

$$I_{mod} = (1 - P_t)I_u + P_t I_p \tag{1.27}$$

From this equation it is clear that when $P_t = 0$ the total current is simple unpolarized current which can be obtained from the simple BTK theory. It should be noted that the interface scattering is assumed to be spin indepen-

dent for simplicity.

The variation in spin-polarization is shown in Figure 1.17 simulated using spin-polarized BTK formalism. Due to the suppression of the Andreev reflection at 100 % spin-polarization the density of states is essentially approaches to zero.
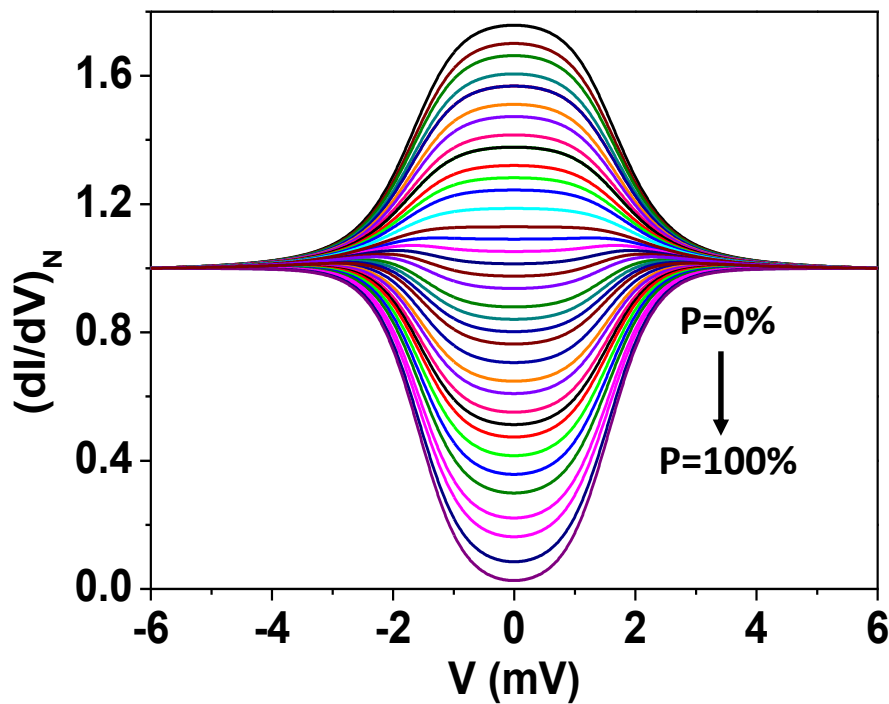
Figure 1.17: Simulated curves obtained from modified BTK model with spin-polarization. The value of P_t varies from 0 to 100 %

1.7.3 PCAR spectroscopy on TI – suppression of AR:

Now the idea is to measure the spin-polarization of a topological surface state. In this regard, we replace the ferromagnetic electrode with a TI (Figure 1.18). In a ferromagnetic metal spin, selective bands are present which suppress Andreev reflection whereas in TI the spin is in plane locked perpendicular to the momentum which causes a spin selective transport. In a superconductor, the Cooper pairs are combined with a spin-up and spin-down electrons. Now, in the directional point-contact geometry of TI/S, only the electrons with in-plane locked with the topological surface states are allowed to propagate. Due to this selection mechanism, the Andreev reflection will suppress [95]. The suppression of the Andreev reflection can be measured using the same approach discussed above. Therefore, it is possible to measure the spin-polarization of a TI using this simple technique. It is important to note
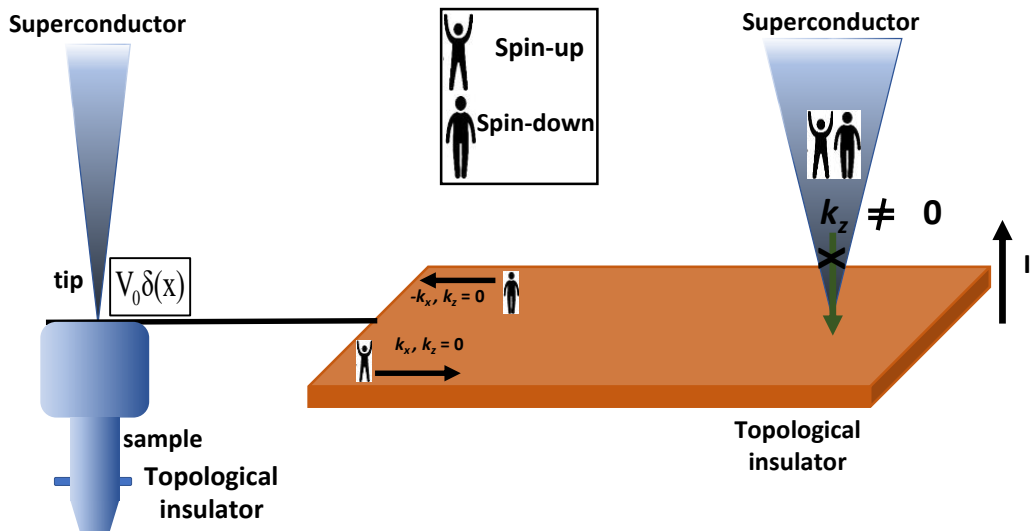
Figure 1.18: Suppression of Andreev reflection in a point-contact of topological insulator and a superconductor due to spin selective transport in TI.

that the measured spin-polarization in case of TI/S point-contact do not estimate upto 100 %. One should carefully notice that in a TI the spin current is 100% spin-polarized. However, here the spin is not a good quantum number because it does not commute with the Hamiltonian. Here the spin (S) is also associated with the orbital angular momentum (L). Total angular momentum $J = L + S$, commutes with the Hamiltonian. In the point-contact measurement we calculate the expectation value of J which gives $\sim 70\%$ for a strong TI [95, 130].

1.8 Point-contact spectroscopy in the thermal regime:

In the point-contact geometry, it is not possible to get ballistic limit contact always. When this happens, we should depend on the other hallmarks to detect superconductivity as well. There are two terms in Wexler's formula (equation 1.6). The first term is for ballistic limit resistance and the second term is Thermal limit resistance. From the second term, it is seen that the resistance is directly proportional to the resistivity of the sample. Now, if one of the electrodes between tip and sample is a superconductor, then in the thermal limit one should get a resistive transition with decreasing temperature. Another hallmark of a superconductor is the non-linear $I - V$ characteristic curve. A phase sensitive $I - V$ characteristic measurement also manifests the existence of superconductivity. The presence of critical current in a superconductor can be realized in an $I - V$ characteristic curve

which can be more easily resolved by taking the differentiation of the $I -$ V characteristic, gives dI/dV. The signature of the critical current dips about $V = 0$ in a $dI/dV\,vs.V$ spectra also a hallmark for the existence of a superconducting phase can be accumulated in the thermal limit of a point-contact [119]. A representative thermal limit spectrum is shown in Figure 1.13.

CHAPTER 2

Experimental details

In the previous chapter, I have mentioned some measurement techniques to study the topological systems and superconductors. In this chapter, I will introduce the measurement techniques in details which will be useful to understand the experimental results in the next chapters. First, I will introduce the STM technique.

Scanning tunnelling microscopy provides a direct evidence of quantum mechanical tunnelling. If the barrier width of the tunnel junction is 'd' then the expression for tunnelling current is,

$$I \propto e^{-2\kappa d} \tag{2.1}$$

The STM was invented by Gerd Binning and Heinrich Rohrer at IBM Zürich in 1981 [131], and they earned Nobel Prize in Physics in 1986. Using an STM one can achieve sub-atomic resolution. It has a high resolution because the tunnelling current decreases exponentially with distance which gives the high vertical resolution.
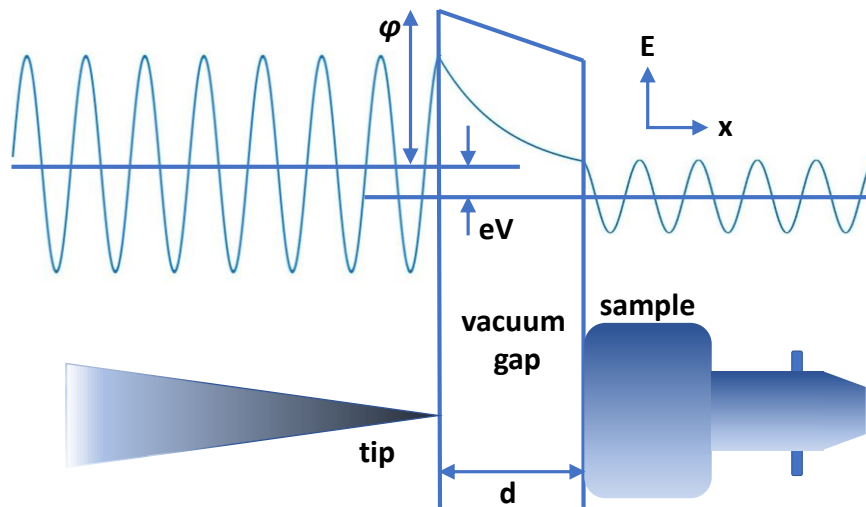
Figure 2.1: Schematic of a quantum mechanical tunnelling process.

2.1 Scanning technique in STM:

A typical STM consists of a metallic tip and a sample. The sample has to be either metallic or semiconducting because it involves tunnelling. A sharp tip is brought closer to the conducting sample upto several angstroms in order to reach the tunnelling regime. However, it is challenging to create such a small gap between the tip and sample. However, It is possible to reach in that length scale using a piezoelectric z-positioner, The procedure of approaching the sample is following,

1. Set a bias to the sample with respect to the tip (suppose 1 V)

2. Set a current value (suppose 100 pA)

3. Now connect an ammeter to measure the current

In this case, when the tip and sample are far enough, by applying a
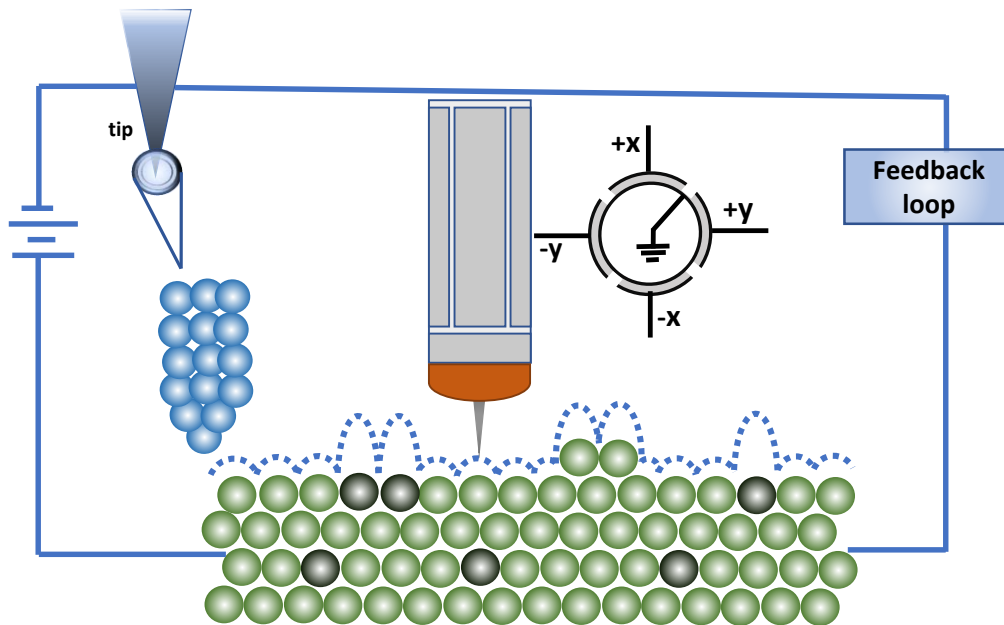
Figure 2.2: Scanning mechanism in a STM. A tube scanner with four major quadrants are shown. Bottom electrode is called Dither electrode.

voltage we will not get a current of 100 pA. In order to get the current, the tip (sample) need to walk close to the sample (tip). By applying a high voltage to a piezoelectric z-positioner which works in a slip-stick mechanism [132] one can make the tip approached to the sample. While approaching to the sample, we should measure the current as well. Now, the current amplifier is connected to a feedback loop to the positioner where it measures the current and keeps applying a voltage to the positioner until it reaches the set value of current. In a typical STM, xy-positioners are also attached to move around the sample. Once we reach in the tunnelling regime, we can scan over the sample using the tip which is embedded on a piezoelectric tube-scanner. The tube is generally divided into four quadrants vertically, and each of the opposite quadrants is connected to a voltage source shown in Figure 2.2.

Using a combination of applied voltages to the scanner one can bend the piezoelectric tube in any direction because of its intrinsic property. Now, one can also utilize this technique to scan over the sample in two ways. (i) Constant current mode, where the set value is a current and (ii) constant height mode, where the set value is a height between the tip and sample. It is possible to map the topography of the sample surface using both techniques. In the first case during scanning, the feedback loop will try to maintain the current constant by varying the height between the tip and sample according to the sample topography whereas in the second case it is opposite to the first one. Now, one can plot the change in height/current concerning the spatial points of the sample. From the color map of the plot, the topography can be seen. Now, if the sample surface is atomically flat and pristine and the end point of the tip contains on the atom, then one can also get the atomic resolution of the sample surface which includes the existence of impurities and defects.

2.2   Types of STM measurements:

At cryogenic temperature the tunnelling equation can be written as,

$$I_T \approx \beta \mid T \mid^2 \int_0^{eV} N_S(E)dE \qquad (2.2)$$

where, $N_S(E)$ is the density of state of the sample. Typically, PtIr or W tips used to use in the STM measurements and the density of states of tip is considered to be constant around the Fermi level. $|T|^2$ is the tunnelling

matrix can be expressed as,

$$|T|^2 \approx e^{-2\frac{d}{\hbar}\sqrt{2m\phi}} \tag{2.3}$$

where, ϕ is the work function and d is the tunnelling height.

From equation 2.2 it is clear that the tunnelling current measured at bias V is proportional to the integral of the density of states of the sample.

Topography: As I have mentioned earlier, the STM can map the topography of the sample surface. One can also observe the defect and impurity states on the surface. The tunnelling current depends on the sample barrier width and the density of states of the sample. The surface with a homogeneous density of state gives purely geometric surface topography whereas, the surface with a heterogeneous density of states give the geometric surface plus the charge density wave shown in Figure 2.3 (top left).

dI/dV spectrum: In addition to obtaining information about the surface topography, STM also can acquire LDOS up to several electron volts. Fixing the distance between the tip and sample by turning off the feedback loop, $dI/dV - V$ can be measured which gives the information about LDOS of occupied and unoccupied states with respect to the energy.

$$\frac{dI}{dV} \propto N_S(E)$$

A representative dI/dV spectrum is shown in Figure 2.3 (top right). The measurement details are described in the next section.

dI/dV mapping: As it is possible to measure the LDOS at a fixed point, it is also possible to measure the LDOS at every point within the scan area on the sample. By obtaining the LDOS data at every point on the surface,
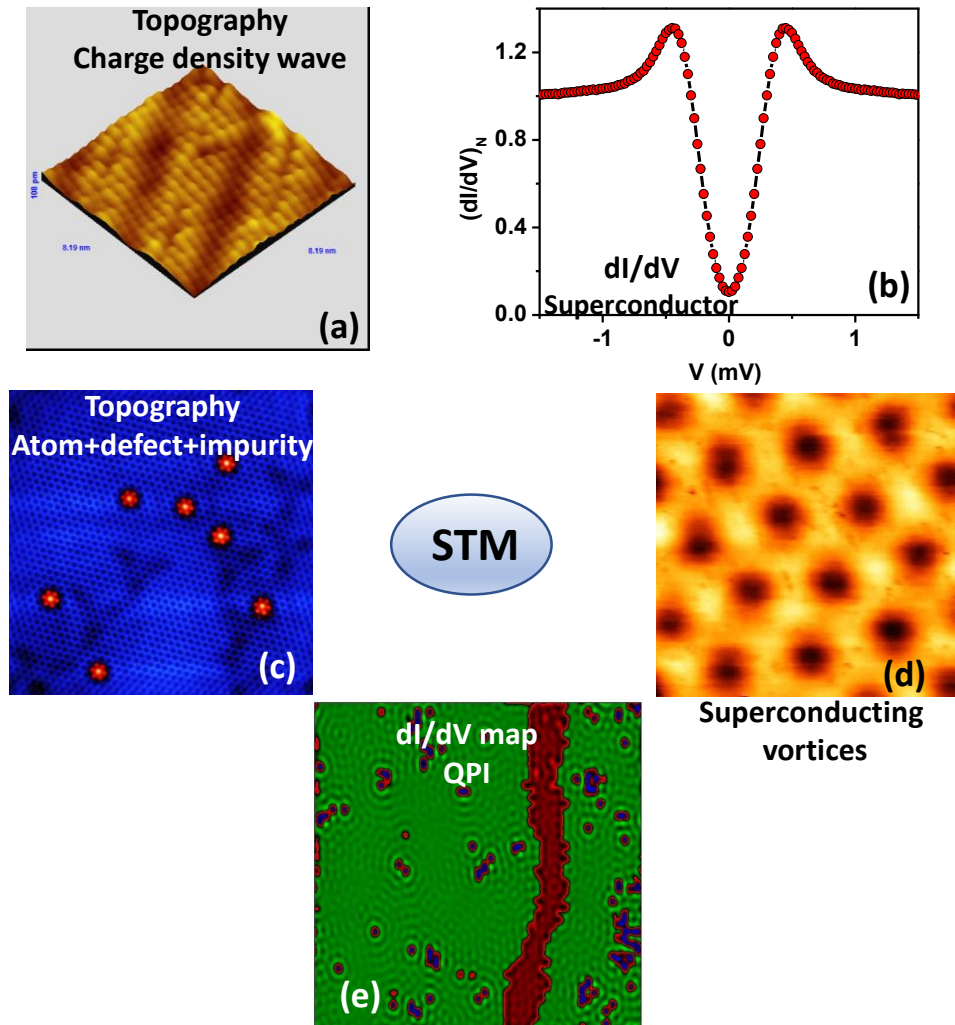
Figure 2.3: (a) Atomic resolution plus the charge density wave in BSCCO single crystal. (b) Superconducting $dI/dV - V$ spectrum of $PdTe_2$ (c) STM topography of Sb_2Se_3 Defects and and impurities are also seen. (d) Vortex imaging on $Co-NbSe_2$ (e) Quasipartical interference image extracted from dI/dV mapping in Sb_2Se_3.

one can slice the LDOS (dI/dV) at particular energy (bias). From this, we can map the LDOS on the real space directly. A quasiparticle interference pattern around the defects and boundary acquired in STM LDOS map is shown in Figure 2.3 (bottom right).

2.3   STM at IISER Mohali:

The STM was installed in August 2016, and I have actively participated in the installation process from scratch. The STM is built by UNISOKU (model 1300) equipped with a JANIS-He3 cryostat. The STM measurements can be operated at 300 mK in UHV (10^{-10} mbar) under an 11 T magnetic fields along the z-axis with 4G magnet controller. The whole system consists of a load lock chamber (LLC), a preparation chamber (PC), an exchange chamber (EC) and a STM chamber are arranged in this respective manner. All the chambers are separated by a VAT gate valve and are maintained in UHV at all times except the LLC.

2.3.1   Chambers:

The LLC chamber is utilized to expose to mount a new sample or tip inside. The small LLC is first pumped down to 10^{-8} mbar with an Edwards nEXT-300 turbo molecular pump (TMP) before opening the gate valve between LLC and PC.

In the PC, it is possible to clean, prepare and characterize a sample and tip. The PC consists of a tip heating system, two thermal evaporators (K-shell and W-shell) with low-temperature surface treatment facility on a sample, one Argon reverse sputtering system, reflected high energy electron diffraction (RHEED), low energy electron diffraction (LEED), and an auger electron spectroscopy (AUS).

The EC consists of a low-temperature cleaving facility and a long UHV
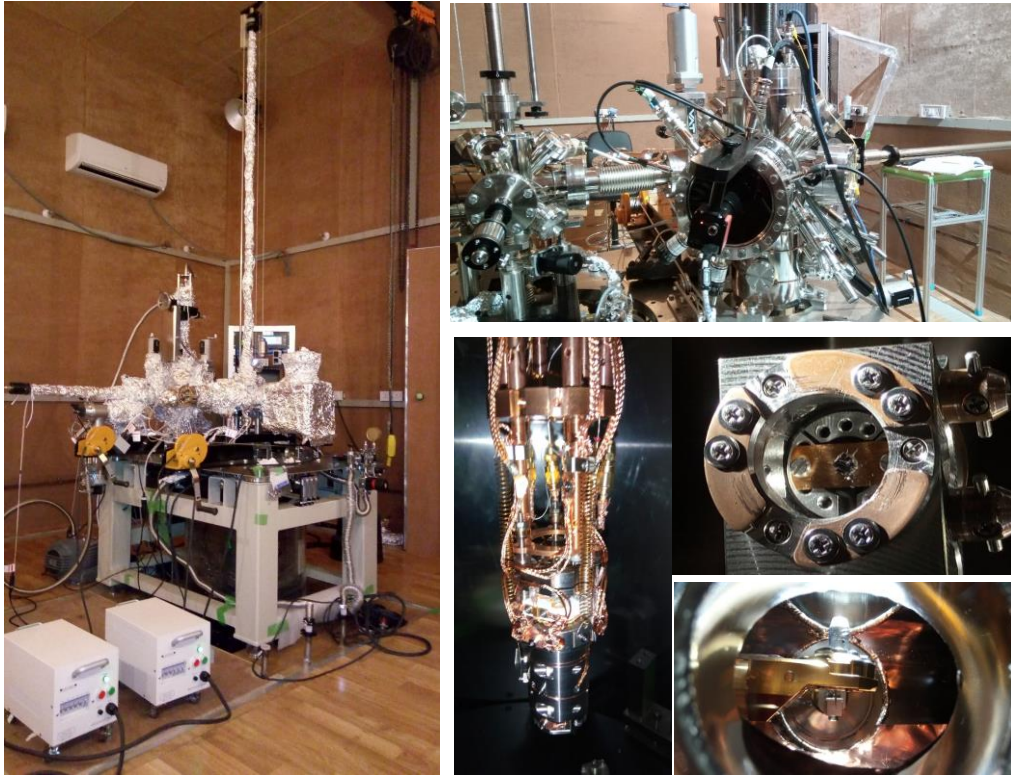
Figure 2.4: Some images of the STM at IISER Mohali.

manipulator to transfer the sample and tip holder in the STM chamber. All the chambers are also equipped with UHV magnetic manipulators to transfer the tip and sample from one chamber to another chamber.

2.3.2 Noise isolation:

In order to get an atomic resolution image, one must be very careful to isolate the vibrational, electromagnetic, and acoustic noise from the scanning space. At IISER Mohali the STM system was installed in a separate building with a customized building structure. In order to avoid the vibrational noise, we made a giant cubic concrete pit that is isolated from the rest of the building

Figure 2.5: Inside picture of active vibration isolation.

in all the 6-faces, on which the STM system stands. As the cryostat has a high field magnet, we have chosen all the components nonmagnetic. The rods for the concrete block were made of aluminium (1 inch diameter) (Figure 2.5). To isolate the electromagnetic and acoustic noise, we made a Faraday cage embedded with acoustic isolation. In order to avoid the ground loop noise, we made separate grounding pits for the measurement electronics with a ground line resistance of < 2 Ω.

2.4 Tip preparation:

A large probability to get an atomic resolution image depends on the tip apex. Therefore, it is essential to make a good tip in order to increase this probability. The most used tip material in STM systems is Tungsten (W) because it is easily etchable and the DOS is flat near the Fermi energy.
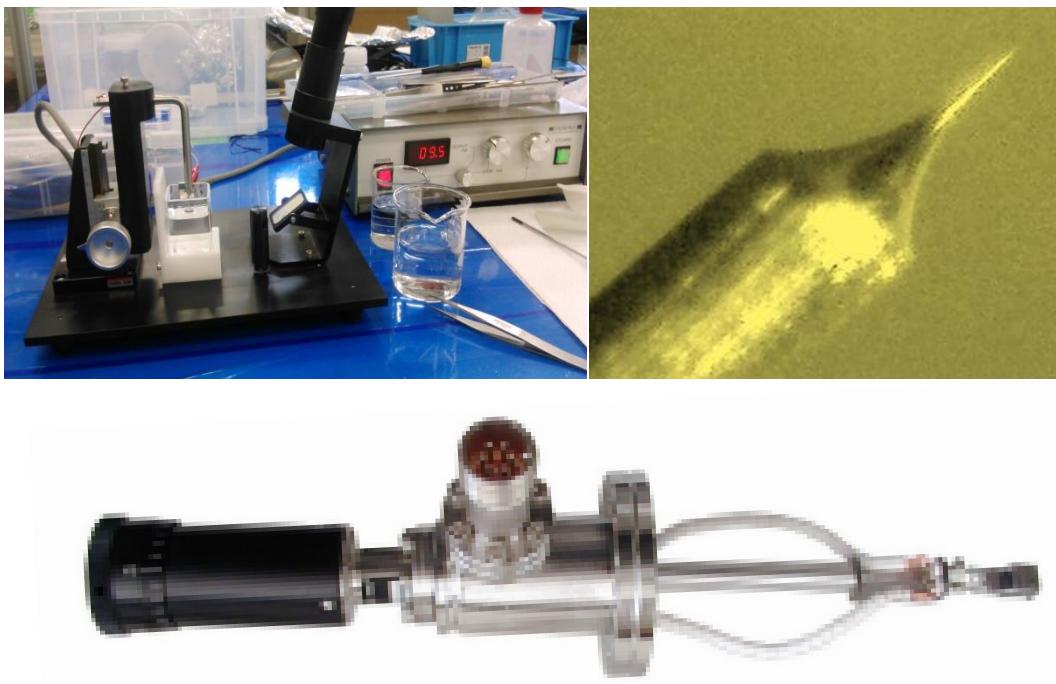
Figure 2.6: (top left) Tip preparation setup, (top right) A processed tip image, (bottom) UHV tip heat treatment setup.

The process for making W tip is electrochemical etching. The solution used for this mechanism is NaOH/KOH. There are two electrodes, one should be connected to the tip (W) wire, and another one should be the solution. If the wire is inserted into the solution and apply a voltage between the wire and solution, then electrochemical etching will begin very slowly. In order

to increase the electric field, a ring-type arrangement is made to around the wire on the top surface of the solution. The etching probability will increase and the material will etch faster from the surface around the ring. In order to control the mechanism automatically a current feedback circuit with a circuit breaker is attached to the system. Once it reaches the calibrated set current value the circuit breaks and control over the etching. As a general procedure, first, make 1.2 N NaOH or KOH solution and keep ready ethanol and distilled water in two separate beakers. Then, 0.5/1.0 mm diameter W wire cut into many pieces and scratch those with a P8000 grade sandpaper to remove the oxide layers roughly. Now clean the W wire with ethanol and fix it in one of the electrodes. Then apply bias (say 10 V) and set a current (say 1 mA). Once the etching finishes an alarm sound is to alert and the tip is dipped immediately in distilled water for 30 seconds then it is dipped in ethanol to avoid formation of oxide layer on the freshly etched tip. After confirming the that the tip has a sharp apex with an optical microscope, it is transferred in the UHV chamber after mounting on tip holder. Here, we have another tip heating treatment facility to remove any oxide layer and modify the tip apex.

Figure 2.7: (top) Sample holders, (bottom left) image of the UHV cleaver, (bottom right) A tip holder

2.5 LEED:

There are several techniques to characterize the surface of a single crystal. Low energy electron diffraction (LEED) is one of such techniques. A low energy electron gun is used to generate an electron beam. The focused electron beam emerges normally on the surface of a single crystal. If the sample surface is pristine, then a diffraction pattern will form, and that can be detected by a detector placed behind the source. The sample must be grounded properly during measurement otherwise, no diffraction pattern is obtained even if the sample is clean.The electron beam falls on the surface and makes it charged. If the sample is not grounded the charge will remain there and further reflect the electron beam by the repulsion between the beam and the

charged surface. The grounded sample transfer the charges to the ground and make the electron beam fall on the surface.

2.6 STM measurements:

All the STM measurements were performed in UNISOKU-1300 system. Though we have isolated the STM chamber from the unusual noises as mentioned earlier, it is important to reduce the electrical noise as well. To do this one needs good electronics. Our STM is interfaced with a R9 controller from RHK technology. Inside the R9 controller four lock-in amplifier (0-100 kHz), several voltage sources (-10 V to 10 V), high/low pass filters, two PLLs, twenty DACs, four digital oscillators, spectrum analyzers are assembled. The R9 controller can be interfaced with IHDL icon-based program language.

In a typical STM technique, we apply voltage and measure current. However, measuring voltage is much more easier than current. In this regard, we use a Femto DLPCA-200 current amplifier (gain from 10^3 to 10^{11} V/A, Input noise down to 4.3 fA/$\sqrt{}$Hz) which first converts the current to voltage and then amplifies it – this also reduces noise in the feedback signal. In addition to this, we also use a high voltage filter provided by UNISOKU to reduce the high-frequency noise to the input signal. The cut-off frequency of the filter is 530 kHz. A second stage voltage pre-amplifier (R9 IVP preamp) is also used to the input signal. The approach mechanism is controlled using PMC100 from RHK technology which is interlocked with the R9 controller in order to control the approach mechanism automatically by the interface program. In order to increase the S/N ration, we use several filters before all of the input

lines such as temperature controller, piezo motor controller, etc.

With these cautions, one can perform real space imaging easily because we have taken care of the input voltage and output feedback current signal. Higher resolution is required for measuring $dI/dV - V$ spectroscopy. Apparently, it seems that it is nothing but a derivative of an $I - V$ characteristic curve. However, it is beyond that. A simple voltage or current source or a multimeter do not care about the phase of the signal. As the tip and the sample in the STM geometry do not touch each other, it will work as a capacitor, and for AC signal one must care about the phase of the input and output signal. To do this, we must need a lock-in amplifier.

It is simple to control the signal locked at first harmonic is proportional to dI/dV : the output can be expressed by Taylor expansion,

$I(V = V_{dc} + V_{ac}cos\omega t$ with $V_{dc} \gg V_{ac}) = I(V_{dc}) + \left(\frac{dI}{dV}\right) \mid_{V_{dc}} V_{ac}cos\omega t + \frac{1}{2}\left(\frac{d^2I}{dV^2}\right) \mid_{V_{dc}} (V_{ac}cos\omega t)^2 + \cdots = I(V_{dc}) + \left(\frac{dI}{dV}\right) \mid_{V_{dc}} V_{ac}cos\omega t + \cdots$

One can measure the first harmonic with a lock-in amplifier which is phase sensitive without losing any information. The applied V_{ac} is very small compared to the V_{dc} ($< 5\%$)

The resolution of the R9 controller is 24 bit. During the spectroscopic measurement on a low-temperature superconductor, the applied voltage step should be less than the superconducting energy gap. The bit size of the controller is fixed. Therefore, in order to get a better resolution, we use voltage divider down to 1/100 during spectroscopy at low bias.

To do the LDOS map we choose image + spectroscopy option where the tip does spectroscopy and imaging both but one at a time. During spectroscopy, the feedback remain turned off, and it is on during imaging.

Figure 2.8: Some Electronics of STM measurements

The selection of the pixel size and sampling time defines the required time for a LDOS map in a given area. However, it is also possible to do LDOS map at certain energy by adding a low AC signal to the tip-sample bias voltage and do imaging only that requires much less time. In this case, It important to note that in this process the feedback is remains turned on. Therefore, any signal which is comparable to the topographic signal can not be resolved.

2.7 Point-contact spectroscopy:

Point-contact spectroscopy is a very powerful technique to study the behaviour of a electron in metals [113, 133], ferromagnets [125–128], superconductors [134–138], topological insulators [95] etc. There are several methods to do point-contact spectroscopy. Here I will discuss the needle-anvil method. In this method, a sharp tip physically touches the sample.

2.8 The point-contact probe:

A point-contact probe consists of a sample space, a tip holder and an approach mechanism. This probe is designed to be used in an American magnetics cryostat operated at 1.4 K with a vector magnet of 6-1-1 T. In this probe, we have used a differential screw (100 threads per inch) which can be operated from the top using a manipulator. The whole probe goes inside the liquid helium dewar. In order to measure the temperature of the sample space we use a calibrated Cernox thermometer and to heat this space, we use a 50 Ω Nichrome coil heater.

As it is operated at helium temperature, one should block the radiation from the outside. In order to block the radiation, we use multiple copper radiation baffles on the probe connectors at the top are vacuum sealed and 0.25 mm copper wires are used for the connections from the top to the sample space. The sample connections are made by 50 micron gold wires from Alfa Aesar using a silver epoxy as a conductive glue.
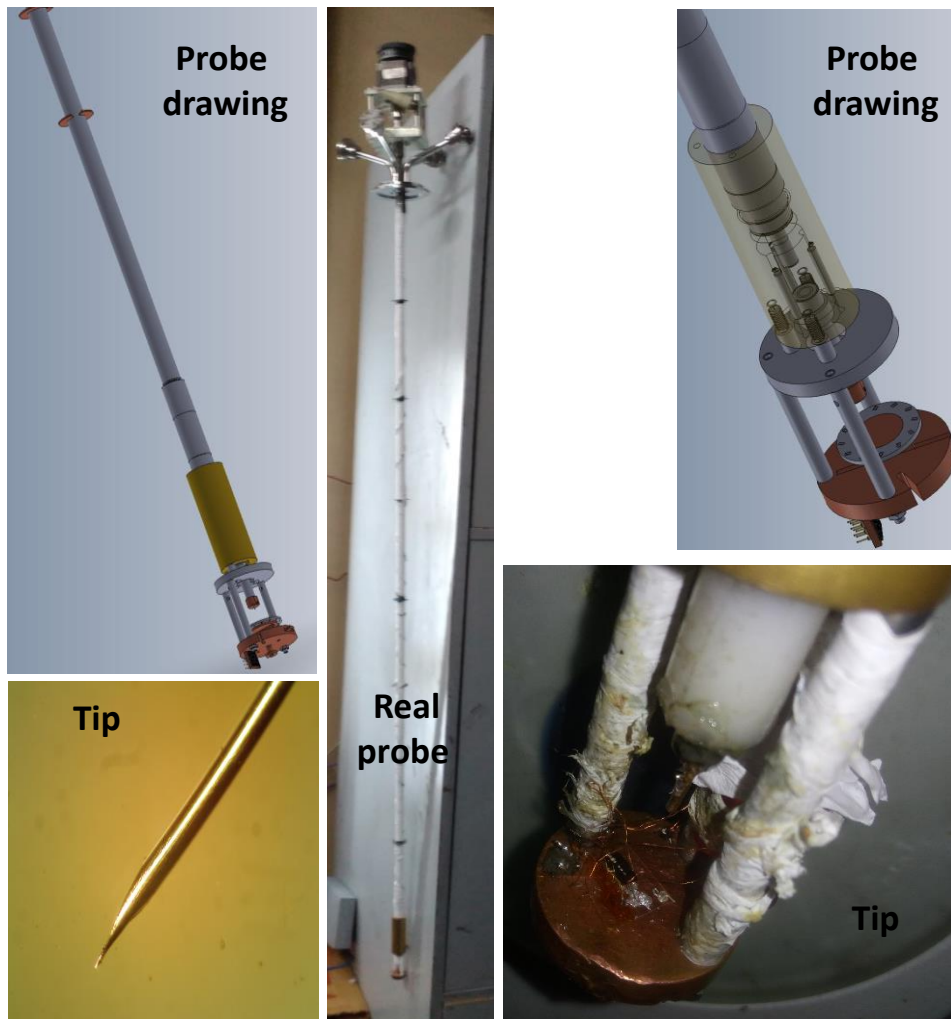
Figure 2.9: Point-contact probe: Drawing and real

2.9 Data acquisition:

Lock-in based modulation technique is used to obtain the PC spectrum. A sweeping dc current I_{dc} coupled with a small, fixed amplitude ac current $I_{ac}cos\omega t$ from Keithley 6221 (ac+dc current source) is passed through the point contact.
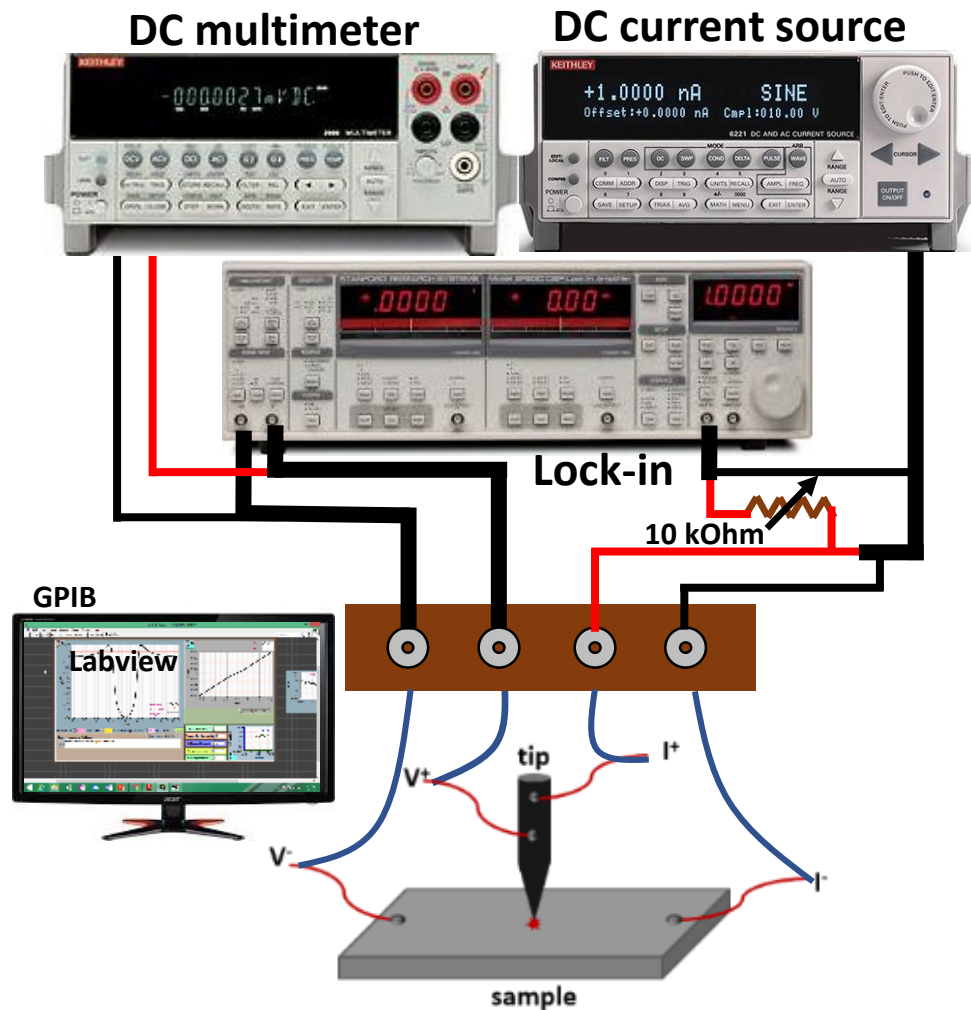
Figure 2.10: Data acquisition setup of point-contact spectroscopy measurement.

The dc output voltage across the point contact V, is recorded by a digital multimeter (Keithley 2000) while the differential resistance dV/dI (proportional to the ac output voltage locked externally at the first harmonic) is measured by a lock-in amplifier (SR830). It is simple to show why the signal locked at first harmonic is proportional to dV/dI (and second harmonic to d^2V/dI^2): the output voltage can be expressed by Taylor expansion,

$V(I = I_{dc} + I_{ac}cos\omega t$ with $I_{dc} \gg I_{ac}) = V(I_{dc}) + \left(\frac{dV}{dI}\right) |_{I_{dc}} I_{ac}cos\omega t +$ $\frac{1}{2}\left(\frac{d^2V}{dI^2}\right) |_{I_{dc}} (I_{ac}cos\omega t)^2 + \cdots = V(I_{dc}) + \left(\frac{dV}{dI}\right) |_{I_{dc}} I_{ac}cos\omega t + \frac{1}{4}\left(\frac{d^2V}{dI^2}\right) |_{I_{dc}}$ $(I_{ac})^2(1 + cos2\omega t) + \cdots$ One may use a voltage-to-current converter with an adder circuit to couple dc voltage (from a source meter or from auxiliary port of SR830) and ac voltage (from SR830 with locked internally or from a function generator locked externally) as well. The schematic of this technique is shown in Figure 2.10. The data acquisition is performed through GPIB connection and the measurement is made completely automated (using LabVIEW platform) with full control over the measurement parameters like temperature, magnetic field *etc.*

CHAPTER 3

Conventional Superconductivity in PdTe$_2$

Investigation of Majorana Fermion is at the forefront of the experimental Condensed Matter Physics due to the ubiquitous property of it being its own antiparticle [153]. Discovering such a particle experimentally, is one of the breakthroughs in science. Different techniques are being followed world wide to probe Majorana Fermions [100, 101, 104, 139–154]. The most attempted technique to detect Majorana fermions experimentally is by making heterostructures of topological insulators and superconductors. The idea of making heterostructure came in mind because it is believed that Majorana fermions can be found in a material which displays topological superconductivity [93]. Therefore, it is an obvious choice that superconductivity realized on a topologically nontrivial material may give a way to find the relativistic Majorana fermion. There are many experiments claim to detect the signature of Majorana fermions in their systems, but the actual finding is still elusive. Other than heterostructure, people have also tried to find this particle by applying pressure [155–161], doping a topological material [162–165], induc-

ing superconductivity by the normal tip on a topological materials [166–169]. But the realization of this particle still under debate in the community. Now, one might also think that if it is possible to realize superconductivity on a parent material whose normal states is topologically nontrivial. The first such type of discovered materials is PdTe$_2$. Though the superconductivity in PdTe$_2$ is already known since 1961 [170], the topological nontrivial behavior of this material is realized in 2017 [71]. Soon after the discovery of topological nature of PdTe2, it has drawn more attention in the search for topological superconductivity in this material. As the normal state of the material is type II Dirac semimetal, it is a natural choice to investigate the superconductivity thoroughly. All the previous reports of such investigation on PdTe2 based only on bulk transport measurement. In order to study the superconductivity more precisely for the first time we performed STM/S measurements on a single crystal of PdTe$_2$.

3.1 Synthesis and characterization of the PdTe$_2$ single crystals:

High-quality single crystals of PdTe2 were grown using a melt-grown method by taking Pd (99.99 %) and Te(99.999 %) as starting elements. The detailed crystal growth technique is described in Ref. [171]. The purity of the crystal initially confirmed by powder x-ray diffraction pattern. The single crystals of PdTe2 were well crystallized in CdI2-type structure with the $P\bar{3}m1(164)$ space group. The grown single crystals were easily cleavable had quite high

residual resistive ratio (RRR), $\rho(300K)/\rho(2K) \backsim 75$. The single crystals also displayed de Haas-van Alphen (dHvA) quantum oscillation in a relatively how magnetic field (B) of 3 T at $B \perp c$, where c is the crystal axis perpendicular to the cleavage plane [171]. The Landau level index (n) vs. $1/B$ curve gave a non-zero intercept of 0.42 which confirmed the existence of a nontrivial topological band [171]. These experiments confirmed the quality and topological behaviour of the single crystal.

3.2 Surface characterization of the PdTe$_2$ single crystals:

Till now the quality of the crystal was confirmed by bulk measurements. But, STM is a surface sensitive measurement. Therefore, it requires an extremely clean surface. In order to achieve this, the single crystal was cleaved in UHV by an $in-situ$ cleaver at liquid nitrogen temperature to get a pristine crystal surface. In order to confirm the surface quality of the crystal first, we performed LEED measurement on PdTe$_2$. The LEED pattern of PdTe$_2$ single crystal is shown in Figure 3.1 (a). The Laue diffraction pattern is clearly visible in that image. Now we transferred the crystal into the STM head using an UHV manipulator for scanning measurements. The atomic resolution image of the surface if PdTe$_2$ is shown in Figure 3.1 (b). The atomic arrays show a hexagonal closed pack (hcp) arrangements of the surface.

The interatomic distance is 4.0 ± 0.1 Å. In the atomic resolution image
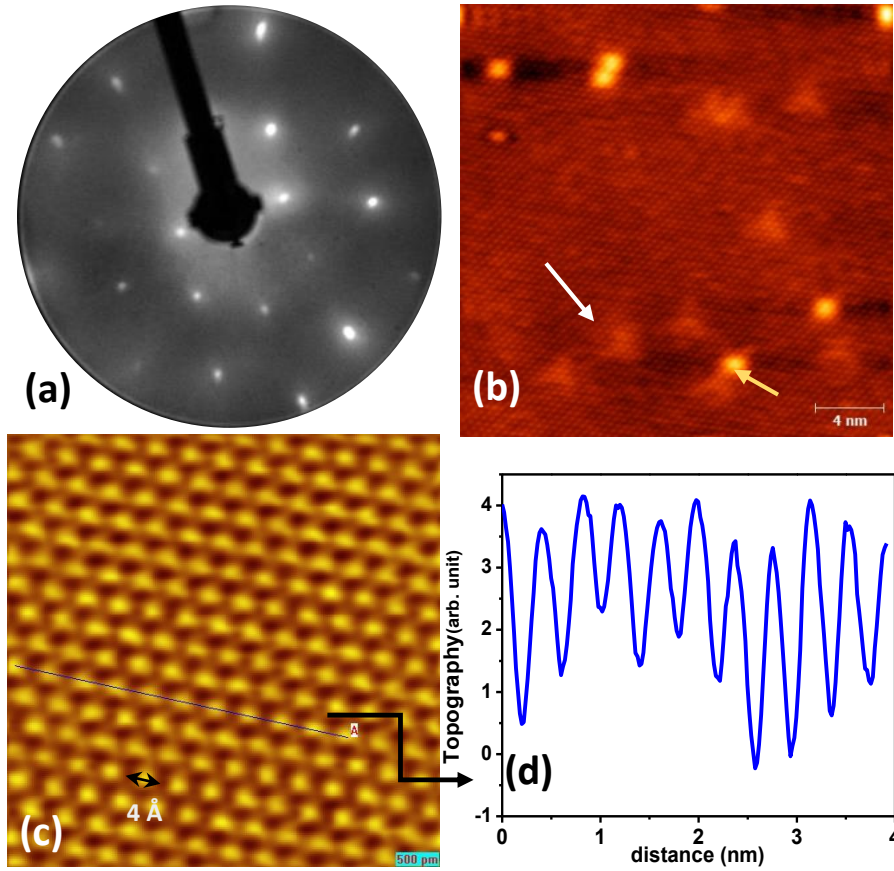
Figure 3.1: (a) LEED pattern of the cleaved surface of PdTe$_2$ single crystal. (b) Atomic resolution image of PdTe$_2$ captured at 2.6 K. The measurement parameters are, $V_s = 300$ mV and $I_s = 380$ pA, 512 px $\times$ 512 px, 25 $\times$ 25 nm^2 . Two types of defects are indicated by the white and the yellow arrows respectively. (c) Atomic resolution image in a defect free area. (d) A topographic modulation across the line on the image in (c).

two types of defects are clearly visible, (i) clover-leaf shaped defects (marked by white arrow) and (ii) additional atoms abbreviated as adatoms. The clover-leaf shaped defects are formed due to the Tellurium (Te) vacancies from the atomic lattice sides. This type of defects also seen on the surface of topological insulators such as Bi$_2$Se$_3$, Bi$_2$Te$_3$, etc. [47, 49, 50] A zoomed in view of a defect free area is also shown in Figure 3.1 (c). A topographic

modulation of the line cut in Figure 3.1 (d) is also shown in Figure 3.1 (b). From this surface sensitive measurement, we finally confirmed the pristine surface quality of the crystal. In order to look at the local density of states (LDOS) of the material, we need to do the energy resolved scanning tunnelling spectroscopy (STS).

3.3 Spectroscopy on the PdTe$_2$ single crystals:

First we performed STS measurements at 22 K which is above the superconducting transition temperature ($\sim$ 1.7 K). A $\frac{dI}{dV}$ vs V spectrum on PdTe$_2$ at 22 K is shown in Figure 3.2 (a).
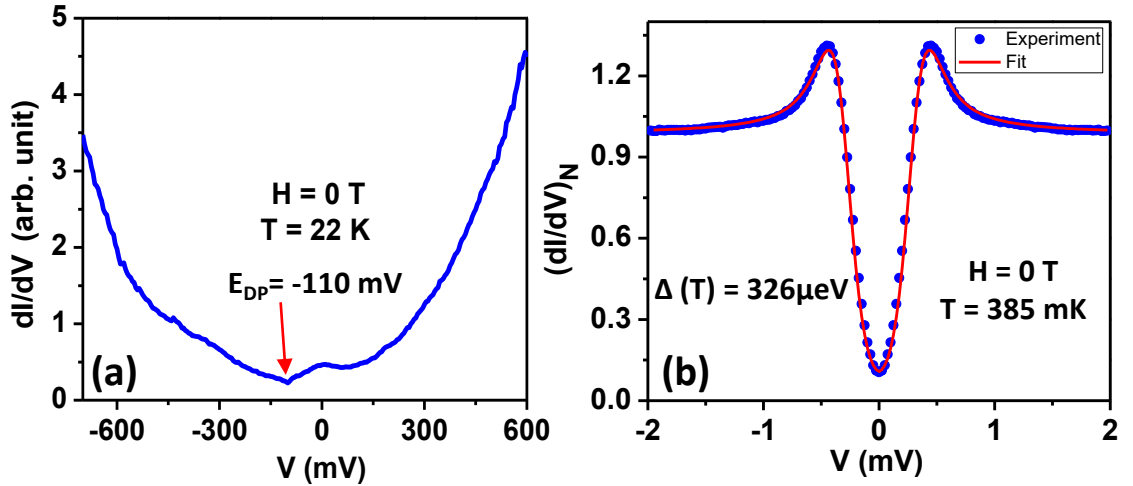
Figure 3.2: (a) A differential conductance spectrum measured by STS at 22 K where $V_s = 300$ mV, $I_s = 800$ pA, $V_{mod} = 5$ mV, and f$_{mod} = 783$ Hz (b) Normalized STS data taken at 385 mK. $V_s = 2$ mV, $I_s = 1.73$ nA, V$_{mod} = 100$ μV and f$_{mod} = 881$ Hz. The scattered curve shows experimental data points and the red line shows theoretical fits within BCS theory.

We spanned the energy range from -600 meV to +600 meV. A "*V*" shaped spectral feature corresponds to a Dirac cone, and in our case, it appeared at 110 meV in the valance band. The concentration of defect state defines the position of the Dirac cone. Here $\frac{dI}{dV}$ is proportional to the local density of the surface states. From this observation, we further confirmed that the surface states of the crystal we are measuring is topologically nontrivial as it was reported a type II Dirac semimetal. After confirming the crystal quality and topological behaviour, we investigate the superconductivity of the sample at low temperature. By lowering down the sample temperature below the critical temperature, we performed similar spectroscopy but in lower energy range. In order to get higher resolution in the low energy spectroscopic data we use a voltage divider to step down the voltage ranges. A superconducting spectrum at 385 mK spanned over an energy range -2 meV to 2 meV is shown in Figure 3.2 (b). The peaks about $V = 0$ is called coherence peaks related to the superconducting energy gap apparently. The LDOS is essentially zero at zero bias. We tried to fit the superconducting spectrum using the Dyne's formula (Equation 1.22). The superconducting spectrum is well fitted with the simulated curve which lies within the BCS theory. The superconducting energy gap measured from the fitted parameter is 326 μeV at 385 mK.

3.4 Nature of superconductivity:

As the normal state of the material is topologically nontrivial, the coexisting superconductivity is expected to be unconventional in nature. But the above superconducting spectrum is fitted with BCS theory seems to be the

superconductivity is conventional in nature. Now one can argue that if it is a conventional superconductor then why not the LDOS is zero at zero bias? In order to find the answer let's go back to the BCS theory. As the superconductivity described in the BCS theory is at $T = 0$, but our measurements were done in a nonzero finite temperature. There should be one parameter to control the temperature effect of the spectrum. In Dyne's formula, Γ described as a quasiparticle lifetime which is related to the electron temperature of the tunnel junction. Now, in this case, the superconducting transition temperature is 1.7 K, and we measure the superconductivity at 385 mK which is not even five times lesser than that of the transition temperature. Thus the spectral feature is not falling to zero at zero bias. In order to investigate the actual nature of the superconducting property, we need to do further experiments such as temperature and magnetic field dependence of the spectrum.

3.4.1 Temperature and Magnetic field dependence of the spectrum:

The superconductivity evolves with temperature and magnetic field. Here we performed the temperature dependence of the spectrum at zero magnetic fields and without changing the position of the tip (Figure 3.3 (a)). However, variation of temperature comes with the cost of thermal drift of the STM tip with respect to the sample which is negligible in this case because the change in temperature is minimal. The superconducting spectral feature evolves gradually and vanishes at 1.78 K which is the bulk T_c of the sample.

All the spectrum were fitted with Dyne's formula at different temperature values. The measured superconducting energy gap as a function of temperature is plotted in Figure 3.3 (b). The gap decreases systematically with temperature and lies on the BCS predicted Δ vs T curve which confirms the superconductivity is conventional in nature. The formula used for the fitting curve is,

$$\frac{\Delta(T)}{\Delta(0)} \approx tanh\left(1.74\sqrt{\frac{T_c}{T} - 1}\right) \tag{3.1}$$

We also performed magnetic field dependence of the spectrum at 385 mK. The spectral feature decreases gradually with increasing magnetic field and vanishes at 1.6 T (Figure 3.3 (c)). We tried to fit the spectrum at different magnetic fields by changing the broadening parameter Γ. The measured superconducting energy gap as a function of the magnetic field is plotted in Figure 3.3 (d). The experimental data lies on the empirically predicted $H - T$ phase diagram for a conventional superconductor. The formula used for the fitting curve is,

$$H_c(T) = H_c(0)[1 - (T/T_c)^2] \tag{3.2}$$

The $H - T$ further confirmed the superconductivity in type II Dirac semimetal PdTe$_2$ is conventional in nature. The parameter $\frac{2\Delta}{k_B T_c} \sim 4$ gives rise close to weak coupling BCS superconductor, and the calculated coherence length is around 14 nm.
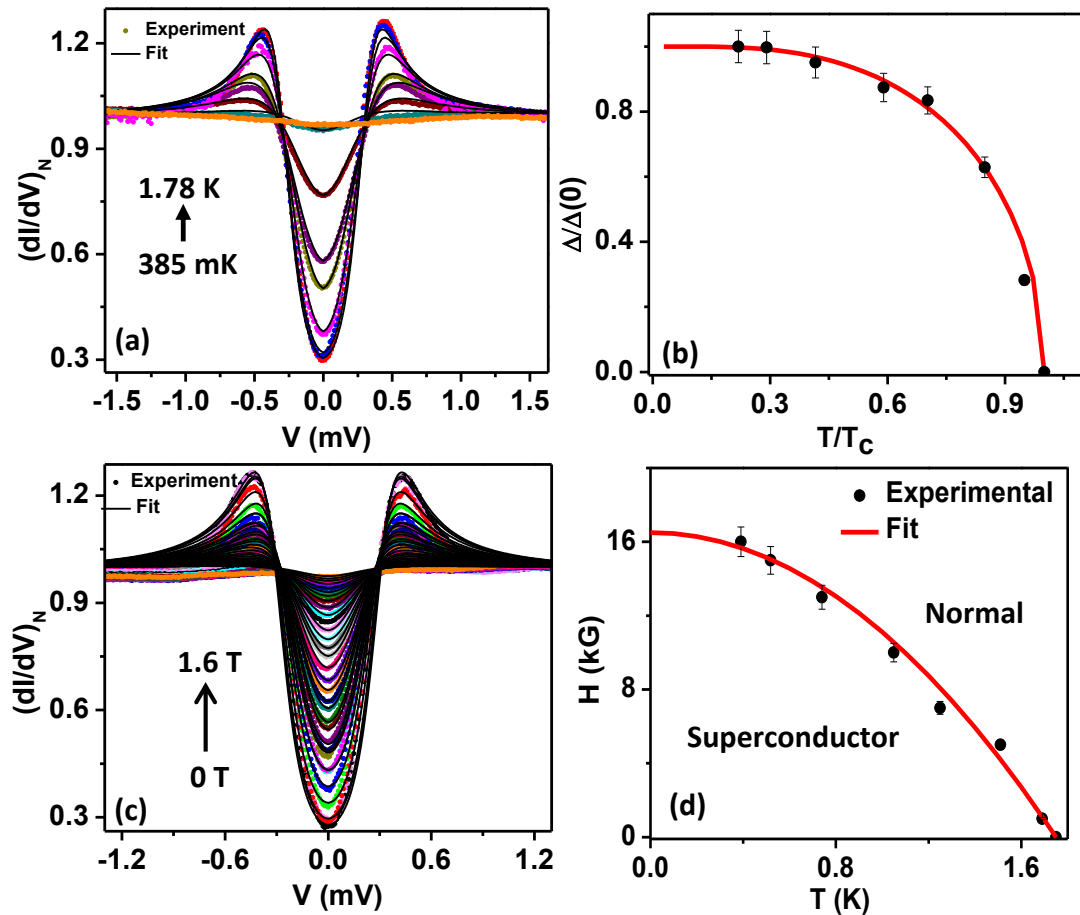
Figure 3.3: (a) Normalized STS data with varying temperature over a range from 385 mK to 1.78 K. The colored lines show experimental data points and the black lines show theoretical fits within BCS theory. (b) Temperature evolution of Δ. The dots are values extracted from the theoretical fits and the solid line shows the temperature dependence as per BCS theory. (c) Normalized STS data with varying magnetic field ($\parallel$ c axis) up to 1.6 T. The colored lines show experimental data points and the black lines show theoretical fits within BCS theory. (d) The H-T phase diagram extracted from the temperature dependent STS measurements at different magnetic fields. The solid line is a plot of the phase line expected empirically for conventional superconductors.

3.5 Conclusions:

In conclusion, from our detailed tunnelling spectroscopic study, we have shown that the superconductivity in type-II Dirac semimetal $PdTe_2$ is conventional in nature. From the dHvA oscillation measurements, it is seen that with H⊥c gives rise to one band topologically nontrivial, but with H∥c, there are other bands available which could be trivial and lead to conventional superconductivity in case of $PdTe_2$ [171]. In order to understand the unexpected behaviour of the superconductivity, detailed theoretical investigation required.

3.6 Appendix:

3.6.1 Observation of inhomogeneous superconductivity in $PdTe_2$

The magnetic field dependence of the superconducting spectrum shows that the superconductivity in $PdTe_2$ vanishes at 1.6 T which is quite high. But in previous reports, it is claimed that $PdTe_2$ is a type-I superconductor which is quite strange. As $PdTe_2$ is a binary compound, it should be a type-II superconductor. Our further investigation interestingly revealed that the critical field is spatially inhomogeneous (Figure 3.4 (a),(b)). We plotted a statistical average is shown in Figure 3.4 (c). The superconductivity with low critical field dominates which is in accordance with the bulk transport measurements. But STM is a local probe measurement which gives that the

number of spectra with the low critical field is quite high however the critical field spans over a large scale upto 4 T which may point towards the existence of a mixture of type-I and type-II superconductivity in PdTe$_2$ [173].
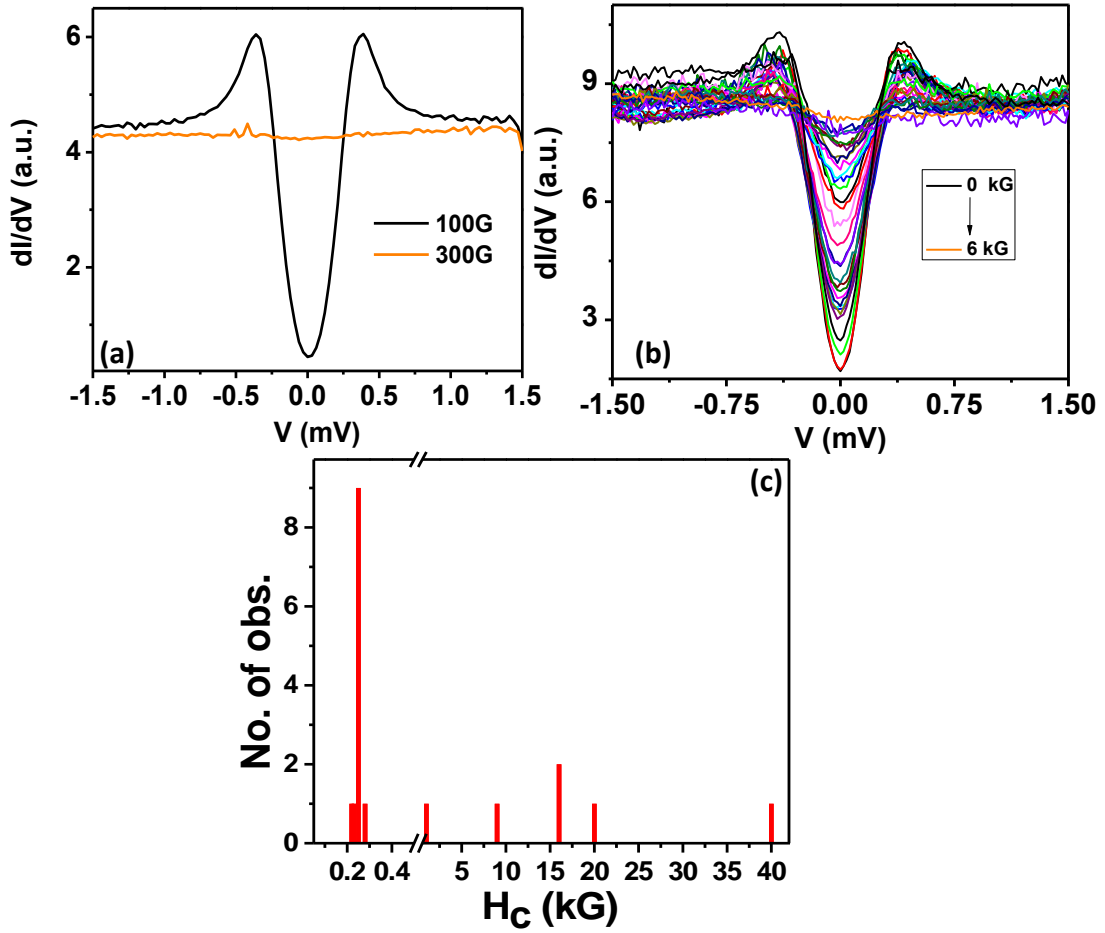
Figure 3.4: (a) Superconducting spectrum with a low critical field. (b) Superconducting spectrum with a high critical field. (c) Statistical average of measurement of H$_c$

CHAPTER 4

High spin-polarization in Sb_2Se_3

According to the band theory in solid state physics, metals and insulators are distinguished by a band gap. Topological insulators are the new state of quantum matter incorporated with the time reversal symmetry protected conducting surface states whereas the bulk is insulating [32]. In a topological insulator, the spins of the surface states are in-plane locked perpendicular to the momentum and this phenomenon abbreviated as "spin-momentum locking" [30]. The spin-orbit coupling in such systems plays a vital role to create an effective magnetic field. In order to obtain high spin-orbit coupling in the materials, we should choose elements from the periodic table with higher mass numbers.

Most of the A_2B_3-type chalcogenide materials such as Bi_2Se_3, Bi_2Te_3, Sb_2Te_3 are topological insulators. But in spite of sitting in the same group Sb_2Se_3 is not known to be a topological insulator under ambient conditions. The elements of those materials are mostly heavy materials. Se and Te are chalcogenides with mass numbers of 78.96 and 127.68 respectively. The

mass numbers of Bi and Sb are 208.98 and 121.76 respectively. As mentioned above, three types of combination of those materials exhibit intrinsic topological property under ambient conditions. But Sb_2Se_3 whereas the mass numbers of both the elements are relatively small, is an exception here. From earlier band structure calculation and experiment it was classified that Sb_2Se_3 a member of A_2B_3-type chalcogenide family, a band insulator with high spin-orbit coupling. But some experiments argued that it is possible to emerge topological phase in Sb_2Se_3 under a high pressure of several gigapascals (GPas) due to the structural phase transition of the material under a high pressure [174–177]. But there are some results which are still controversial. Recently, a band structure calculation showed that Sb_2Se_3 can be a topological insulator under ambient conditions if we consider interlayer van der Walls interactions into the calculation. However, there is no experimental verification for this claim. As mentioned above that due to the high spin-orbit coupling, the surface states of a topological insulator are spin-polarized. The spin polarization of the surface states can be measured by Spin-ARPES which is the only experimental tool that can directly probe the spin-resolved bandstructure of materials [178–180]. The other indirect techniques have also been employed such as by controlling topological insulator photocurrents with light polarization, [181–183]. By comparing spin potentiometric measurements on topological insulator based devices [184,185]. We can measure the spin polarization of the surface states indirectly, using the spin-polarized point-contact Andreev reflection spectroscopy. The methodological details are described in Section 1.7. This technique was most widely exploited to measure spin polarization in ferromagnetic materials [125–128].

Recently, This similar technique is also employed (please see Section 1.7.3) to measure the spin polarization in several topological insulators [95, 186].
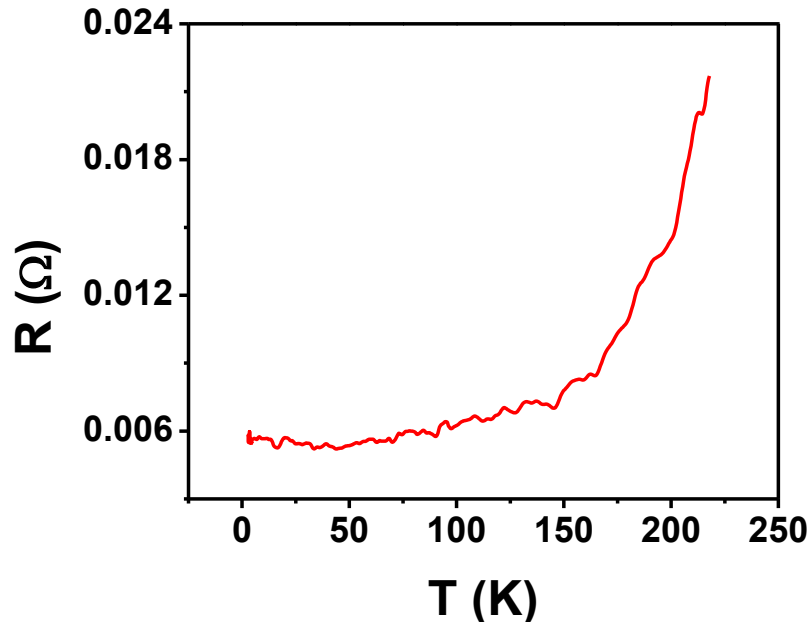
Figure 4.1: $R - T$ curve of Sb$_2$Se$_3$ in four probe geometry

It was known from the previous studies that Sb$_2$Se$_3$ is a band insulator, but our four probe resistivity (see Figure 4.1) measurement revealed that there are conducting state(s) in this material. To investigate further we started working on this material. Here, using spin-polarized point-contact Andreev reflection spectroscopy and scanning tunnelling microscopy/spectroscopy, we studied the surface states of Sb$_2$Se$_3$.

4.1 STM on Sb_2Se_3:

First, we confirmed the surface quality of the crystal. The single crystals of Sb_2Se_3 were cleaved at low temperature (80 K) inside a UHV chamber using an $in-situ$ cleaver and immediately transferred into the STM chamber with an UHV manipulator. We performed STM scanning in constant current mode. The atomic terraces are shown in Figure 4.2 (b) in a large scale scan of 281 nm × 281 nm area. A small area scan clearly resolved the atoms and as well as defect states. There are two types of defects visible, and one of the defects is very similar to the defects seen in the case of $PdTe_2$ shown in chapter 3. This triangular type of defects is formed due to Se vacancy. The calculated interatomic distance is $\sim 4.0 \pm 0.1$ Å. After confirming the surface quality, we performed spectroscopy on Sb_2Se_3 in a defect-free area. One representative spectrum averaged over 512 spectra is shown in Figure 4.2 (d). The U-shaped spectral feature whereas the flat bottom area does not become absolutely zero, clearly indicates that the material is a semiconductor with a bandgap of 800 meV. The crystal structure of Sb_2Se_3 in the [001] direction is shown in Figure 4.2 (a).
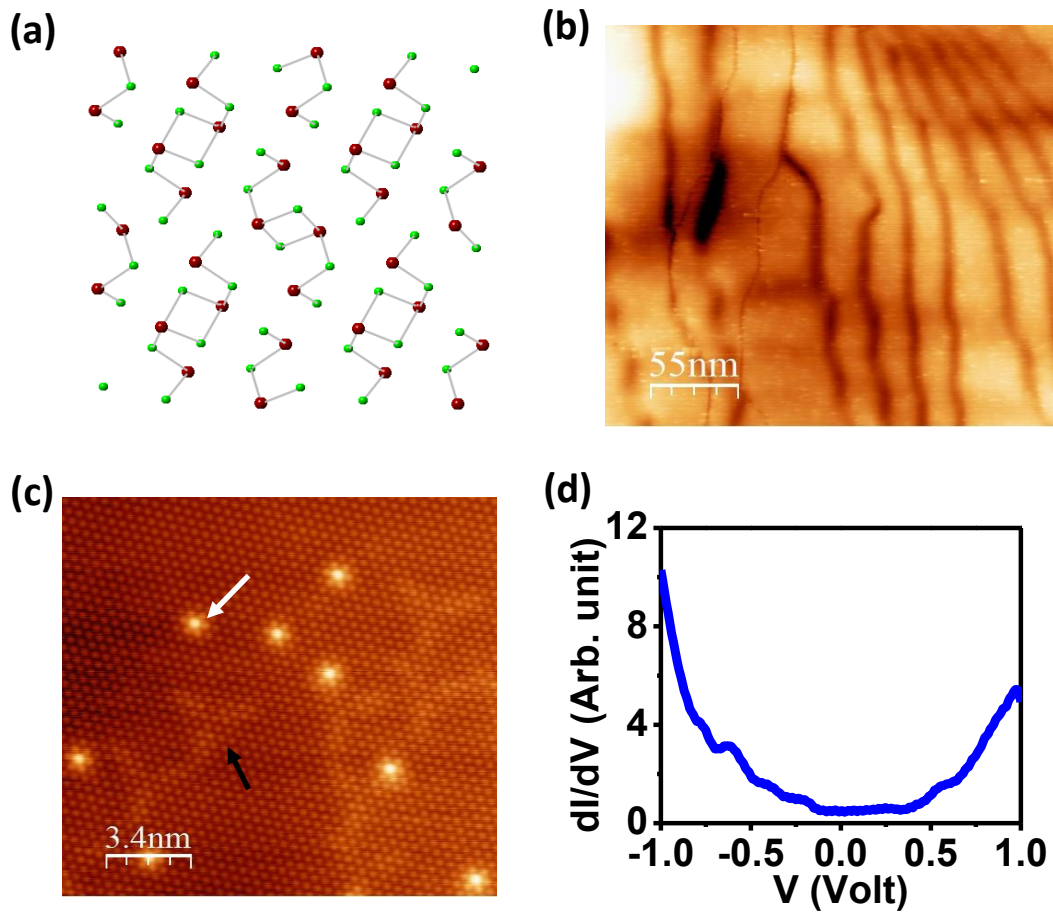
Figure 4.2: (a)Crystal structure of Sb$_2$Se$_3$ along [001] direction. (b) Large area (281 nm × 281 nm) scan shows atomic terraces on the surface of Sb$_2$Se$_3$. V_s = -700 mV, I_s = -100 pA (c) An atomic resolution image of Sb$_2$Se$_3$ at 17 K. Two types of defects are indicated by black and white arrows. V_s = -700 mV, I_s = -110 pA (d) dI/dV spectrum at 17 K indicates semiconducting energy gap. V_s = -700 mV, I_s = -110 pA, V_{mod} = 10 mV and f$_{mod}$ = 1.12 kHz

4.2   Study of defect states:
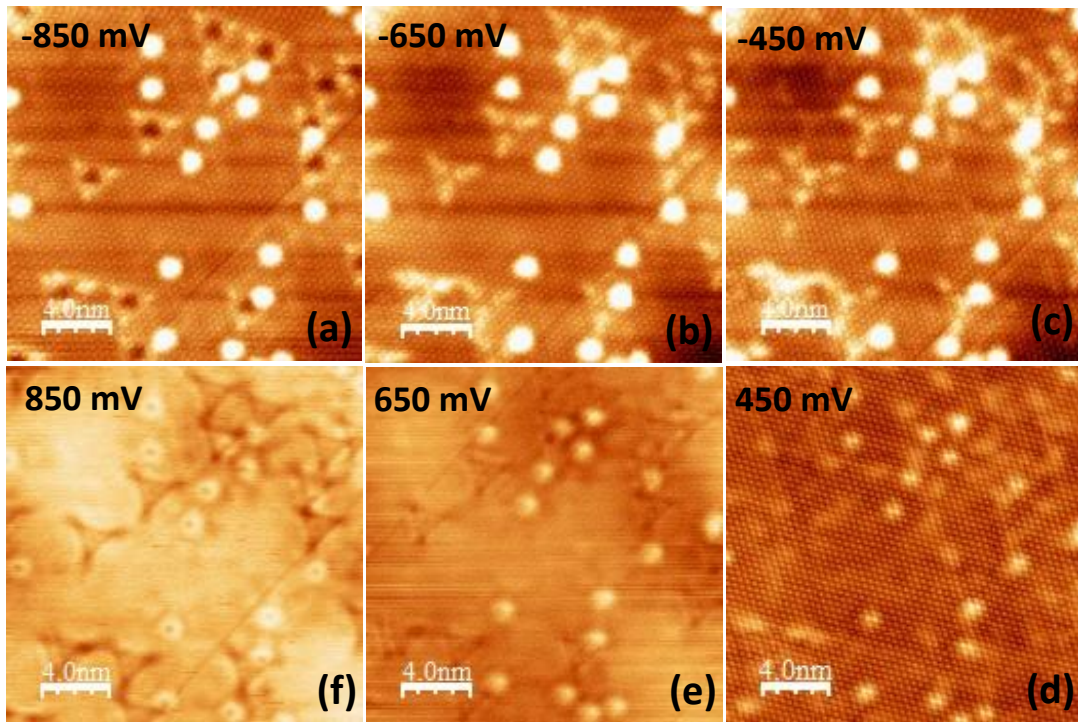
Figure 4.3: Evolution of defect states with energy. The topography of defect states captured at (a)-850 meV, (b)-650 meV, (c) -450 meV, (d) +450 meV, (e) +650 meV and (f) +850 meV. I$_s$ = $\mp$ 300 pA

In order to look at the behaviour of the defect states of the material projecting on the surface we carried out the STM scanning at different energies spanning over -850 mV to +850 mV (Figure 4.3 (a)-(f)). It is clearly seen that the defect states change intensity and shape with energy and all the triangular type of defects are aligned in the same direction and the alignment is independent of energy. The defect states are also more prominent in -ve bias with respect to the positive bias. Therefore, the defect states show an asymmetric behaviour with the direction of the applied bias.

4.3 QPI on Sb$_2$Se$_3$:

To investigate the surface states more precisely we performed local density of states (LDOS) map on Sb$_2$Se$_3$ surface. From the LDOS map, we can also reconstruct the quasiparticle interference pattern (QPI) (For more details of QPI Please see Section 1.3).
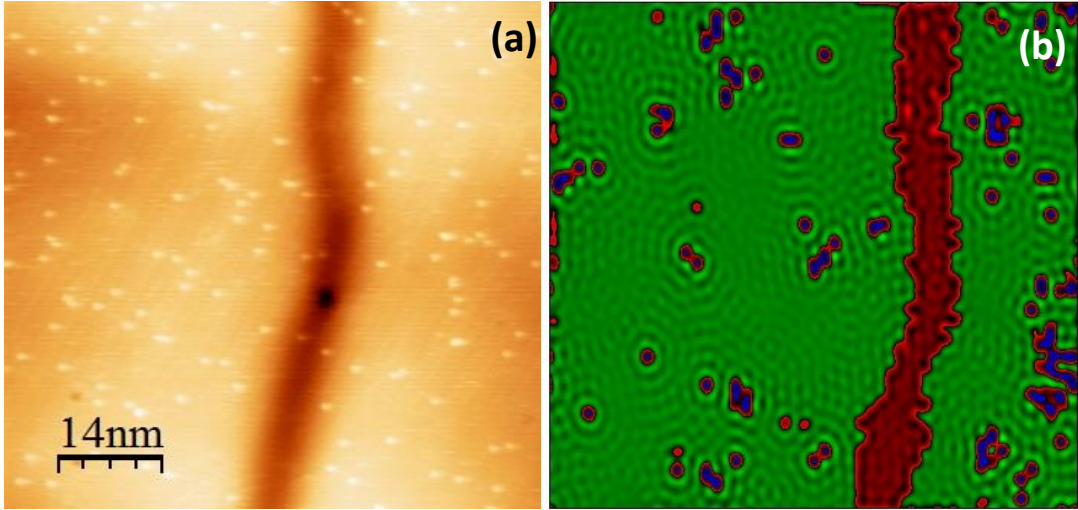
Figure 4.4: (a) LDOS map on a selected area of 70 nm x 70 nm containing two atomically sharp steps on Sb$_2$Se$_3$. V_s = -700 mV, I_s = -100 pA, V$_{mod}$ = 10 mV, T = 17 K, H = 0 G (b) Quasi-particle interference patterns are seen in the LDOS map of Sb$_2$Se$_3$ surface after removing the background noise.

The 70 nm $\times$ 70 nm LDOS map is shown in Figure 4.4 (a). One valley and a lot of defects are seen in this image. After the Fourier filtering of this image, the QPI patterns have become prominent (Figure 4.4 (b)). The interference pattern is forming around the defects and boundaries. This particular area was chosen intentionally in order to look at the QPI patterns prominently where the defect states and a valley are both present.

4.4   Spin polarization measurement on Sb$_2$Se$_3$:

Till now we intended to look at the surface states of Sb$_2$Se$_3$. As I mentioned earlier that Sb$_2$Se$_3$ is not a topological insulator, the more convincing explanation that we can see from our STM/S study on this material. The spectroscopy clearly shows that the Sb$_2$Se$_3$ is semiconducting in nature. In a topological insulator, the intensity of QPI pattern diminishes because the backscattering and as well as a wide-angle scattering is prohibited [49, 187]. Here in our case the prominent QPI pattern further confirms that it is not a topological insulator.

Now, we know that Sb$_2$Se$_3$ is a strong spin-orbit coupling semiconductor. To measure the spin-polarization of the material we performed point-contact Andreev reflection spectroscopic measurements on Sb$_2$Se$_3$ single crystals with two different superconducting tips (Pb and Nb: both are conventional superconductor). In Figure 4.5 (a)-(d) we show the representative Andreev reflection spectra with the Pb (red in colour) and Nb (blue in colour) tips. The sharp dip at $V = 0$ and two shallow peaks about $V = 0$ in dI/dV vs. V spectra clearly reveal the suppression of Andreev reflection (the reason behind this suppression has been described in Chapter 1). The experimental data were fitted with modified BTK model (See chapter 1) for the finite spin polarization of the nonsuperconducting electrodes. The theoretical fits are exactly lying on the experimental curves. The theoretical model includes the parameter spin polarization (P) which gives the value of spin polarization in the point-contact geometry at a certain barrier Z. The strength of the barrier height causes the normal reflection of quasiparticles from the barrier,
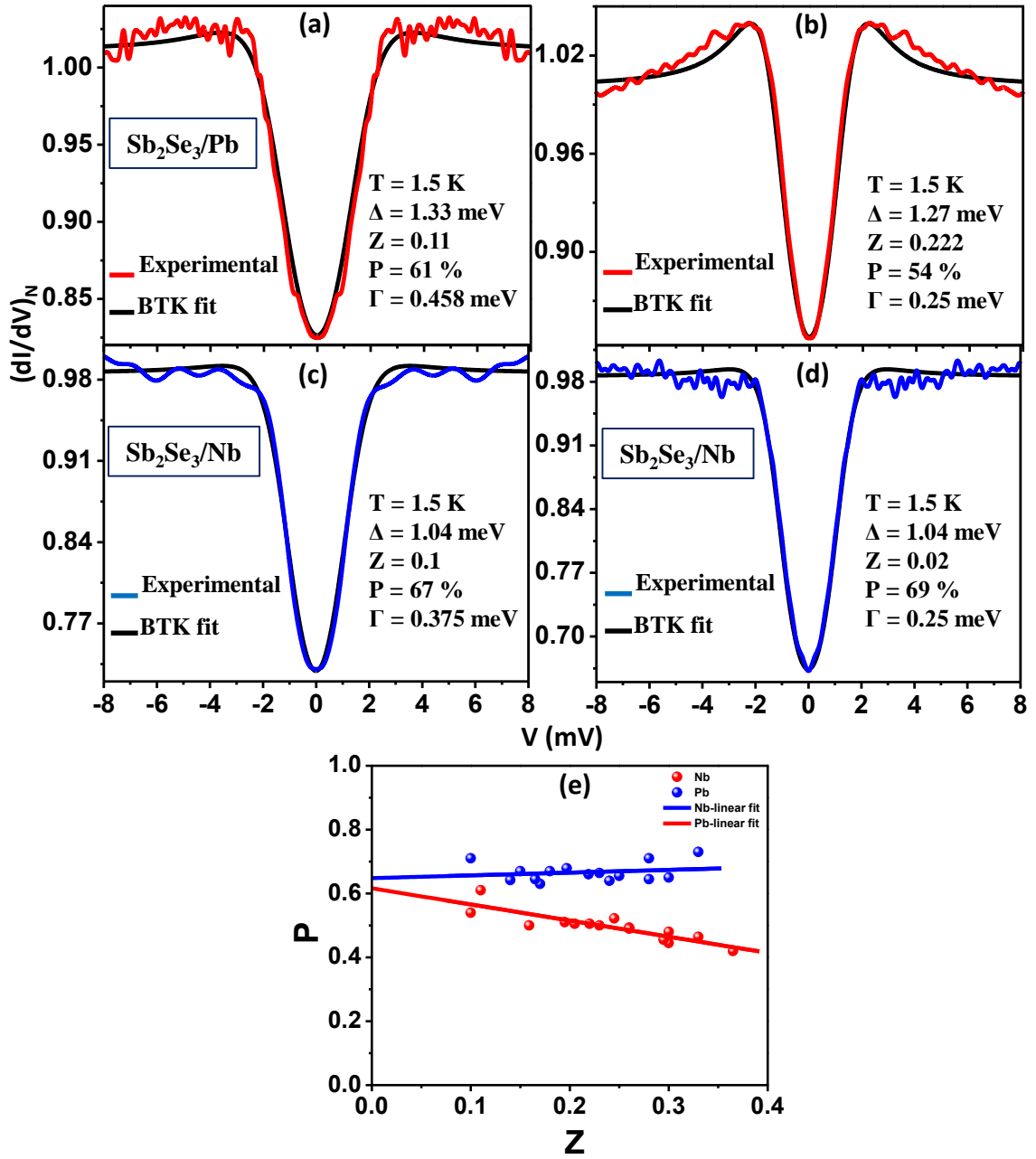
Figure 4.5: Normalized dI/dV spectra for point-contacts on Sb$_2$Se$_3$ with (a,b) Pb tip and (c,d) Nb tip. The black lines show BTK fits with spin-polarization included. (e) Spin polarization (P) vs. barrier strength (Z) plot. The solid lines show extrapolation to Z = 0 where the spin-polarization approaches 70 %

and due to this, we will not get the actual value of spin polarization. In practice, it is not possible to achieve $Z = 0$. In order to get the maximum intrinsic spin polarization value, we plotted P as a function of Z for a large number of point-contacts. We extrapolated with the linear fit, and at $Z = 0$, it gives the maximum intrinsic spin polarization of 70 %. The value of spin polarization is quite high incomparable to some ferromagnetic metals such as, Fe ($P = 40\%$), Co ($P = 42\%$), Ni ($P = 39\%$) [126]. It is also comparable to the spin polarization of 70 % in case of Bi_2Te_3 and some other topological insulators [95]. In the previous study in topological insulators, the data fitted with two gap parameters. But in our case, the data are fitted with a single gap parameter. The gap values are 1.3 meV in case of Pb tip and 1.5 meV in case of Nb as expected for a normal metal-superconductor point-contacts. The analysis involved only three effective parameters, P, Z and Γ where Γ is the effective broadening parameter. Some of the previous reports claimed the pressure induced superconductivity and topological phase transition in Sb_2Se_3 [172]. But in the point-contact setup with a soft tip, it is not possible to withstand such high pressure. Therefore, the measurements are not pressure induced in our case. Though the material is not a topological insulator, it shows such a high spin polarization. This indicates that the some of the states of Sb_2Se_3 might be topologically trivial with nontrivial spin texture present due to strong spin-orbit coupling.

4.5 Angular magnetoresistance in Sb_2Se_3:

In order to further confirm the presence of a spin-polarized current, we have performed angular magnetoresistance (AMR) of the ballistic point contact. The magnetic field direction was rotated using a 3-axis vector magnet with respect to the direction of the current. The angular magnetoresistance data is shown in Figure 4.6 (a), (b). A large anisotropy in the angular magnetoresistance is observed. This anisotropy in magnetoresistance can be explained if we assume the point-contact geometry as a nano-wire and the magnetic field is rotated perpendicular to the direction of current flow through the nanowire [169]. This anisotropy is well described by a $\cos 2\phi$ field-angle dependence, where ϕ is the relative angle of rotation of the applied magnetic field [169, 188].

Here, the AMR data with Nb tip fitted well with $\cos 2\phi$ dependence. But in case of Pb tip, it fitted well with $\cos (2.25)\phi$. This deviation is also observed in the past [169]. In order to further confirm whether the anisotropic angular magnetoresistance is originating from the superconductivity and/or point-contact geometry, we performed a similar experiment in four probe geometry. In Figure 4.6 (c) we show that in the four probe geometry the AMR is anisotropic as well. Such anisotropy is also observed in the case of Bi_2Se_3 [189]. The anisotropy is well fitted with $\cos 2\phi$ dependence. This result confirms the anisotropy is coming from the material Sb_2Se_3 itself and the strong spin-orbit coupling governs it. In the measurement technique we choose two electrodes—one is superconductor (Pb/Nb), and another one is Sb_2Se_3. In the thermal regime of point-contact, we could see the critical cur-
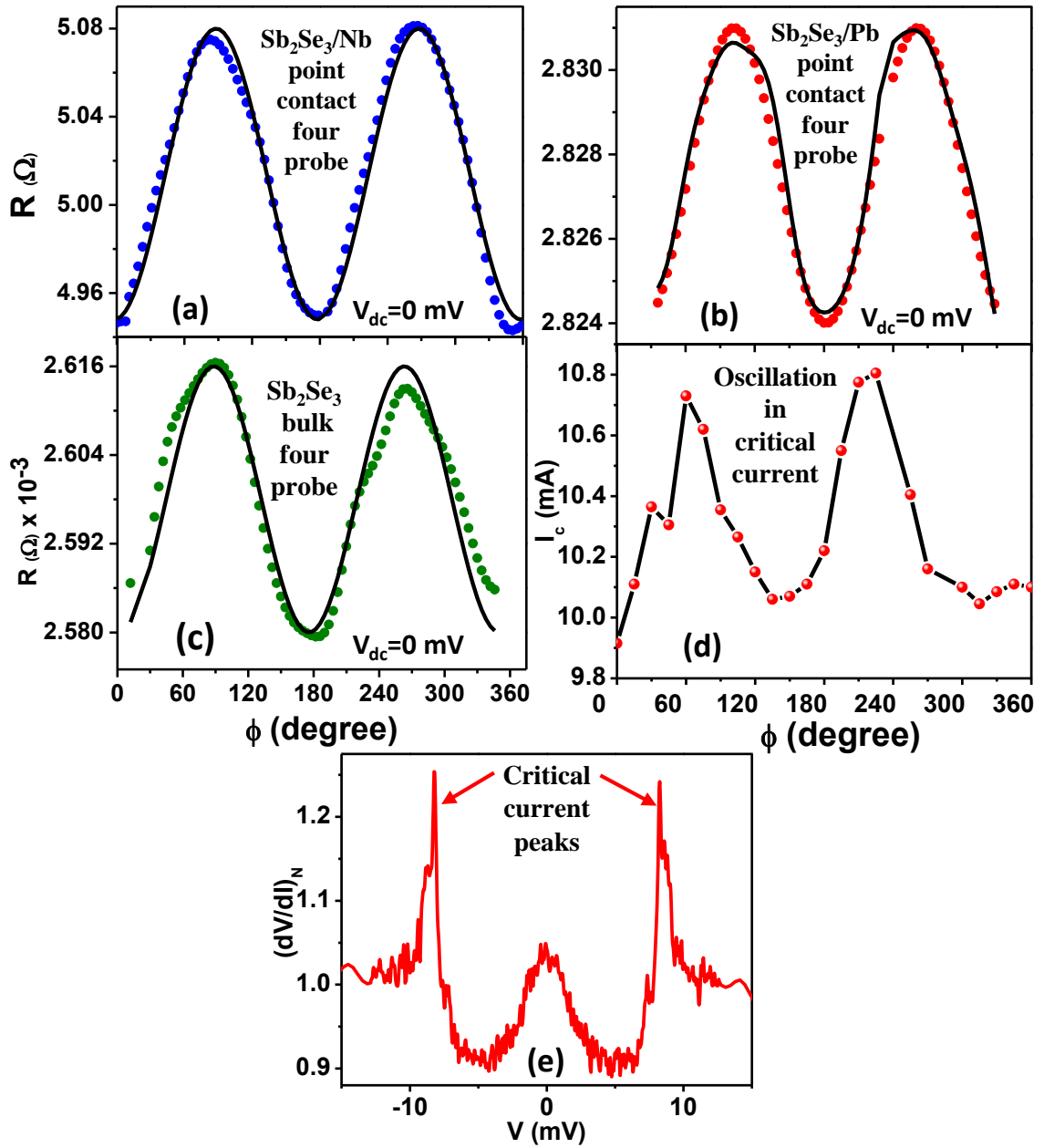
Figure 4.6: Anisotropic angular magnetoresistance of (a) a point contact on Sb_2Se_3 with Nb. (b) with Pb tip. (c) Bulk Sb_2Se_3 crystal. The black lines show a $\cos 2\phi$ fit. (d) Anisotropy of the critical current of a superconducting point contact in the thermal regime. (e) The corresponding thermal regime dV/dI spectrum.

rent peaks in the dV/dI spectrum. In this method, superconductivity induces on the other electrode via proximity effect. If an anisotropy exists in the system, the critical current should modulate with respect to the field-angle. In order to investigate the modulation of the critical current, we acquired data for field angle dependence of a thermal regime point-contact spectra. The critical current values also oscillate with the magnetic field direction. This data supports the previous data presented in Figure 4.6 (a)-(c). A representative point-contact spectrum is shown in Figure 4.6 (e). The system with high spin polarization shows anisotropy in AMR was observed before in the case of ferromagnetic materials [190]. So the AMR data further confirm the existence of spin dependent transport in Sb_2Se_3.

4.6 Magnetoresistance in Sb$_2$Se$_3$:

In order to further investigate the magnetic correlation in a different way, we performed magnetoresistance measurements on the single crystal of Sb$_2$Se$_3$. At zero dc bias voltage in the point contact geometry, a large negative magnetoresistance is observed (Figure 4.7 (b)). At 1.5 K the resistance shows a peak at zero magnetic field and suppresses at very weak magnetic field. With increasing temperature, the peak evolves gradually and smears out at 7 K which is the bulk T$_c$ of Pb. In order to confirm whether the magnetoresistance is due to the superconductivity of Pb alone, we performed a similar experiment at different dc bias voltages (Figure 4.7 (a)).
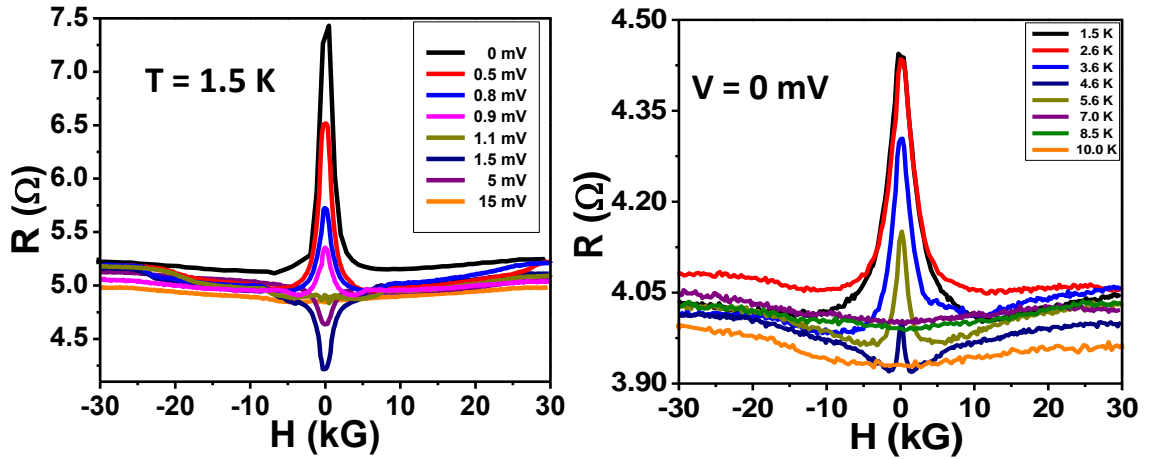
Figure 4.7: (a) Magnetoresistance of a Pb/Sb$_2$Se$_3$ point contact at different biases.Sample temperature (T) = 1.5 K. At 1.5 V the peak becomes dip.(b) Temperature dependence of the magnetoresistance.

The zero field peak decreases gradually, and surprisingly the peak becomes a dip at 1.5 mV and finally smears out at 15 mV which is far above

the superconducting energy gap of Pb. This confirms that the magnetoresistance is not entirely originating from superconductivity. The interesting thing happened at 1.5 mV. The zero field peak becomes a dip. Such high negative magnetoresistance was observed in the past in certain nontrivial systems [191]. The alternation of the peak was also observed before with applied gate bias was ascribed to a transition from weak-anti-localization dominated transport to weak-localization transport [192, 193]. Here, in case of Sb_2Se_3, this could be a possibility of the reversal of the magnetization.

4.7   Theoretical study on Sb_2Se_3:

In order to understand the possibility of spin-polarized surface states, we investigated the band structure of our Sb_2Se_3 crystals. Our Sb_2Se_3 crystals have an orthorhombic structure with space group *Pmna* with the lattice constants of a=4.0345Å, b=11.5681Å, c=12.7341Å; $\alpha = \beta = \gamma$ =90°. The band structure calculations were performed using density functional theory within the Local Density Approximation (LDA) exchange-correlation as implemented in the Vienna ab-initio simulation package (VASP) [194]. Projected augmented-wave (PAW) pseudo-potentials are used to describe the core electron in the calculation [195]. The electronic wave function is expanded using plane wave up to cutoff energy of 265 eV. Brillouin zone sampling is done by using a (10x10x10) Monkhorst-Pack k-grid. Both atomic position and cell parameters are allowed to relax until the forces on each atom are less than 0.01 eV/Å.

Sb$_2$Se$_3$ in the typical rhombohedral structure does not have enough spin-
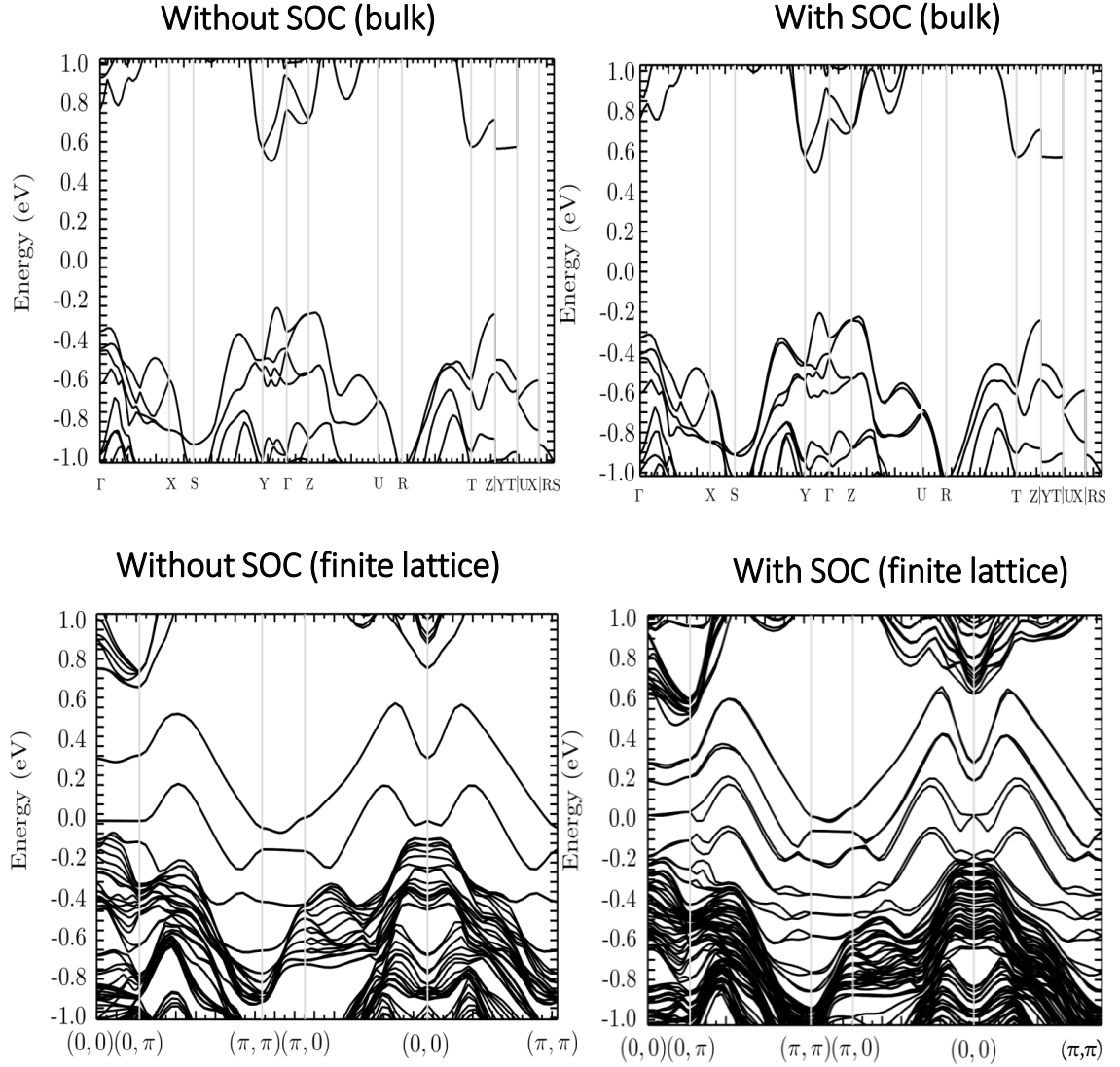
Figure 4.8: Band structure of Sb$_2$Se$_3$ (a)for bulk without SOC, (b) for bulk with SOC, (c) for finite lattices without SOC (two trivial surface states available), and (d) for finite lattices with SOC (one trivial surface state splits due to Rashba SOC).

orbit coupling strength to cause topological band inversion [23]. The studied orthorhombic phase of Sb$_2$Se$_3$ has higher crystal symmetry. It has tendency to reduce the spin-orbit coupling strength in the bulk [196]. The DFT calcu-

With SOC (finite lattice)
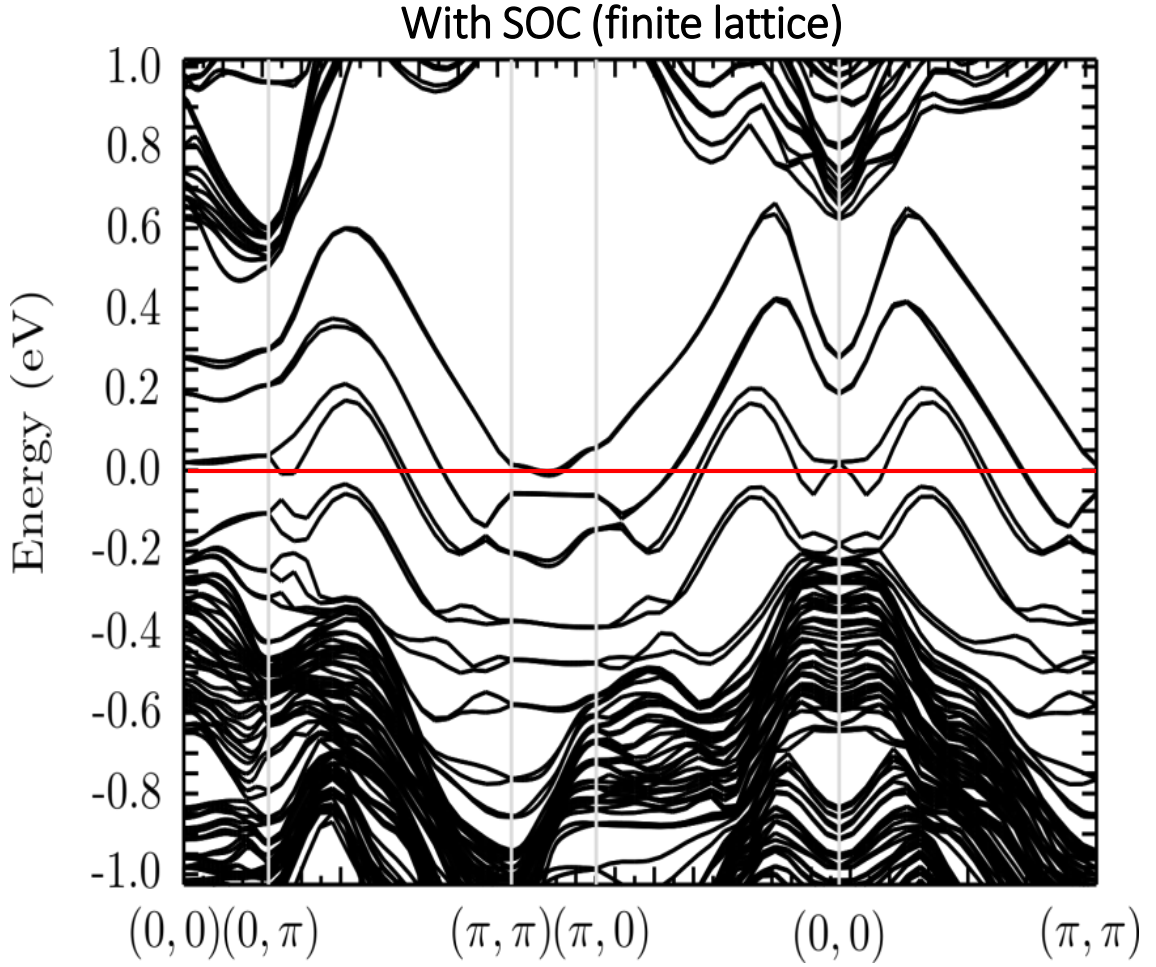
Figure 4.9: Band structure of Sb_2Se_3 for finite lattices with SOC (one trivial surface state splits due to Rashba SOC) (zoomed in view)

lations for the bulk phase without spin-orbit coupling indicates that this is a band insulator with a gap of ~ 1 eV (Figure 4.8 (a)). With spin-orbit coupling in the bulk phase no signature of band inversion is observed either (Figure 4.8 (b). However, surprisingly, for a finite lattice without spin-orbit coupling, we found two trivial surface states available when the sample cleaved perpendicular to the c-axis but not in the other two orthogonal directions (see structure in Figure 4.2 (a)). The bandstructure is shown in Figure 4.8

(c). The point-contact Andreev reflection and STM/S experiments were carried out on the same crystal plane. By introducing the spin-orbit coupling with the finite lattice, these two states split due to Kramer's degeneracy [32] (Figure 4.8 (d). Here, the surface states generate spontaneously and do not follow bulk-boundary correspondence. Therefore, those are trivial surface states. In Chapter 1, I have described that if the surface states intersect the Fermi level even number of times, then the surface states is trivial in nature but when it intersect an odd number of times the then the surface states are non-trivial in nature. In Figure 4.9 it is clear that the Fermi level (red line) cuts the surface states even number of times everywhere which implies that the surface states are trivial in nature. Among these two states, one shows a large splitting at the surface due to Rashba type spin-orbit coupling. The spin-splitting is ~ 800 meV which is comparable to the experimental data. This large spin-splitting may lead to the large value of spin-polarization measured in point-contact measurements. Thus, The DFT calculation supports our experimental observation.

4.8   Conclusions:

The actual behaviour of Sb_2Se_3 was quite debatable. Here, using STM measurements, we proved experimentally that Sb_2Se_3 is not a topological insulator. The theoretical study says that two trivial surface states available on Sb_2Se_3. We have performed spin-polarized Andreev reflection spectroscopy and detected highly spin-polarized surface states in the topologically trivial band insulator Sb_2Se_3 with strong spin-orbit coupling. The band structure

calculations also revealed that one of the trivial surface states undergoes spin splitting due to Rashba-type SOC thereby giving rise to the observed large value of the spin polarization. Moreover, we observed highly anisotropic magnetoresistance in the basal plane of the Sb_2Se_3 crystals which supports the claim the existence of magnetic correlations.

CHAPTER 5

Tip-induced superconductivity in $Pb_{0.6}Sn_{0.4}Te$

Study of topologically nontrivial systems in multiple numbers of approaches is a fascinating work nowadays. People have discovered many exotic phases of matter from these topologically nontrivial systems. Looking for Majorana fermions, excitation for topological superconductors are an active area of research in condensed matter physics. By applying perturbations like doping [162–165], pressure [155–161] etc. on topological materials to discover exotic phase of matter widely explored. Recently, the discovery of tip-induced superconductivity probed through point-contact Andreev reflection spectroscopy (PCAR) in such materials opened a new approach in experimental physics [167–169]. Previously studied materials were in semimetal classes. Here, I have explored the technique in a topological crystalline insulator (TCI). TCI surface states are protected by crystal symmetry [82]. TCI surface states are easily tunable by perturbations to emerge exotic phases [85].

Recently, $Pb_{0.6}Sn_{0.4}Te$ was shown to be a TCI confirmed by angle-resolved photoemission spectroscopy (ARPES) [197]. The solid solution composi-

tion $Pb_{0.6}Sn_{0.4}Te$ derived from PbTe (Eg $\sim$ 0.29 eV) and SnTe (Eg $\sim$ 0.18 eV,inverted gap). Being motivated from the previous discoveries and tunability of TCIs, we choose $Pb_{0.6}Sn_{0.4}Te$ to explore. Here, we show that $Pb_{0.6}Sn_{0.4}Te$ which is not a superconductor ($R - T$ curve shown in Figure 5.1), the used tip (Ag and Pd) are not superconductors but as soon as the mesoscopic point-contact made between the tip and sample, the confined region underneath the tip become superconducting.
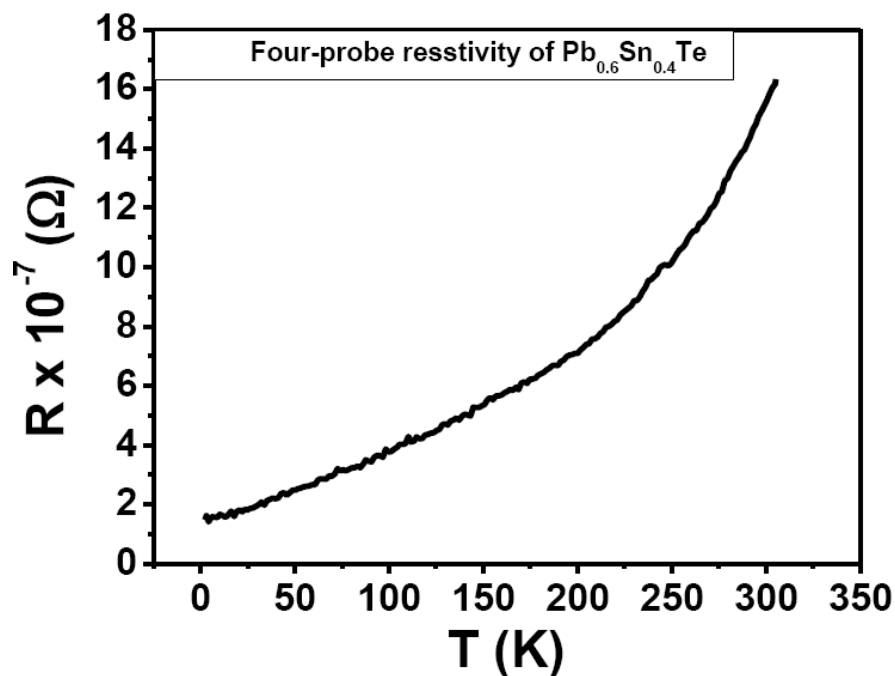
Figure 5.1: $R - T$ curve of $Pb_{0.6}Sn_{0.4}Te$ shows metallic behaviour. No superconducting transition down to 2 K.

5.1   PCAR on $Pb_{0.6}Sn_{0.4}Te$

Figure 5.1, the four probe measurement on $Pb_{0.6}Sn_{0.4}Te$ do not show any superconducting transition down to 2 K. Pd and Ag is not known to be a superconductor within this temperature range. But the superconductivity emerges at the point-contacts between tip and sample. A lock-in based dI/dV modulation technique was utilized to probe the superconductivity — the details of the measurement technique described in chapter 1. In order to understand in a better way, first I will discuss the results on some known/standard sample. As a test case, first, we used Pb superconductor, $T_c = 7.1$ K) as a sample and Ag (normal metal) as a tip. Secondly, we chose Cu (normal metal) as a sample and Nb (superconductor, $T_c = 9.2$ K) as a tip. In both the cases, the superconducting transition was seen at respective transition temperatures of the superconductors (right *insets* of Figure 5.2 (a) and (b)). Therefore, in the point-contact geometry, we could see the superconducting transition in the R-T curve. It should be noted that the resistance in the superconducting region doesn't reach zero even for a conventional superconductor. The reason may be due to (a) the existence of a non-superconducting component of the point-contact, (b) existence of some ballistic channels cause Sharvin resistance even when the thermal contacts dominate effectively, and (c) the intrinsic mismatch of the Fermi-velocities in the two electrodes forming the point-contact. Another way to probe this superconductivity is $I - V$ characteristic measurement. A lock-in based first derivative technique is employed to get better resolution.

Such modulation technique also utilized here. Figure 5.2 (a) and (b)
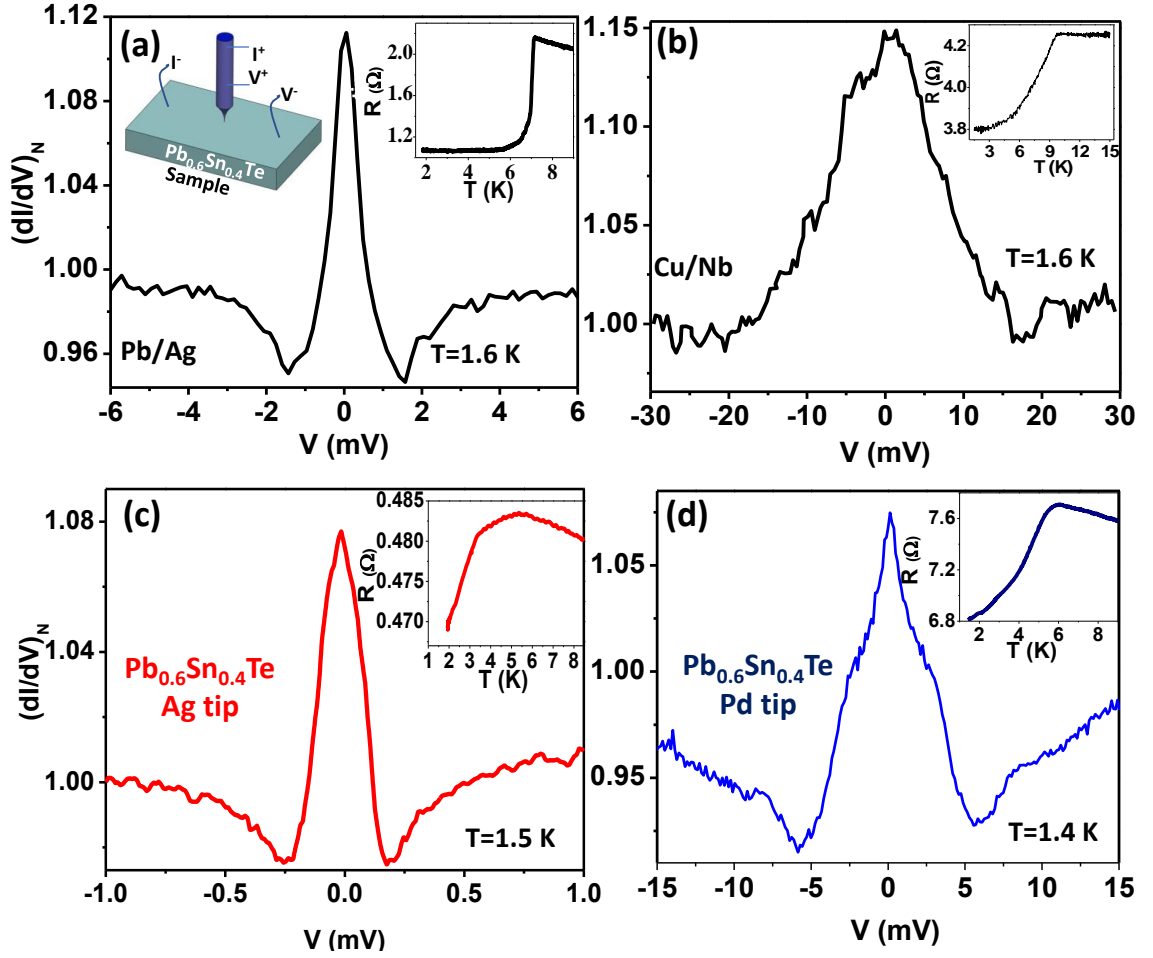
Figure 5.2: (a) A normalized dI/dV spectrum, point-contact between Ag (tip) and Pb (sample), a conventional superconductor. *Inset:* A schematic diagram showing the point contact on $Pb_{0.6}Sn_{0.4}Te$ with measuring electrodes (left) and R–T data showing superconducting transition at 7.1 K (right). (b) A normalized dI/dV spectrum, point-contact between a conventional superconductor Nb (tip) and Cu (sample). *Inset:* R–T data showing superconducting transition at 9.4 K. A normalized dI/dV spectrum for a point-contact on $Pb_{0.6}Sn_{0.4}Te$ with (c) an Ag tip (d) a Pd tip. *Inset:* R–T data showing superconducting transition at 5.4 K and 6 K, respectively.

show the representative dI/dV vs V spectra at 1.6 K for the conventional superconductors Pb and Nb respectively. Therefore, the signature of superconductivity in the thermal limit of point-contact is a sharp dI/dV peak at

$V = 0$ and two critical current dips about $V = 0$.

After ensuring the results on the conventional superconductors, we performed similar experiments on our target material $Pb_{0.6}Sn_{0.4}Te$ with two normal metallic tips Ag and Pd. Interestingly, similar results were observed on $Pb_{0.6}Sn_{0.4}Te$ point-contacts as in the standard superconductors.

In the inset of Figure of 5.2 (c) and (d) the resistive transitions are clearly seen at 5.5 K and 6.5 K for Ag tip and Pd tip respectively. The dI/dV vs. V spectra show a sharp peak at $V = 0$, and two critical current dips are also seen about $V = 0$. From the presented data it seems that the point-contacts of $Pb_{0.6}Sn_{0.4}Te$ with the normal metallic tip is superconducting. In order to confirm further, we performed the experiment on huge number of different spatial points as well as on many sample flakes. Some of the representative spectra are shown in Figure 5.3. The red curves represent the point-contacts of Ag/$Pb_{0.6}Sn_{0.4}Te$, and blue curves stand for the point-contacts of Pd/$Pb_{0.6}Sn_{0.4}Te$. Some diffusive regime spectra are also seen where the Andreev reflection dip and critical current peaks both exist. Last four spectra represent for the same. Therefore, the superconductivity remained there underneath the point-contacts.
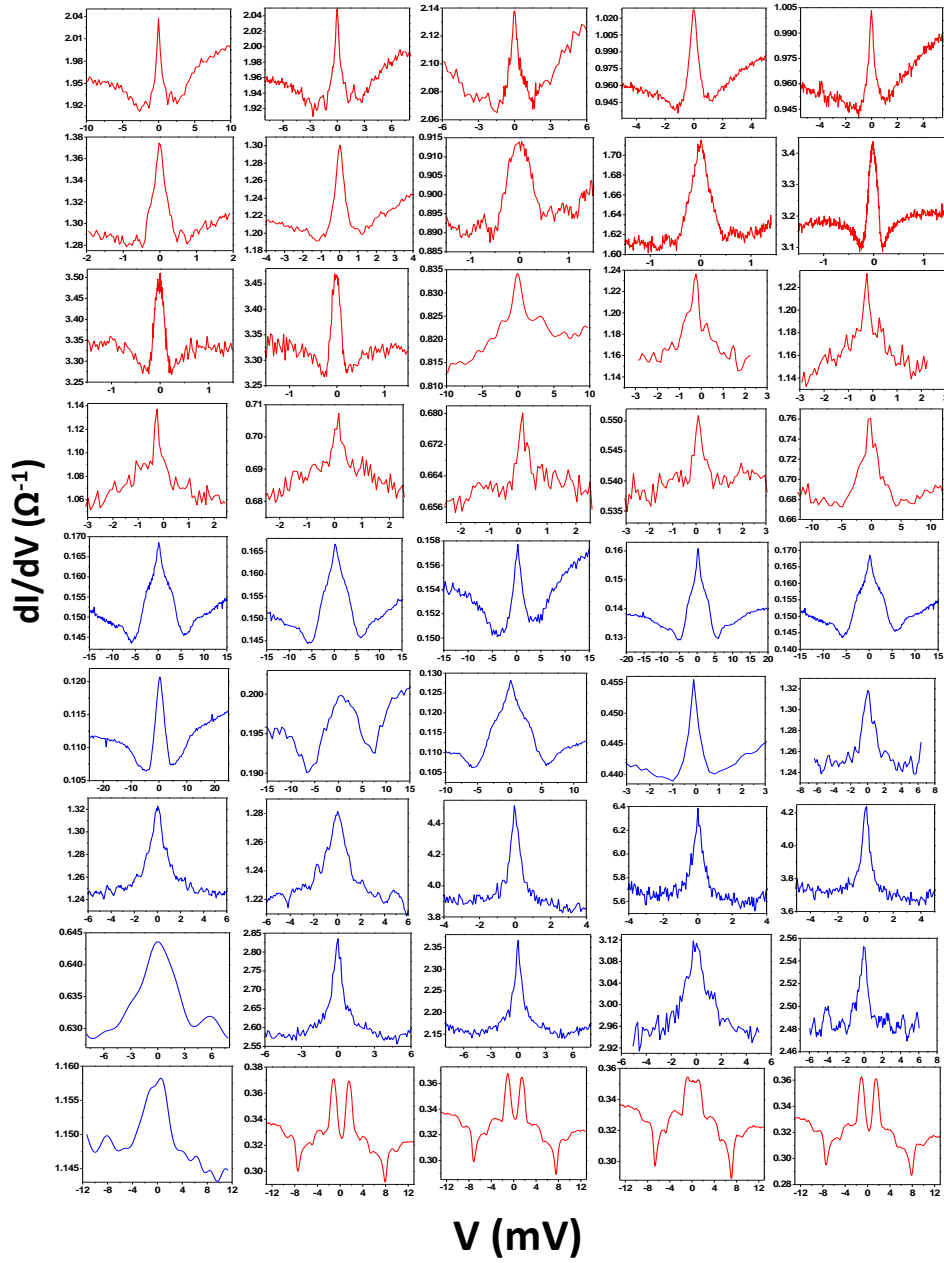
Figure 5.3: 50 representative point-contact spectra at different spatial points with Ag (red), Pd (blue) tips.

5.2 Proof of superconductivity:

To make sure the observation of superconductivity on the metallic point-contacts on $Pb_{0.6}Sn_{0.4}Te$, it is necessary to investigate the temperature and magnetic field dependence study on the point-contact of $Pb_{0.6}Sn_{0.4}Te$. In the following sections we will demonstrate all those points:

5.2.1 Magnetic field dependence of $R - T$ data:

To further confirm the superconductivity we did the magnetic field dependence of the $R - T$ data for both the point-contacts.
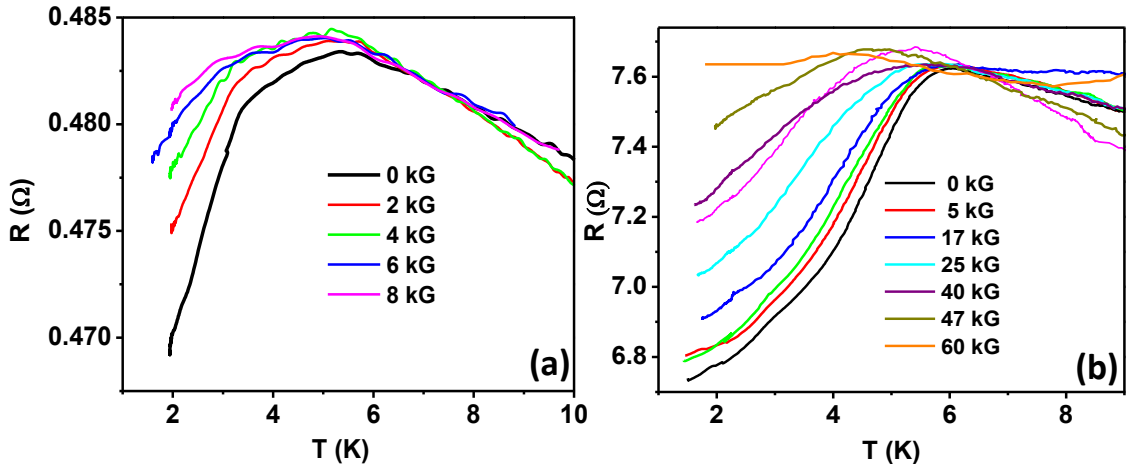
Figure 5.4: Magnetic field dependence of $R - T$ data for (a) Ag tip, (b) Pd tip.

The $R - T$ curves evolved with increasing magnetic fields systematically and suppressed at 8 kG and 60 kG for Ag and Pd tip respectively as expected for a conventional superconductor.

5.2.2 Temperature dependence of $dI/dV\,spectra$:

In a superconducting point-contact, the temperature dependence of the dI/dV spectral features should suppress with increasing temperature and vanish at T_c. Here, the dI/dV spectrum with increasing temperature is evolving gradually and disappears at 6 K. The 3-D interpolated curve shown in Figure 5.5. The dips about $V = 0$ indicate the critical current values for a superconductor. The temperature dependence of the critical currents is shown in the inset of Figure 5.5. The variation of the critical current with temperature is similar as expected for a superconducting point-contact.
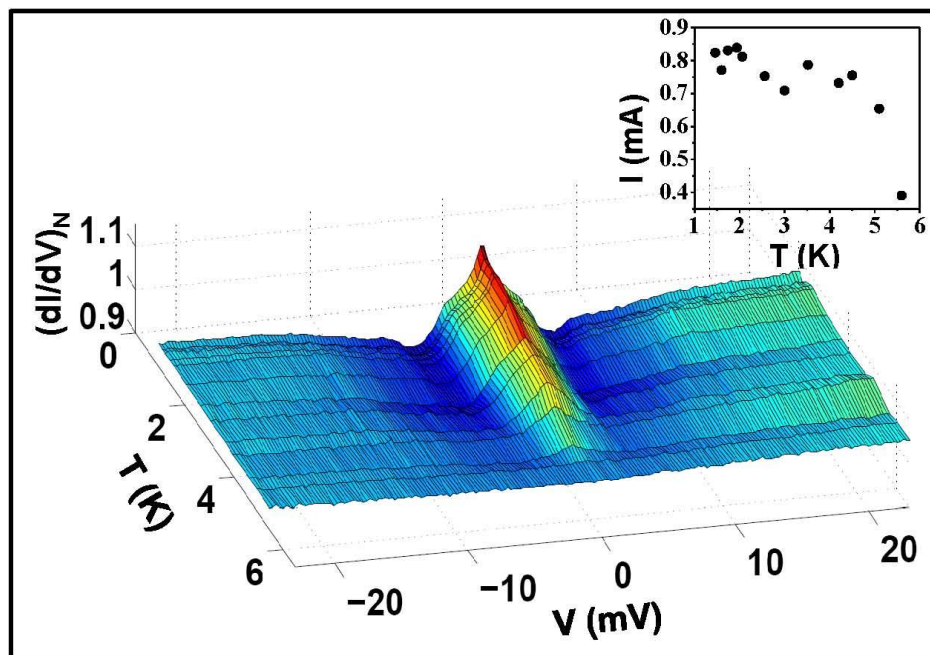
Figure 5.5: 3D interpolated curve of temperature dependence of dI/dV spectra. The spectral feature vanishes at T = 5.4 K. *inset:* Critical current decreases gradually with temperature.

5.2.2.1 Magnetic field dependence of dI/dV *spectra* :

Here, we show the magnetic field dependence of a $Pd/Pb_{0.6}Sn_{0.4}Te$ point-contact spectrum in Figure 5.6. As expected for superconducting point-contacts, the spectrum shows a monotonic decrease in the spectral features with increasing magnetic field and smears out at 6 T. The critical temperature as a function of a magnetic field is plotted in the inset of the Figure 5.6.
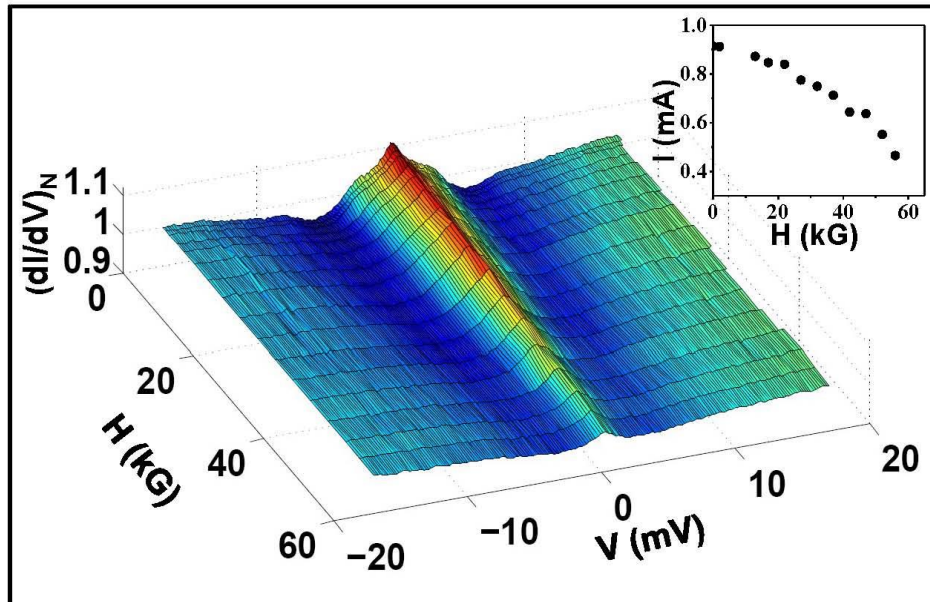
Figure 5.6: 3D interpolated curve of magnetic field dependence of dI/dV spectra. The spectral feature vanishes at H = 6 T. *inset:* Critical current decreases gradually with magnetic field.

5.3   Nature of superconductivity:

After confirming the superconducting phase in the confined region of $Pb_{0.6}Sn_{0.4}Te$ point-contacts, it is essential to investigate the nature of the superconduc-

tivity. As we didn't achieve the ballistic regime of a point-contact, we were unable to probe the superconducting energy gap directly. However, from the magnetic field dependence of $R - T$ curves, we could extract the H_c as a function of T_c. The $H - T$ phase diagrams are shown in Figure 5.7. With both the tips, the experimental data falls on the empirical dependence curve of a conventional superconductor within the error bar. The equation used for the empirical curve is,

$$H_c(T) = H_c(0) \left[1 - \left(\frac{T}{T_c} \right)^2 \right] \tag{5.1}$$
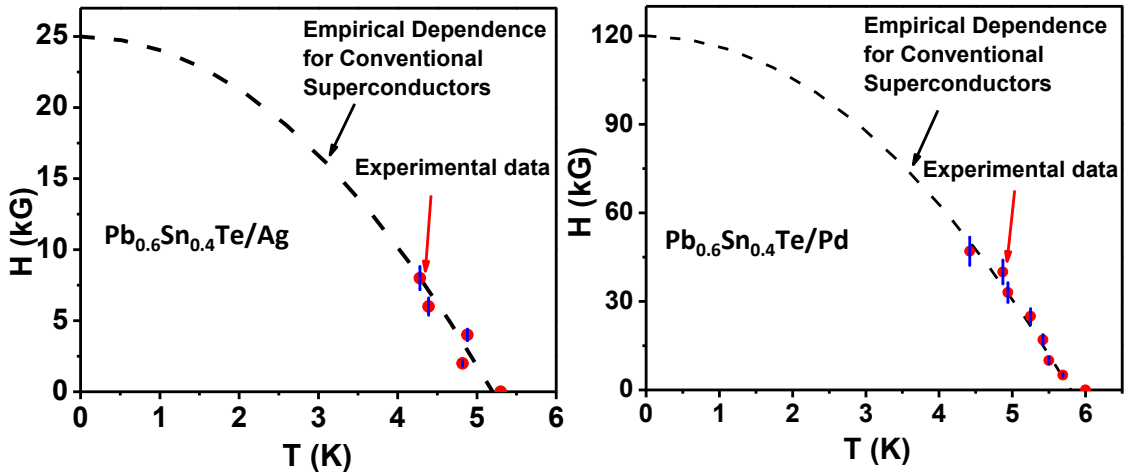
Figure 5.7: *H–T* phase diagram obtained for (a) Ag and (b) Pd point- ontacts on $Pb_{0.6}Sn_{0.4}Te$. These data have been extracted from Figures 5.4 (a) and (b) (error bars are also shown). The dotted lines show the empirical dependence expected for conventional superconductors.

As the transition points in $R - T$ data at higher magnetic fields were not clear, we could not extract the values from the curve. However, from the existing data points, we can say apparently that the tip-induced supercon- ductivity in $Pb_{0.6}Sn_{0.4}Te$ is conventional in nature.

5.4   Statistical evaluation of T_c and contact size:
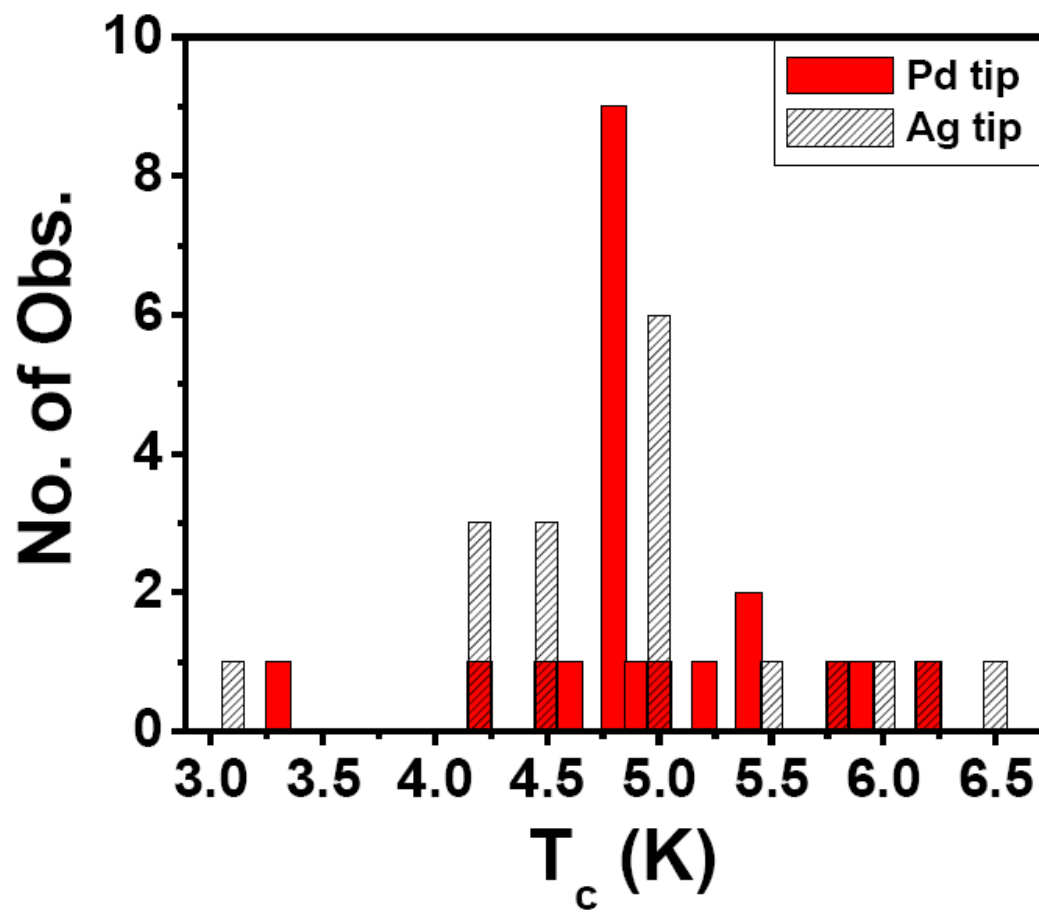
Figure 5.8: Statistical evaluation of T_c. (red) with Pd tip and (shaded) with Ag tip

With Palladium tip			
Contact no.	T_c (K)	Normal state resistance (Ω)	Contact diameter (a) in nm
1.	4.2	0.962	123
2.	5.2	0.274	227
3.	5.4	0.177	282
4.	5.4	0.268	229
5.	6.2	0.468	174
6.	5.0	0.341	204
7.	4.5	0.333	206
8.	4.8	0.312	213
9.	4.8	0.487	170
10.	4.8	0.612	152
11.	4.8	1.350	102
12.	4.8	1.000	119
13.	4.8	0.930	123
14.	4.8	0.744	138
15.	4.8	2.510	75
16.	4.8	0.477	172
17.	5.8	0.323	209
18.	4.6	0.980	120
19.	4.9	0.467	174
20.	3.3	2.210	80
21.	5.0	6.300	47
22.	5.9	7.600	43

With Silver tip			
Contact no.	T_c (K)	Normal state resistance (Ω)	Contact diameter (a) in nm
1.	5.8	1.430	99
2.	5.0	1.282	105
3.	5.0	1.255	106
4.	5.0	1.252	106
5.	4.5	0.724	140
6.	4.2	2.046	83
7.	6.5	1.456	98
8.	4.5	1.556	95
9.	5.5	1.420	100
10.	6.0	1.220	107
11.	5.0	1.012	118
12.	6.2	0.864	128
13.	4.2	0.858	128
14.	5.0	0.856	128
15.	4.5	0.736	139
16.	5.0	4.830	54
17.	4.2	3.600	62
18.	3.1	0.611	152

Table 5.1: Evaluation of contact diameters and T_cs at different PCs.

There are a lot of dissimilarities in measured T_c in different point-contacts with different tips ranging from 3.1 K to 6.5 K. I order to detect the actual T_c we made a statistical average of different point-contacts. Figure 5.8 shows the statistical evaluation of T_c. One can also measure the point-contact diameter from the Wexler's formula [118]:

$$R_{PC} = \frac{2h/e^2}{(ak_F)^2} + \Gamma(l/a)\frac{\rho(T)}{2a} \qquad (5.2)$$

where h is the Planck's constant, e is the single electron charge, a is the point-contact diameter, $\Gamma(l/a)$ is a slowly varying function of the order of unity, ρ is the bulk resistivity of the material and T is the effective temperature of the point contact. The contact diameters are calculated for different point-contacts. For each point-contacts, the value of T_c's are also measured. A tabular format of those data is shown in Table 5.1. The statistical average T_c is 4.7 K, and the average diameter is $\sim$ 150 nm. With this value, the calculated current density is $\sim 10^6$ A/cm^2 which is reasonable for a superconductor.

5.5 Point-contact on $\mathbf{Pb_{0.6}Sn_{0.4}Te}$ with ferromagnetic tips:

The above superconducting phase has been derived from a topologically non-trivial system. Therefore, there is a possibility to have unconventional pairing in the superconducting phase. Since, for a p-wave symmetry, the proximity of
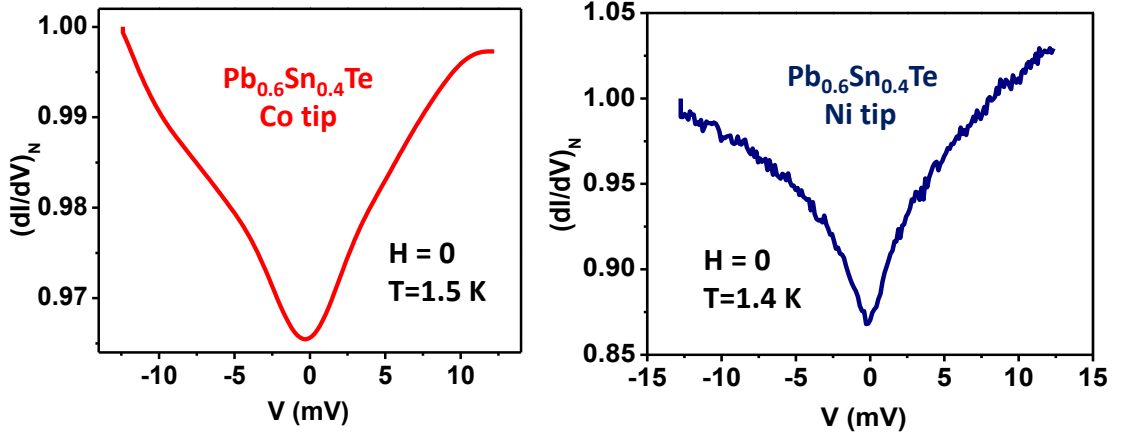
Figure 5.9: Representative point-contact spectrum (a) with a cobalt tip and (b) with a Ni tip on $Pb_{0.6}Sn_{0.4}Te$. Superconductivity is suppressed with ferromagnetic tips.

a spin-polarized Fermi surface should favour the superconductivity. However, we predict the above superconducting phase is a BCS type *i.e.* conventional in nature. In this context, the conventional BCS-type of superconductors with the proximity of a ferromagnet competes with and suppresses the super-conducting order. Here, we report our experimental results on $Pb_{0.6}Sn_{0.4}Te$ with two different ferromagnetic tips Co and Ni showed in Figure 5.9 (a) and (b) respectively. It is seen that with ferromagnetic tips the dI/dV spectrum does not show any feature as expected for a superconductor. The metallic ferromagnetic tip might be competing with the superconductivity and suppressed it. This data supports our previous prediction about the nature of the superconductivity.

5.6 Conclusion

$Pb_{0.6}Sn_{0.4}Te$ has low mobility ($\sim 10^4$ $cm^2V^{-1}s^{-1}$) which implies lower electronic mean free path. The system with lower mean free path has less possibility to achieve ballistic point-contact. In principle, the superconducting order parameter in the PCAR experiment could be confirmed by measuring the superconducting energy gap in the Andreev reflected dominated spectra. Here, we attempted to attain that phase but unable to retrieve due to the intrinsic disorder of the system. However, using the alternate method, we established that the point-contacts of $Pb_{0.6}Sn_{0.4}Te$ with the normal metallic tips are superconducting. The observed critical temperature is around 6.5 K which is intriguing. The existing theories predict the expected transition temperature in such systems is very low and mostly in the millikelvin regime. Moreover, the superconducting phase emerges in the nano-droplet under the mesoscopic point-contacts of a topological crystalline insulator with such a high critical temperature is even more interesting. However, Our study provided spectroscopic and transport data as a proof of the emergence of a novel superconducting phase at the mesoscopic point-contacts on the topological crystalline insulator $Pb_{0.6}Sn_{0.4}Te$. This discovery adds an important new candidate in the class of superconductors derived from topologically non-trivial systems. The results will be extremely helpful in understanding the origin of unexpected superconductivity in topological materials in general.

5.7 Appendix:

5.7.1 Material characterization:
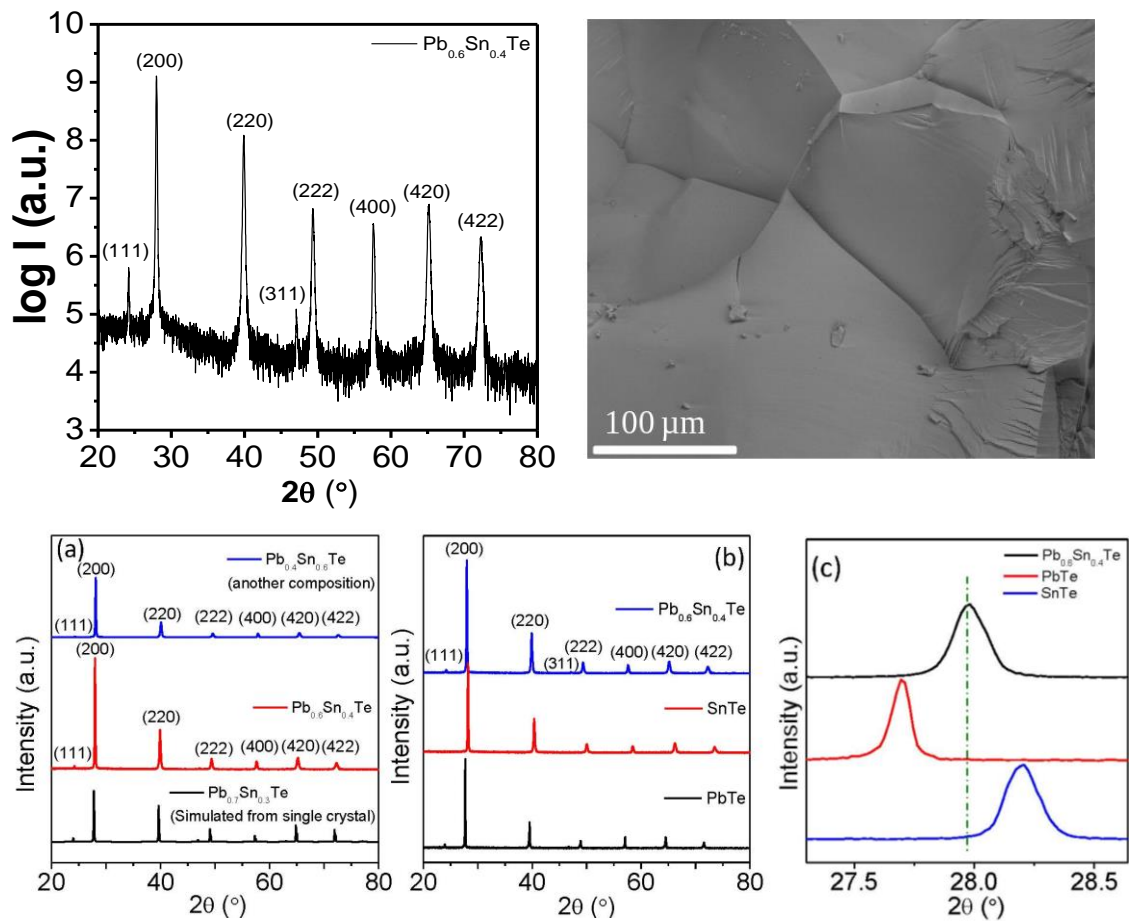
Figure 5.10: (a) PXRD patterns of $Pb_{0.6}Sn_{0.4}Te$ in logarithmic scale. (b) FE-SEM image of $Pb_{0.6}Sn_{0.4}Te$. Grain size ~100 μm (c) Powder X-ray diffraction patterns of $Pb_{0.6}Sn_{0.4}Te$ and $Pb_{0.4}Sn_{0.6}Te$ samples. Simulated PXRD from the single crystal of $Pb_{0.7}Sn_{0.3}Te$ are given for comparison. (d) Powder X-ray diffraction patterns of $Pb_{0.6}Sn_{0.4}Te$, PbTe and SnTe. (e) Zoomed XRD patterns from 27.2 to 28.6 degree for Figure (d)
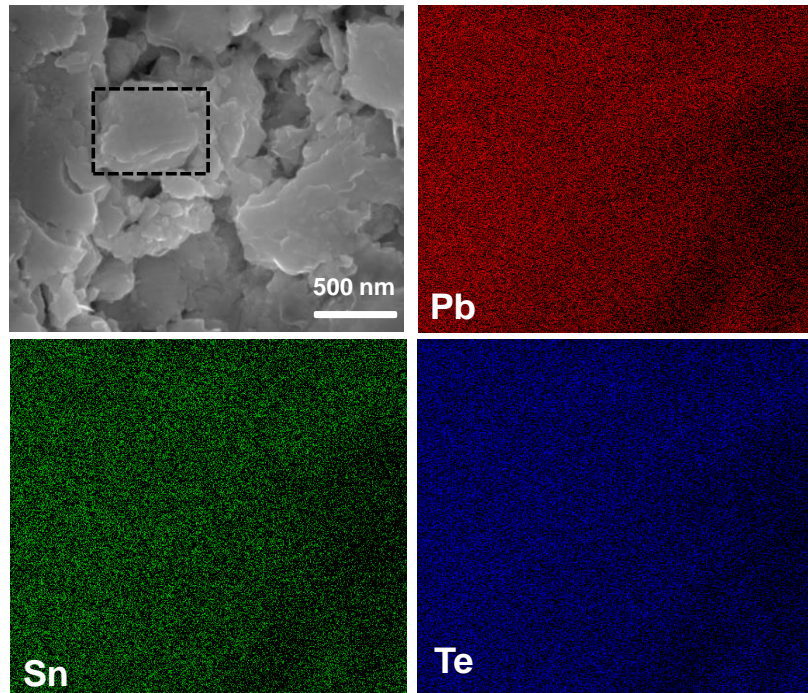
Figure 5.11: EDAX color mapping of freshly cleaved surface of $Pb_{0.6}Sn_{0.4}Te$ showing the presence of all elements (Pb, Sn, Te)

Stoichiometrically pure $Pb_{0.6}Sn_{0.4}Te$ samples were used for all the measurements presented here. Since Pb and Sn are also known superconductor, detailed elemental analysis has been performed to rule out the possibility of obtaining a superconducting signal from local clustering of Pb or Sn. Moreover, the transition temperature and the critical fields that we measure are significantly different from that expected for Pb or Sn. It should also be noted that the samples used for the presented measurement were polycrystalline in nature. However, as shown in Figure 5.10 (b), the grain size of the polycrystals are large ($\sim 100\mu$). The point-contact diameter is much smaller than the grain size. Therefore, the majority of the times the point-contact was established on a single crystallite.

5.7.2 Temperature and magnetic field dependence of dI/dV spectra with Ag tip:
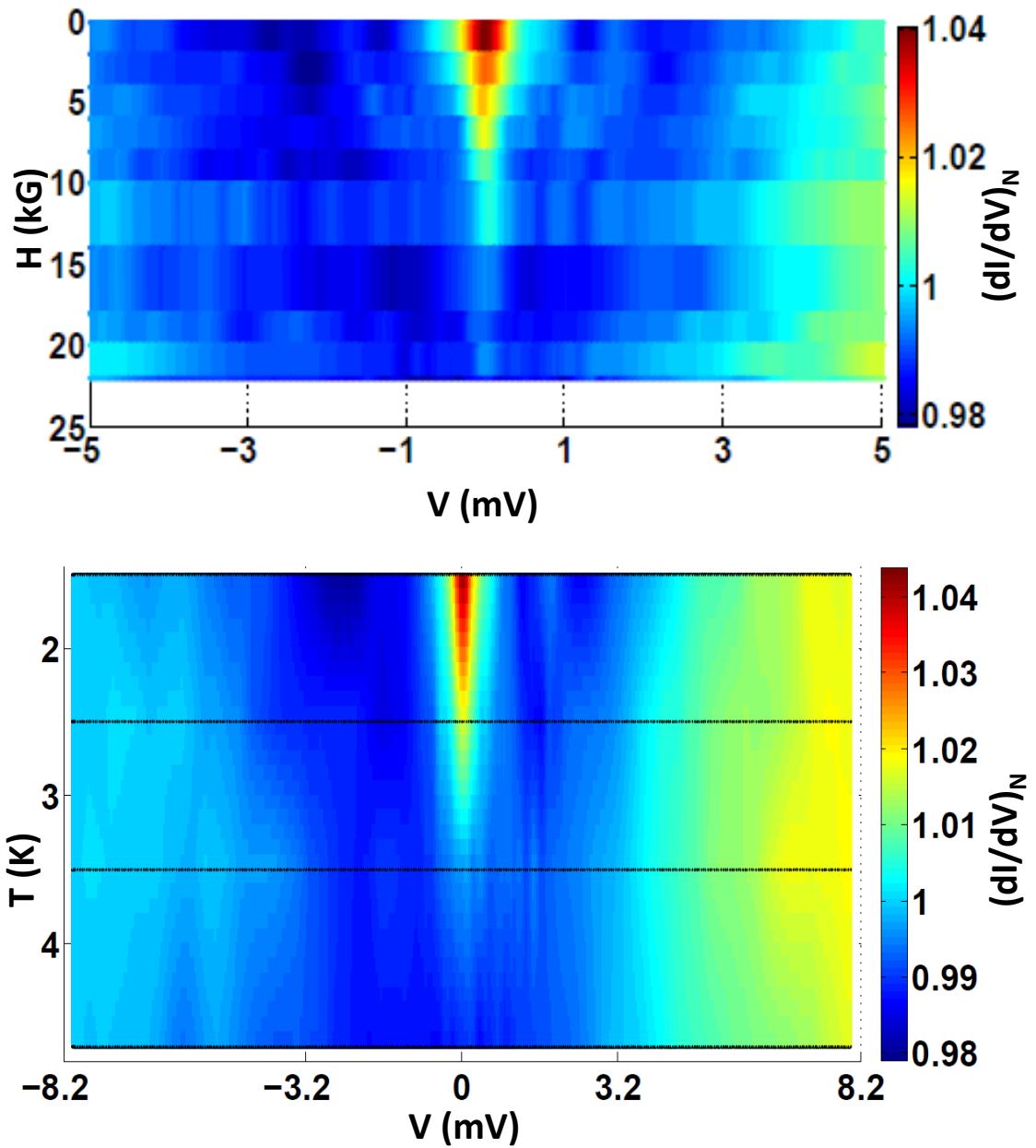
Figure 5.12: Temperature and magnetic field dependence of dI/dV spectra with Ag tip. Supports previous observations.

An additional temperature and magnetic field dependence of $Ag/Pb_{0.6}Sn_{0.4}Te$ point-contact is shown in Figure 5.12 (a) and (b) respectively.

CHAPTER 6

Instrumentation

Point contact spectroscopy (PCS) [113–116], the study of energy-resolved differential conductance and its higher orders, of a mesoscopic confined region is a popular technique that has been practised over decades to probe the electron-phonon interaction in metals and to characterize superconductors, in particular, to find the superconducting gap amplitude, symmetry of the order parameter *etc.* The details of this technique and data analysis has been shown in Chapter 1 and 2. Recently, PCS become very popular to study superconductors in particular, some phenomena like Andreev reflection [112], weak link Josephson effect [198, 199]. This method has been employed to study heavy Fermion superconductors [134], BiS_2 based superconductors [135, 136], pnictide superconductors [137], multi-gap superconductors [138]. Besides, this technique is also well known to measure spin-polarization in a ferromagnetic materials [126, 128] and topological insulators [95, 186]. Very recently, the discovery [166–169] of unexpected superconductivity in mesoscopic junctions of non-superconducting topological mate-

rial [32, 83] and elemental metal opens up a new paradigm in understanding the emergence of superconductivity in materials.

To perform such experiments, one should design and fabricate a probe assembly. Here we present the implementation of a home-built point contact probe operates down to ~ 346 mK. This detachable probe head can be inserted in any cryostat. However, We will demonstrate here the performance of this probe in a JANIS He3 cryostat goes down to ~ 292 mK. Using this assembly, we performed a spectroscopic study of superconductivity in Zr/PtIr under the point-contact down to 350 mK. We will discuss the design of the probe for ultra-low temperature operation in high vacuum and high magnetic field environment along with the details of instrumentation, measurement automation, and data analysis.

6.1   Experimental Details

6.1.1   Point-contact:

A most common way of making a point contact is achieved by moving a tip towards a sample in a very controlled way called the needle-anvil [113, 114] method (refer to Figure 6.1). The tip movement can be controlled manually by a differential screw or by a piezo-controlled nano-positioner. Another simple technique is the "Soft" contact method [113, 114] where the point-contact is made between the sample surface and $\sim 25\,\mu$m gold wire pasted with a small drop of silver epoxy. The effective cross-section of the point-

contact can be tuned by applying current (or voltage) pulses through it. The pulses destroy some of the existing conduction channels and/or creating new ones by piercing a small oxide layer on the surface of either electrode. The soft-contacts are mechanically and thermally better stable than the needle-anvil technique and does not involve any pressure applied to the sample (that is why called "soft"). However, the needle-anvil method, what we will discuss here, is non-destructive and more controllable. There are other methods [113,114] of making point-contact like shear method, break junction method. The small constriction can also be fabricated by the lithography technique.
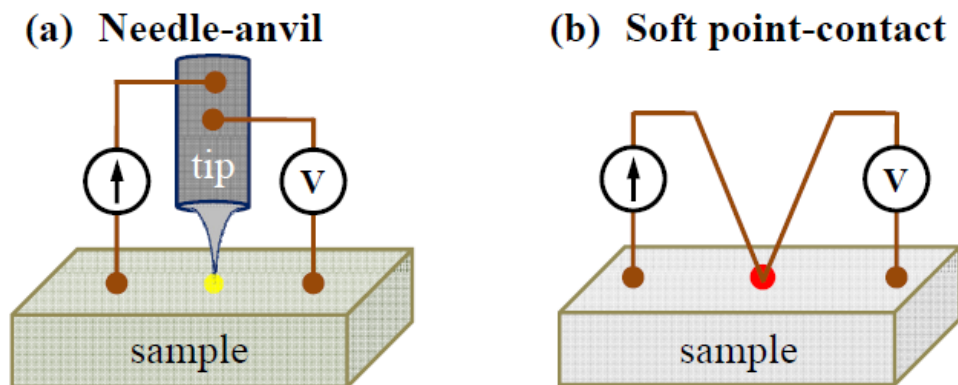
Figure 6.1: Schematic of a point-contact set up with electrical connections. **(a)** The needle-anvil method: the point-contact is made by approaching a sharp tip (needle) towards the sample by manual differential screw or piezo-controlled nano-positioner. **(b)** The "soft" point-contact: Using small drop of Ag-paste is used to make a soft point-contact on the sample.

6.1.2   Technical details:

Here we performed a PC spectroscopic measurements in a liquid helium based He3 cryostat (Janis Research, USA). The He3 insert goes inside the bore of a superconducting solenoid that can apply a magnetic field up to 7 Tesla in the vertical direction. Pumping on He-4 a base temperature of $1.4\,\text{K}$ is achieved, then the temperature further lowered down to $350\,\text{mK}$ using He-3 pumping.

6.1.3   Design of the probe:

For a He-4 system which goes down to 1.4 K, where exchange gas playing an important role to cool down the sample space is quite easy to fabricate and handle. However, for a He-3 system which goes down to sub-Kelvin temperature is a quite challenging job to transfer the sample space into the cryostat and cool down the sample space in a vacuum whereas the cooling power decreases with the temperature of the order of 10^{-4}. To increase the thermal conductivity we used oxygen-free high thermal conductivity (OFHC) grade copper in our probe assembly and to reach to the lowest temperature we reduced the maximal amount of thermal mass in every part of the probe. The PC probe is designed to work for ultra-low temperature application and to make the process easy for changing the sample/tip even in milli-kelvin without disturbing the vacuum insulation of the sample chamber. In order to fulfil these conditions we divided the probe assembly into four parts, (1) a load-lock chamber (LLC) with a differential pumping mechanism (figure 2(e,f)), (2) a vertical manipulator made of non-magnetic SS-316 (Figure 2(b)), a probe head (Figure 2(d)), and a sample space can (SSC) which is attached
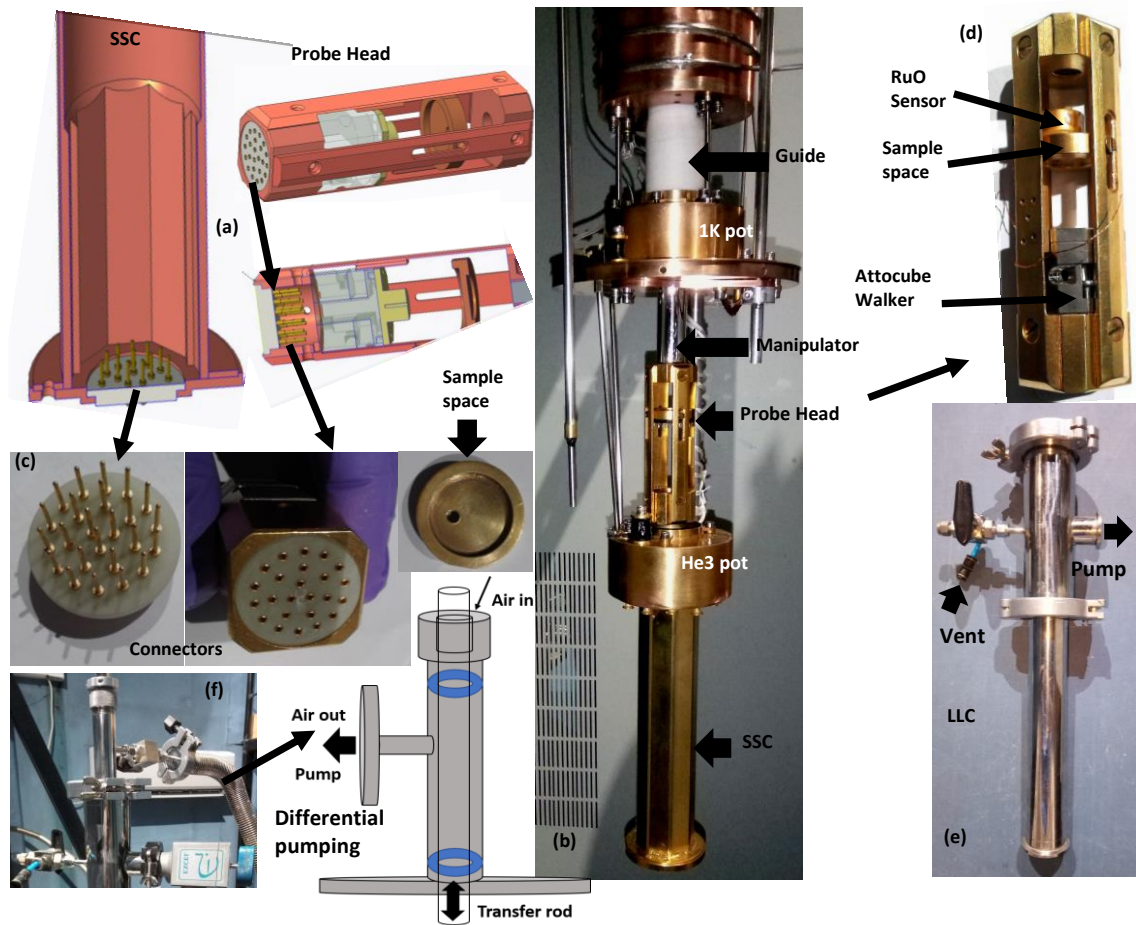
Figure 6.2: Detachable probe-head (needle-anvil type) designed for sub-Kelvin operation. A transfer rod is used to place it inside the He-3 cryostat. The tip movement is controlled electronically through piezo-driven walkers. **(a)** Schematic of the head and sample space can. **(b)** Real image of the unit. **(c)** Different components of the probe-head. **(d)** Zoomed view of the probe head. **(e)** Load -lock chamber. **(f)** Differential pumping assembly.

and thermally anchored with the coldest point of the cryostat (He-3 pot) (Figure 2(b)). The LLC is separated from the inner vacuum can (IVC) with a gate valve of size KF-40. The sample transfer mechanism is following, (1) First, we attach the probe head on the manipulator with threading and put it into the LLC. (2(e)) Then, we pump the LLC down to $\sim 10^{-6}$ mbar which

is comparable with the pressure of the IVC. (3) Once we get a good vacuum, we are ready to transfer the probe head. With the help of the vertical manipulator, we transfer the probe head into the SSC. To avoid the interruption of the vacuum during transfer, we implemented a differential pumping mechanism (depicted in Figure 6.2 (f)). (4) When the probe head reaches the SSC, inside which has a mating groove as in the outside of the probe head, it goes very smoothly. To get the groove quickly, we have marked an alignment mark with respect to a fixed point of the cryostat during installation. The probe head contains sample(s), tip, piezo-driven motor(s), heater, sensor(s) etc. shown in Figure 6.2 (c). All the wire connections from these parts go bottom of the probe head which has 24 pin mill-max female connectors (gold coated). The connectors are aligned so nicely that it matches with the mating male part in the SSC when the probe head enters into the groove. All the wire connections corresponding to the probe head parts are coming to the top of the cryostat via feed through from the bottom part of the SSC. (5) Once we confirm all the connections of the sample space, we un-thread the probe head from the manipulator and withdraw it to the LLC and close the gate valve and thermal shutter. Now we cool down the sample space by introducing minimal amount (20 mbar approximately) of helium exchange gas into the IVC. We pump out the IVC when the sample space temperature is at 40 K. Then we follow the regular condensation process of He-3 to get into millikelvine temperature. The whole process takes around 2 to 2.5 hours. (6) After cooling down the sample space and performing all the experiments, we remove the probe head in the similar way. We do not expose the probe head into the air suddenly when it is taken out from the cold bath. We keep

it in the LLC for a while. We have also implemented a controlled venting system with dry nitrogen gas. The lowest temperature on the He3 pot we reached down to 292 mK. Due to the thermal mass, the actual sample space temperature goes down to 347 mK measured using LakeShore temperature controller (Refer to Figure 3). As the manipulator is very long, it is difficult to get such straight pipe. To align the rod, we use a Teflon guide shown in Figure 2. The diameter and the length of the guide have been taken appropriately so that the manipulator does not misalign. The SSC and the probe head are made of copper with the gold coating on it. To avoid magnetic material we used all the screws made of gold-coated brass. A 50 ohm cartridge heater grooved inside and is equipped with a calibrated ruthenium oxide temperature sensor. The sample is glued fixed on the copper sample-stage using insulating varnish (sometimes thin quartz cover-slip is used in-between for better insulation). The tip-assembly consists of piezo-driven three-stage (x-y-z) coarse positioner (attocube ANPx101, ANPz101) and the tip-holder. The movement of the tip is electronically controlled through piezo-driven walkers similar to the coarse approach mechanism of STM tip and can be performed independently in all the three directions. The metal tips are fabricated by electrochemical etching or simply by cutting metal wires ($0.25\,\mathrm{mm}$ in diameter) and mounted on the tip holder (plug-n-play type with mill-max pin connector) with silver-epoxy. Two metal contact leads are fabricated on the tip, and two additional contacts are fabricated on the sample using silver-epoxy. Out of these four electrodes two are used to source current and other two to sense the voltage. We have twelve free connections to perform experiments on multiple samples simultaneously.
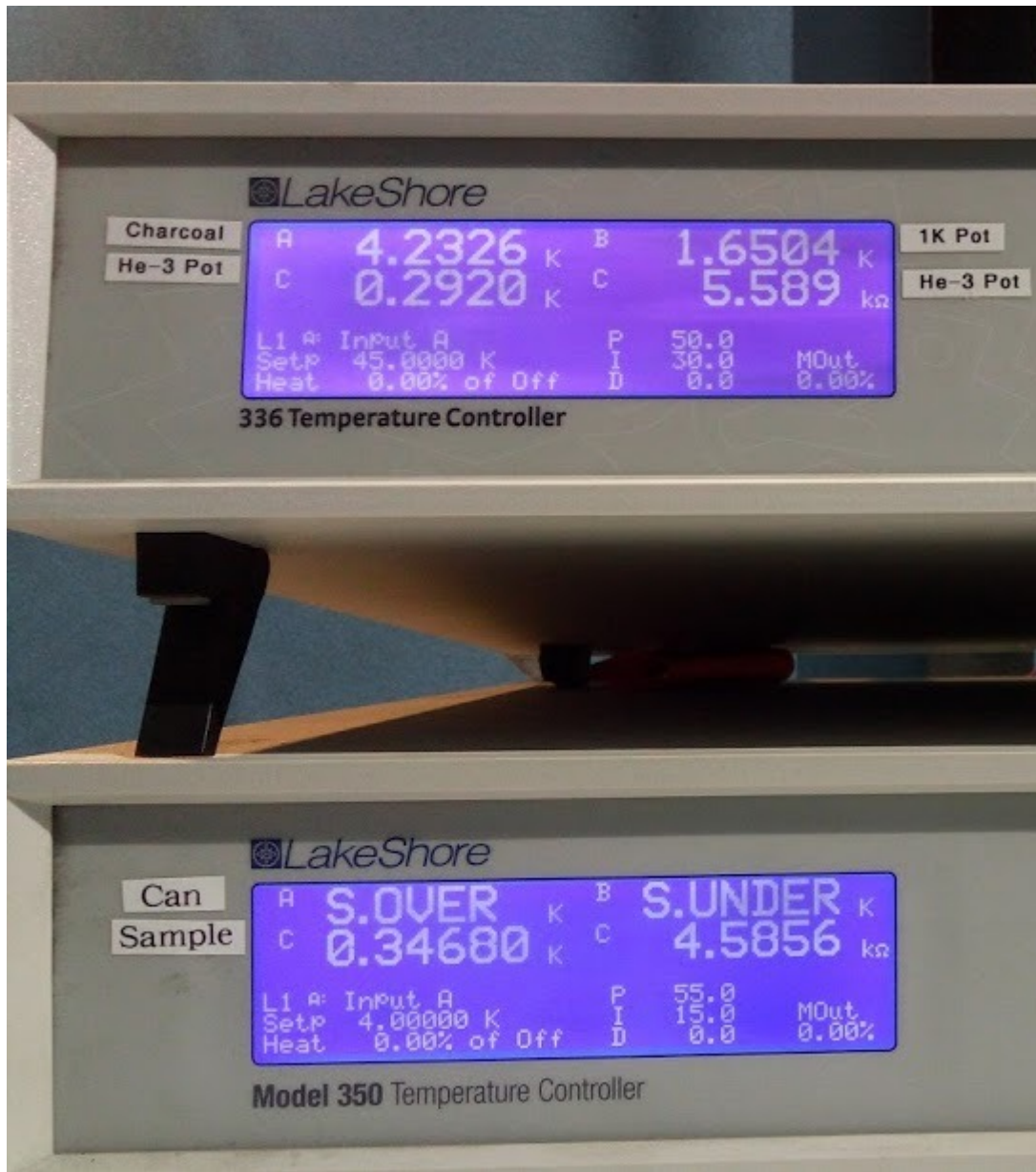
Figure 6.3: Minimum temperature reading at He-3 pot (292 mK) and sample space (347 mK) using LakeShore temperature controller.

6.1.4 Electrical measurement and automation:

Most of the measurement parts are described in Chapter 2. Here I will focus on the measurement in the millikelvin temperatures. At this temperature, a continuous flow of current will cause a heating in the contacts. To overcome this problem we developed an alternative measurement for the differential conductance can be performed in pulsed technique using Keithley 6221 with Keithley 2182A (nano volt meter). The pulsed technique measurement is very fast and suitable for low-power devices and/or in ultra-low temperature range (short pulses drastically reduces the Joule heating). The data acquisition is performed through GPIB connection and the measurement is made completely automated (using LabVIEW platform) with full control over the measurement parameters like temperature, magnetic field through interactive graphic-user-interface (GUI) as shown in Figure 6.4.
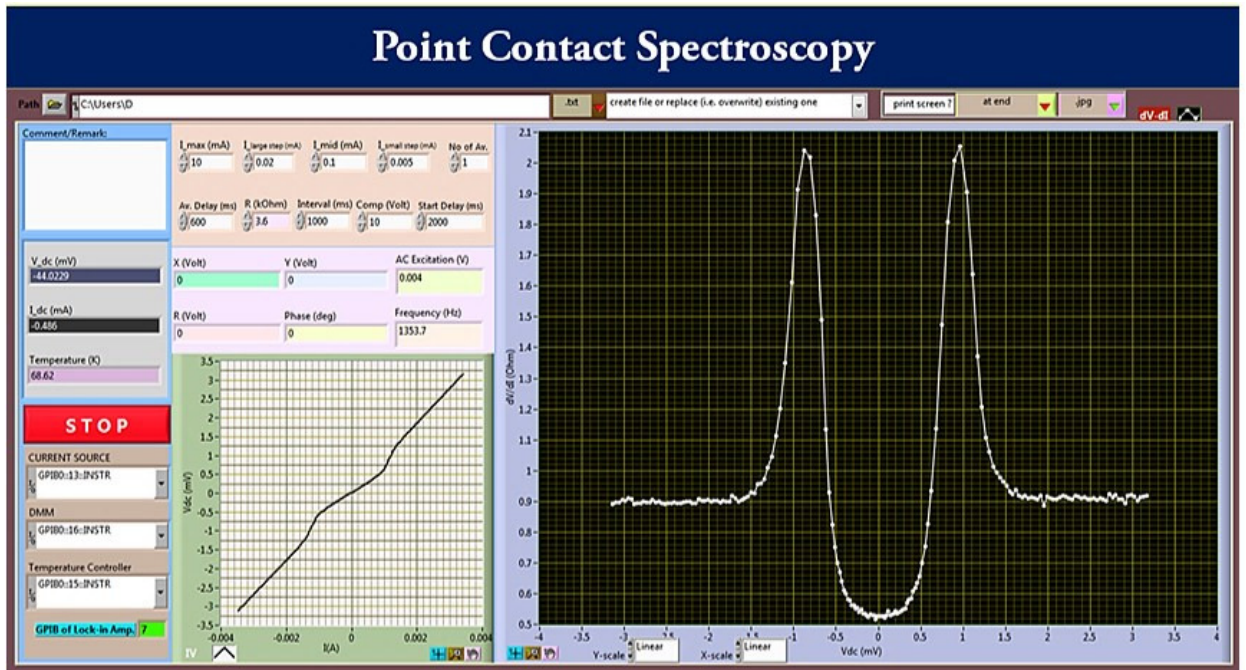
Figure 6.4: Interactive and user-friendly window for automated measurement.

6.1.5 Data analysis software:

We developed an interactive, user-friendly graphical user interface to furnish and analyze experimental data (refer to Fig. 6.5). Following Blonder-Tinkham-Klapwijk (BTK) [121] theory, one can simulate the PCS spectrum for a set of given superconducting gap amplitude (Δ), temperature of the junction (T), interface barrier strength (Z), quasi-particle life-time (Γ) and spin polarization (P) and can model fit experimental spectra.
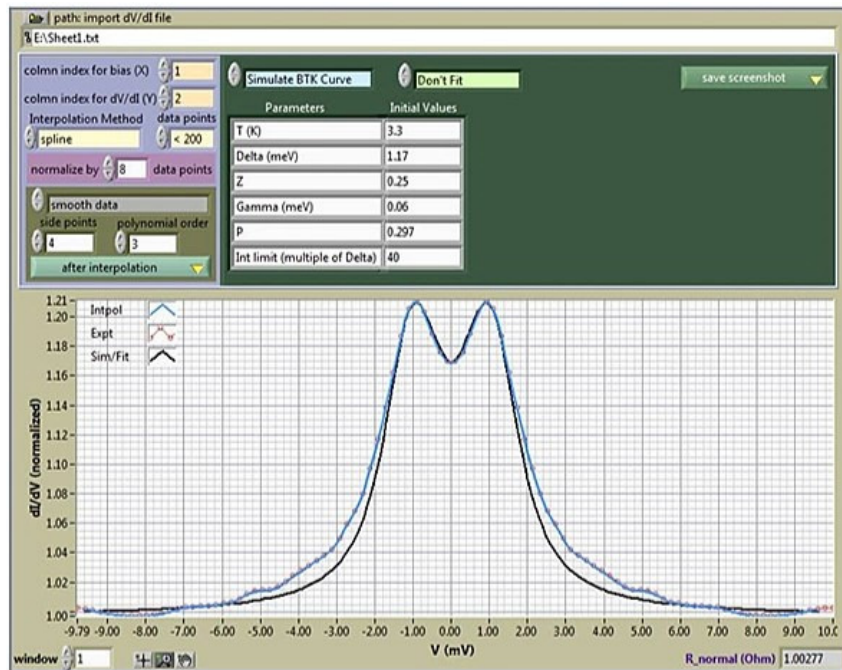
Figure 6.5: Interactive window for data analysis. One can simulate/fit PCS spectrum following BTK theory.

6.2 Results and discussion:

We performed an experiment on Zr/PtIr point contact. In Figure 7(a), we have shown a diffusive regime spectrum (red in color) with the BTK Fit (black in color). The lower portion of the spectrum where it is close to the ballistic limit is well fitted with the BTK simulation. The dips in the differential resistance about V = 0 is known as Andreev reflection dip. The corresponding superconducting energy gap we calculated is $\Delta = 0.510$ meV. In Figure 7(b) we have shown a representative spectrum of a thermal regime spectrum of Zr/PtIr point-contact. The peaks in the differential resistance about V = 0 is known as critical current peaks. As a conclusion, we suc-
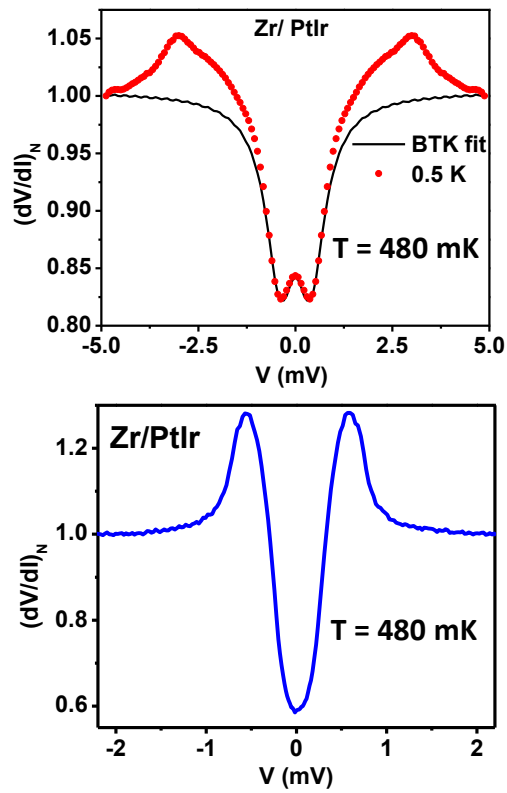
Figure 6.6: (a) A representative spectrum (red) of Zr/PtIr PC with the BTK fit (black). (b) A representative thermal regime spectrum of Zr/PtIr PC.

cessfully designed, fabricated and installed a probe which goes down to 347 mK and performed a point-contact measurement on Zr. With some minor modifications of the current probe, we can also do STM/STS experiments as well.

CHAPTER 7

Conclusion

In this thesis, I have investigated the electronic properties of few of the candidate topological materials using two powerful tools – Scanning Tunnelling Microscopy (STM) and Point-Contact Spectroscopy (PCS). It was found that these materials show unexpected behavior which is described below,

(i) $PdTe_2$ is a type-II Dirac semimetal as well as a superconductor. According to theoretical research, there was a high probability of realizing unconventional superconductivity in this material. Being motivated by this claim, I investigated the nature of superconductivity in this material using one of the most powerful techniques, the "STM," which is capable of directly probing the superconducting order parameter. Through our experiments, we reported that, quite unexpectedly, superconductivity in $PdTe_2$ is conventional in nature.

(ii) Sb_2Se_3 is not known to be a topological insulator under ambient conditions. However, the materials such as Bi_2Se_3, Bi_2Te_3, Sb_2Te_3 with similar stoichiometry are known to be strong topological insulators. A high spin-

polarized transport current is expected in a topological insulator due to spin-momentum locking. Using STM, we probed that Sb_2Se_3 is not a topological insulator under ambient conditions. However, unexpectedly, it is found that Sb_2Se_3 have highly spin-polarized conducting surface states probed by spin-resolved directional point-contact spectroscopy and the spin-polarization is coming from Rashba type SOC.

(iii) $Pb_{0.6}Sn_{0.4}Te$ is a topological crystalline insulator and is not a superconductor under ambient conditions. We performed point contact spectroscopy on $Pb_{0.6}Sn_{0.4}Te$ using metallic (Pd, Ag) tips which are also not superconductors. But, unexpectedly, we saw that as soon as the point-contact is made between the tip and sample, the nano-droplet under the mesoscopic point-contact becomes superconducting.

In conclusion, we have investigated some of the exciting properties exhibited by these materials, which might play a crucial role in understanding the subject and provide key information from the application point of view.

Along with these findings, I have also gained experience in designing and fabrication of low-temperature high-vacuum instruments. I designed and fabricated a user-friendly point-contact probe that can operate at millikelvin temperatures.

Bibliography

[1] Joseph D. Martin, Physics Today **72**, 1, 30 (2019);

[2] H. Kamerlingh Onnes, Research notebooks 56, 57, Kamerlingh Onnes Archive, Boerhaave Museum, Leiden, the Netherlands.

[3] K. P. Klitzing, G. Dorda, and M. Pepper, Phys. Rev. L **46**, 6 (1980)

[4] D. Hsieh, D. Qian, L. Wray, Y. Xia, Y. S. Hor, R. J. Cava, and M. Z. Hasan, Nature **452** , 970 (2008).

[5] T. H. Hsieh, H. Lin, J. Liu, W. Duan, A. Bansil, and L. Fu: Nat. Commun. **3**, 982 (2012).

[6] Y. Tanaka, Z. Ren, T. Sato, K. Nakayama, S. Souma, T. Takahashi, K. Segawa, and Y. Ando: Nat. Phys. **8**,800(2012).

[7] Z. K. Liu, B. Zhou, Y. Zhang, Z. J. Wang, H. M. Weng, D. Prabhakaran, S.-K. Mo, Z. X. Shen, Z. Fang, X. Dai, Z. Hussain, and Y. L. Chen, Science **343**, 864-867 (2014).

[8] Su-Yang Xu *et. al.*, Science **349**, 613-617 (2015)

[9] M. Sato and Y. Ando, Reports on Progress in Physics **80**, 7 (2017)

[10] T. Ando and Y. Uemura: J. Phys. Soc. Jpn. **36**, 959 (1974).

[11] D. J. Thouless, M. Kohmoto, M. P. Nightingale, and M. den Nijs, Phys. Rev. Lett. **49**, 405 (1982).

[12] D. C. Tsui, H. L. Stormer, and A. C. Gossard: Phys. Rev. Lett. **48** , 1559 (1982).

[13] X. G. Wen and Q. Niu, Phys. Rev. B **41**,9377 (1990).

[14] Y. K. Kato, R. C. Myers, A. C. Gossard, and D. D. Awschalom, Science **306**, 1910 (2004).

[15] M. I. D'yakonov and V. I. Perel', JETP Lett. **13**, 467 (1971).

[16] J. E. Hirsch, Phys. Rev. Lett. **83**, 1834 (1999).

[17] S. Zhang: Phys. Rev. Lett. **85**, 393 (2000).

[18] S. Murakami, N. Nagaosa, and S. C. Zhang, Science **301**, 1948 (2003).

[19] J. Sinova, D. Culcer, Q. Niu, N. A. Sinitsyn, T. Jungwirth, and A. H. MacDonald, Phys. Rev. Lett. **92**, 126606 (2004).

[20] B. A. Bernevig, T. L. Hughes, and S.-C. Zhang, Science **314**, 1757 (2006).

[21] M. Konig, S. Wiedmann, C. Brune, A. Roth, H. Buhmann, L. W. Molenkamp, X.-L. Qi, and S.-C. Zhang, Science **318**, 766 (2007).

[22] L. Fu, C. L. Kane, Phys. Rev. B **76**, 045302 (2007).

[23] H. Zhang et al., Nat. Phys. **5**, 438 (2009).

[24] Y. Xia et al., Nat. Phys. **5**, 398 (2009).

[25] Y. L. Chen et al., Science **325**, 178 (2009).

[26] C. L. Kane and E. J. Mele: Phys. Rev. Lett. **95**, 226801 (2005).

[27] K.v. Klitzing, Phil. Trans. R. Soc. A, **363**, 2211 (2005).

[28] Neil W. Ashcroft, N. David Mermin, Solid State Physics, 1976

[29] S. Murakami, New Journal of Physics **9**, 356 (2007).

[30] Xiao-Liang Qi and Shou-Cheng Zhang, Physics Today **63**, 33 (2010).

[31] Meinolf Geek, Gunter Malle, in Handbook of Algebra, 2006

[32] M. Z. Hasan, and C. L. Kane, Reviews of Modern Physics **82**, 3045 (2010)

[33] Luis Alvarez-Gaume, and Miguel A. Vazquez-Mozo, arXiv:hep-th/0510040v4.

[34] J. J. Sakurai, Book: Modern Quantum Mechanics-second edition, p-306, 2014

[35] Y. Ando, Journal of the Physical Society of Japan, **82**, 102001 (2013).

[36] Kramers, H. A., Proc. Amsterdam Acad. **33**, 959 (1930).

[37] C. L. Kane and E. J. Mele, Phys. Rev. Lett. **95**, 146802 (2005).

[38] J. E. Moore and L. Balents, Phys. Rev. B **75**, 121306(R) (2007).

[39] L. Fu, C. L. Kane, and E. J. Mele, Phys. Rev. Lett. **98**, 106803 (2007).

[40] R. Roy, Phys. Rev. B **79**, 195322 (2009).

[41] J. E. Moore, nature **464**, 11 (2010)

[42] H. Zhang, C.-X. Liu, X.-L. Qi, X. Dai, Z. Fang, and S.-C. Zhang, Nat. Phys. **5**, 438 (2009).

[43] D. Hsieh, Y. Xia, D. Qian, L. Wray, F. Meier, J. H. Dil, J. Osterwalder, L. Patthey, A. V. Fedorov, H. Lin, A. Bansil, D. Grauer, Y. S. Hor, R. J. Cava, and M. Z. Hasan: Phys. Rev. Lett. **103**, 146401 (2009).

[44] Y. Jiang, Y. Wang, M. Chen, Z. Li, C. Song, K. He, L. Wang, X. Chen, X. Ma, and Q.-K. Xue, Phys. Rev. Lett. **108**, 016401 (2012).

[45] P. Roushan, *et. al.*, Nature **460**, 1106 (2009).

[46] J.E. Hoffman, K. McElroy, D.-H. Lee, K.M. Lang, H. Eisaki, S. Uchida, and J.C. Davis, Science **297**, 1148 (2002).

[47] Tong Zhang, Peng Cheng, Xi Chen, Jin-Feng Jia, Xucun Ma, Ke He, Lili Wang, Haijun Zhang, Xi Dai, Zhong Fang, Xincheng Xie, and Qi-Kun Xue Phys. Rev. Lett. **103**, 266803 (2009)

[48] Kun Zhao, Yan-Feng Lv, Shuai-Hua Ji, Xucun Ma, Xi Chen and Qi-Kun Xue, J. Phys.: Condens. Matter **26**, 394003 (2014).

[49] T. Hanaguri, K. Igarashi, M. Kawamura, H. Takagi, and T. Sasagawa, Phys. Rev. B **82**, 076801 (2010)

[50] Peng Cheng *et. al.* Phys. Rev. Lett. **105**, 076801 (2010)

[51] A. A. Taskin, S. Sasaki, K. Segawa, and Y. Ando, Phys. Rev. Lett. **109** (2012) 066803.

[52] A. Pariari, P. Dutta, and P. Mandal, Physical Review B **91**, 155139 (2015).

[53] Hui Yang, Roderich Moessner, and Lih-King Lim Phys. Rev. B **97**, 165118 (2018)

[54] Bohm-Jung Yang and Naoto NagaosaNature Communications **5**, 4898 (2014).

[55] S. Murakami, S. Iso, Y. Avishai, M. Onoda, and N. Nagaosa, Phys. Rev. B **76**, 205304 (2007).

[56] S. Murakami, and S. -i. Kuga, Phys. Rev. B **78**, 165313 (2008).

[57] S. Murakami, New J. Phys. **9**, 356 (2007).

[58] S. -Y. Xu, et al. Science **332**, 560–564 (2011).

[59] T. Sato, et al. Nat. Phys. **7**, 840 (2011).

[60] S. M. Young, et al. Phys. Rev. Lett. **108**, 140405 (2012).

[61] J. A. Steinberg, et al. Phys. Rev. Lett. **112**, 036403 (2014).

[62] Z. Wang, et al. Phys. Rev. B **85**, 195320 (2012).

[63] Z. Wang, H. Weng, Q. Wu, X. Dai, and Z. Fang, Phys. Rev. B **88**, 125427 (2013).

[64] J. L. Manes, Phys. Rev. B **85**, 155118 (2012).

[65] T. Morimoto, and A. Furusaki, Phys. Rev. B **89**, 235127 (2014).

[66] Dirac, P. A. M. Dirac, Proceedings of the Royal Society A: Mathematical, Physical and Engineering Sciences. 117 (778) (1928).

[67] H. Weyl, I. Z. Phys. **56**, 330 (1929).

[68] B. P. Palash, American Journal of Physics **79**, 485 (2011).

[69] Souma, S., et al., 2016, Phys. Rev. B **93**, 161112 (2012)

[70] M. Salehi *et. al.*, Nano Lett. **16** 5528–5532 (2016)

[71] Fucong Fei*et.al.*, Phys. Rev. B **96**, 041201(R) (2017)

[72] Han-Jin Noh, Jinwon Jeong, En Jin Cho, Kyoo Kim, B. I. Min, and Byeong Gyu Park Phys. Rev. Lett. **119**, (2017)

[73] Kenan Zhang, Mingzhe Yan, Haoxiong Zhang, Huaqing Huang, Masashi Arita, Zhe Sun, Wenhui Duan, Yang Wu, and Shuyun Zhou Phys. Rev. B **96**, 125102 (2017)

[74] Honghong Zhang, Yuee Xie, Chengyong Zhong, Zhongwei Zhang, Yuanping Chen, arXiv:1612.08456 (2016)

[75] Peng Li, Yan Wen, Xin He, Qiang Zhang, Chuan Xia, Zhi Ming Yu, Shengyuan A. Yang, Zhiyong Zhu, Husam N. Alshareef and Xi-Xiang Zhang, Nature Communication **8**, (2017)

[76] J. Jiang, *et. al.*, Nature Communications **8**,13973 (2017).

[77] N. P. Armitage, E. J. Mele, Ashvin Vishwanath, Reviews of Modern Physics **90** (2018).

[78] X. Wan, A. M. Turner, A. Vishwanath, and S. Y. Savrasov, Phys. Rev. B 83, 205101 (2011).

[79] F. D. M. Haldane, arXiv:1401.0529 (2014).

[80] Su-Yang Xu, *et. al.*, Science **349**, 613 (2015)

[81] Rajib Batabyal *et. al.*, Sci. Adv. **2**, e1600709 (2016)

[82] L. Fu, Pgys. Rev. Lett. **106**, 106802 (2011)

[83] Y. Ando, and L. Fu, Annu. Rev. Condens.Matter Phys. **6**, 361 (2015).

[84] A. Gyenis, I. K. Drozdov, S. Nadj-Perge, O. B. Jeong, J. Seo, I. Pletikosic, T. Valla, G. D. Gu, A. Yazdani Phys. Rev. B **88**, 125414 (2013)

[85] I. Zeljkovic *et. al.* 2013 Nature Physics **10**, 572-577 (2014)

[86] Y. Okada, *et. al.* Science **27**, 1499 (2013).

[87] Ning Xu, Yong Xu, and Jia Zhu, npj Quantum Materials **2**, 51 (2017)

[88] I. A. Nechaev, *et. al.*, Phys. Rev. B **87**, 121111(R) (2013)

[89] Devendra Kumar, Archana Lakhani, Rapid Research Letters 9, 636 (2015)

[90] H. H. Kung *et. al.*, PNAS **116**, (2019)

[91] H. B. Zhang, H. L. Yu and G. W. Yang, EPL **95**, 5 (2011)

[92] Yu. A. Bychkov and E. I. Rashba, Sov. Phys. JETP Lett. **39**, 78-81 (1984)

[93] A. Manchon, H.C. Koo, J. Nitta, S.M. Frolov, R.A. Duine, Nature Materials **14**, 871-882 (2015)

[94] Fanming Qu, *et. al.*, Phys. Rev. Lett. **107**, 016802 (2011)

[95] K. Borisov, C.-Z. Chang, J. S. Moodera, and P. Stamenov, Phys. Rev. B **94**, 094415 (2016).

[96] C. Beenakker, Annual Review of Condensed Matter Physics **4**, 113 (2013).

[97] V. Mourik, K. Zuo, S. M. Frolov, S. Plissard, E. P. Bakkers, and L. P. Kouwenhoven, Science **336**, 1003 (2012).

[98] R. M. Lutchyn, J. D. Sau, and S. Das Sarma, Physical review letters **105**, 077001 (2010).

[99] Y. Oreg, G. Refael, and F. von Oppen, Physical review letters **105**, 177002 (2010).

[100] L. Fu and C. L. Kane, Phys. Rev. Lett. **100**, 096407 (2008).

[101] A. Das, Y. Ronen, Y. Most, Y. Oreg, M. Heiblum, and H. Shtrikman, Nature Physics **8**, 887 (2012).

[102] M. Deng, C. Yu, G. Huang, M. Larsson, P. Caroff, and H. Xu, Nano letters **12**, 6414 (2012).

[103] A. D. K. Finck, D. J. Van Harlingen, P. K. Mohseni, K. Jung, and X. Li, Phys. Rev. Lett. **110**, 126406 (2013).

[104] H. O. H. Churchill, V. Fatemi, K. Grove-Rasmussen, M. Deng, P. Caroff, H. Xu, and C. M. Marcus, Physical Review B 87, 241401 (2013).

[105] Jun Chen, Benjamin Woods, Peng Yu, Moira Hocevar, Diana Car, Sebastien Plissard, Erik Bakkers, Tudor Stanescu, Sergey Frolov, arXiv:1902.02773v2 (2019)

[106] E. J. H. Lee, X. Jiang, R. Aguado, G. Katsaros, C. M. Lieber, and S. De Franceschi, Phys. Rev. Lett. **109**, 186802 (2012).

[107] D. I. Pikulin, J. P. Dahlhaus, M. Wimmer, H. Schomerus, and C. W. J. Beenakker, New Journal of Physics **14**, 125011 (2012)

[108] Y. Ando, T. Hamasaki, T. Kurokawa, K. Ichiba, F. Yang, M. Novak, S. Sasaki, K. Segawa, Y. Ando, and M. Shiraishi, Nano Lett. **14**, 6226 (2014).

[109] J. Tang, L. T. Chang, X. Kou, K. Murata, E. S. Choi, M. Lang, Y. Fan, Y. Jiang, M. Montazeri, W. Jiang, Y. Wang, L. He, and K. L. Wang, Nano Lett. **14**, 5423 (2014).

[110] C. Li, O. Vant Erve, J. Robinson, Y. Liu, L. Li, and B. Jonker, Nat. Nanotechnol. 9, 218 (2014).

[111] A. Dankert, J. Geurs, M. V. Kamalakar, S. Charpentier, and S. P. Dash, Nano Lett. **15**, 7976 (2015).

[112] A. F. Andreev, J. Exp. Theor. Phys. **46**, 1823 (1964) [Sov. Phys. JETP. **19**, 1228 (1964)].

[113] Yu. G. Naidyuk, I. K. Yanson, *Point-contact Spectroscopy*, Springer-Verlag New York (2005).

[114] D. Daghero, R. S. Gonnelli, Supercond. Sci. Tech. **23** 043001 (2010).

[115] L. Janson, M. Klein, H. Lewis, A. Lucas, A. Marantan, K. Luna, Am. J. Phys. **80**, 133 (2012).

[116] Nickolas Groll, M. J. Pellin, J. F. Zasadzinksi, T. Proslier, Rev. Sc. Instrum. **86** 095111 (2015).

[117] Supriyo Datta, *Electronic Transport in Mesoscopic Systems*, Cambridge University Press, Cambridge (1999).

[118] A. Wexler, Proc. Phys. Soc. **89**, 927 (1966).

[119] G. Sheet, S. Mukhopadhyay, P. Raychaudhuri, Phys. Rev. B **69**, 134507 (2004).

[120] B. J. van Wees, H. van Houten, C. W. J. Beenakker, J. G. Williamson, L. P. Kouwenhoven, D. van der Marel, and C. T. Foxon Phys. Rev. Lett. **60**, 848 (1988).

[121] G. E. Blonder, M. Tinkham, and T. M. Klapwijk, Phys. Rev. B **25**, 7 (1982).

[122] A. Plecenik, M. Grajcar, and S. Benacka, Phys. Rev. B **49**, 14 (1994).

[123] M. Tinkham, *Introduction to Superconductivity*, Dover, Second Edition (2004).

[124] R. C. Dynes, V. Narayanamurti, and J. P. Garno, Phys. Rev. Lett. **41**, 1509 (1978).

[125] S. K. Upadhyay *et. al.*, Phys. Rev. Lett. **81**, 3247 (1998)

[126] R. J. Soulen *et. al.*, Science 282, 85 (1998).

[127] P. Raychaudhuri, A. P. Mackenzie, J. W. Reiner, and M. R. Beasley, Phys. Rev. B **67**, 020411(R) (2003)

[128] Goutam Sheet, *et. al.*, Phys. Rev. B **72**, 180407(R) (2005).

[129] I. I. Mazin, A. A. Golubov, and B. Nadgorny, J. Appl. Phys. **89**, 7576 (2001).

[130] S. Kamboj et. al., J. of Phys.: Condensed Matter **30**, 35 (2018)

[131] G. Binnig, H. Rohrer, Ch. Gerbe, E. Weibe, Physical Review Letters **49** 57 (1982).

[132] Matthias Hunstig, Actuators **6** (2017)

[133] A G M Jansen, A P van Gelder and P Wyder, Journal of Physics C: Solid State Physics **13**, 33

[134] Mikael Fogelström, W. K. Park, L. H. Greene, G. Goll, and Matthias J. Graf Phys. Rev. B **82**, 014527

[135] M Aslam, *et al.*, Solid State Communications **264**, 26-30 (2017).

[136] M Aslam *et al.* , Journal of Physics: Condensed Matter **28**, 19 (2017)

[137] X Lu, *et al.*, Superconductor Science and Technology**23**, 5

[138] P. Samuel *et al.*, Nanoscience and Engineering in Superconductivity **28**, 187-210 (2010)

[139] L. Fu, **et al.**, Phys. Rev. B **79**, 161408(R) (2009).

[140] R. M. Lutchyn, *et al.*, Phys. Rev. Lett. **105**, 077001 (2010).

[141] Y. Oreg, **et al.**, Phys. Rev. Lett. **105**, 177002 (2010).

[142] M. Ruby, *et al.*, Phys. Rev. Lett. **115**, 197204 (2015).

[143] Nadj Perge *et al.*, Phys. Rev. B **88**, 020407(R) (2013).

[144] M. M. Vazifeh, *et al.*, Phys. Rev. Lett. **111**, 206802 (2013).

[145] Y. Kim, *et al.*, Phys. Rev. B **90**, 060401(R) (2014).

[146] Y. Peng, *et al.*, Phys. Rev. Lett. **114**, 106801 (2015).

[147] K. T. Law, *et al.*, Phys. Rev. Lett. **103**, 237001 (2009).

[148] K. Flensberg, Phys. Rev. B **82**, 180516(R) (2010).

[149] V. Mourik, *et al.*, Science **336**, 1003–1007 (2012).

[150] M. T. Deng, *et al.*, Nano Lett. **12**, 6414–6419 (2012).

[151] A. D. K. Finck, *et al.*, Phys. Rev. Lett. **110**, 126406 (2013).

[152] Nadj Perge et al. Science **346**, 602–607 (2014).

[153] Hua-Jun Chen, *et al.*, Scientific Reports **6**, 36600 (2016)

[154] Hao-Hua Sun and Jin-Feng Jia npj Quantum Materials **2**, 34 (2017)

[155] Yupeng Li, *et al.* npj Quantum Materials **3**, 58 (2018)

[156] X. C. Pan, *et al.*, Nat. Commun. **6**, 7805 (2015).

[157] L. P. He, *et al.*, NPJ Quantum Mater. 1, 16014 (2016).

[158] Y. H. Zhou, *et al.*, Proc. Natl Acad. Sci. USA **113**, 2904–2909 (2016).

[159] K. Kirshenbaum, *et al.* Phys. Rev. Lett. **111**, 087001 (2013).

[160] J. L. Zhang, *et al.* Proc. Natl Acad. Sci. USA **108**, 24–28 (2011).

[161] J. Zhu, *et al.* Sci. Rep. **3**, 2016 (2013).

[162] Z. Li, *et al.*, Phys. Rev. Materials **2**, 014201 (2018).

[163] K. Momma, *et al.*, J. Appl. Crystallogr **44**, 1272 (2011)

[164] Y. S. Hor, *et al.*, Phys. Rev. Lett. **104**, 057001 (2010).

[165] M. Kriener, *et al.* Phys. Rev. Lett. **106**, 127004 (2011).

[166] S. Das, L. Aggarwal, S. Roychowdhury, M. Aslam, S. Gayen, K. Biswas, and G. Sheet, Appl. Phys. Lett. **109**, 132601 (2016).

[167] L. Aggarwal, A. Gaurav, G. S. Thakur, Z. Haque, A. K. Ganguli, and G. Sheet, Nat. Mater. 15, 32 (2016).

[168] H. Wang, H. Wang, H. Liu, H. Lu, W. Yang, S. Jia, X.-J. Liu, X. C. Xie, J. Wei, and J. Wang, Nat. Mater. **15**, 38 (2016).

[169] L. Aggarwal, S. Gayen, S. Das, R. Kumar, V. Süß, C. Felser, C. Shekhar, and G. Sheet, Nat. Commun. **8**, 13974 (2017).

[170] J. Guggenheim, F. Hulliger, and J. Muller, Helv. Phys. Acta **34**, 408 (1961).

[171] S. Das, *et al.*, Physical Review B **97**, 014523 (2018).

[172] P. P. Kong, *et. al.*, Scientific Reports **4**, 6679 (2014)

[173] A. Sirohi *et al.*, Journal of Physics: Condensed Matter, **31**, 8 (2019)

[174] A. Bera, *et. al.*, Phys. Rev. Lett. **110**, 107401 (2013).

[175] I. Efthimiopoulos, *et. al.*, Sci. Rep. **3**, 2665 (2013).

[176] W. Li, X.-Y. Wei *et. al.*, Phys. Rev. B **89**, 035101 (2014).

[177] I. Efthimiopoulos *et. al.*, Sci. Rep. **6**, 24246 (2016).

[178] D Hsieh1, *et al.* New Journal of Physics **12**, (2010)

[179] S. -Y. Xu, Y. Xia, L. A. Wray, S. Jia, F. Meier, J. H. Dil, J. Osterwalder, B. Slomski, A. Bansil, H. Lin, R. J. Cava, and M. Z. Hasan, Science **332**, 560–564 (2011).

[180] Y. Xia, D. Qian, D. Hsieh, L Wray, A. Pal, H. Lin, A. Bansil, D. Grauer, Y. S. Hor, R. J. Cava, and M. Z. Hasan, Nat. Phys. **5**, 398–402 (2009).

[181] J. W. McIver, D. Hsieh, H. Steinberg, P. Jarillo-Herrero, N. Gedik, Nat. Nanotechnol. **7**, 96–100 (2012).

[182] C. Jozwiak, C. -H. Park, K. Gotlieb, C. Hwang, D. -H. Lee, S. G. Louie, J. D. Denlinger, C. R. Rotundu, R.J. Birgeneau, Z. Hussain, and A. Lanzara, Nat. Phys. **9**, 293–298 (2013).

[183] C. -H. Park, S. G. Louie, Phys. Rev. Lett. **109**, 097601 (2012).

[184] C. H. Li, O. M. J. van't Erve, J. T. Robinson, Y. Liu, L. Li, B. T. Jonker, Nat. Nanotechnol. **9**, 218–224 (2014).

[185] S. Hong, V. Diep, S. Datta, Y. P. Chen, Phys. Rev. B **86**, 085131 (2012)

[186] S. Das, *et. al.*, Physical Review B **97**, 235306 (2018).

[187] Sunghun Kim, *et. al.*, Phys. Rev. Lett. **112**, 136802 (2014)

[188] W. Zhou, T. Seki, T. Kubota, G. E. W. Bauer, and K. Takanashi Phys. Rev. Materials **2**, 094404 (2018)

[189] H. Wang, H. Liu, C. -Z. Chang, H. Zuo, Y. Zhao, Y. Sun, Z. Xia, K. He, X. Ma, X. C. Xie, Q. -K. Xue, and J. Wang, Scientific Reports **4**, 5817 (2014).

[190] T. McGuire and R. Potter, IEEE Trans. Magn. 11, 1018 (1975).

[191] O. Breunig *et al.*, Nature Communications **8**, 15545 (2017)

[192] G. Long, S. Xu, X. Cai, Z.Wu, T. Han, J. Lin, C. Cheng, Y. Cai, X. Wang, and N. Wang, Nanotechnology 29, 035204 (2018).

[193] F. V. Tikhonenko, A. A. Kozikov, A. K. Savchenko, and R. V. Gorbachev, Phys. Rev. Lett. 103, 226801 (2009).

[194] G. Kresse and J. Furthm uller, Phys. Rev. B **54**, 11169(1996).

[195] G. Kresse, D. Joubert, Phys. Rev. B **59**, 1758 (1999).

[196] A. Bansil, H. Lin and T. Das, Rev. Mod. Phys. **88**, 021004 (2016).

[197] Su Yang Xu, *et al.*, Nature Communications volume **3**, 1192 (2012)

[198] K. K. Likharev, Rev. Mod. Phys. **51**, 101 (1979)

[199] Introduction to superconductivity, A. C. Rose-Innes and E. H. Rhoderick, Pergamon, Second Edition (1978).